10. Attachements

10.1 Attachement no. 1

First author

1. **LAHUTSINA, Anastasiya**; ŠPANIEL, Filip; MRZÍLKOVÁ, Jana; MOROZOVA, Alexandra; BRABEC, Marek; MUSIL, Vladimír; ZACH, Petr. Morphology of Anterior Cingulate Cortex and Its Relation to Schizophrenia. *Journal of Clinical Medicine*. 2023, **12**(1), 33. ISSN 2077-0383. DOI: 10.3390/jcm12010033.

IF: 4.964/2021 (Q2/2021)

Journal of
Clinical Medicine

MDPI

Article

Morphology of Anterior Cingulate Cortex and Its Relation to Schizophrenia

Anastasiya Lahutsina [1,*], Filip Spaniel [2], Jana Mrzilkova [1], Alexandra Morozova [1], Marek Brabec [3], Vladimir Musil [4] and Petr Zach [1,2,*]

1 Department of Anatomy, Third Faculty of Medicine, Charles University, 100 00 Prague, Czech Republic
2 National Institute of Mental Health, 250 67 Klecany, Czech Republic
3 Department of Statistical Modeling, Institute of Computer Science, Academy of Sciences of the Czech Republic, 182 00 Prague, Czech Republic
4 Centre of Scientific Information, Third Faculty of Medicine, Charles University, 100 00 Prague, Czech Republic
* Correspondence: anastasiya.lahutsina@lf3.cuni.cz (A.L.); petr.zach@lf3.cuni.cz (P.Z.)

Abstract: Cortical folding of the anterior cingulate cortex (ACC), particularly the cingulate (CS) and the paracingulate (PCS) sulci, represents a neurodevelopmental marker. Deviations in in utero development in schizophrenia can be traced using CS and PCS morphometry. In the present study, we measured the length of CS, PCS, and their segments on T1 MRI scans in 93 patients with first-episode schizophrenia and 42 healthy controls. Besides the length, the frequency and the left-right asymmetry of CS/PCS were compared in patients and controls. Distribution of the CS and PCS morphotypes in patients was different from controls. Parcellated sulcal pattern CS3a in the left hemisphere was longer in patients (53.8 25.7 mm vs. 32.7 19.4 mm in controls, $p < 0.05$), while in CS3c it was reversed—longer in controls (52.5 22.5 mm as opposed to 36.2 12.9 mm, n.s. in patients). Non parcellated PCS in the right hemisphere were longer in patients compared to controls (19.4 10.2 mm vs. 12.1 12.4 mm, $p < 0.001$). Therefore, concurrent presence of PCS1 and CS1 in the left hemisphere and to some extent in the right hemisphere may be suggestive of a higher probability of schizophrenia.

Keywords: MRI; schizophrenia; morphology; anatomy; cingulate and paracingulate sulci

Citation: Lahutsina, A.; Spaniel, F.; Mrzilkova, J.; Morozova, A.; Brabec, M.; Musil, V.; Zach, P. Morphology of Anterior Cingulate Cortex and Its Relation to Schizophrenia. J. Clin. Med. **2023**, 12, 33. https://doi.org/10.3390/jcm12010033

Academic Editor: Nuri B. Farber

Received: 17 October 2022
Revised: 16 December 2022
Accepted: 17 December 2022
Published: 21 December 2022

1. Introduction

Schizophrenia is a heterogeneous group of psychotic diseases with the current absence of clear demarcating neurobiological boundaries of its subtypes [1,2]. Subsequent findings of epidemiological, brain-specific molecular processes and genetic findings may play an important role in the pathogenesis of schizophrenia [3,4]. To this end, aberrations in qualitative anatomical landmarks, i.e., in a form of sulcal morphology, might be of particular value since they may bring additional information on developmental perturbations in regions susceptible to the illness pathology since the gyrification/fissurization of the cortex development is being accomplished principally during the second and third trimester of gestation [5,6]. Abnormalities in the anterior cingulated cortex (ACC) region proven by structural magnetic resonance imaging (MRI) accompanied by neuropathological findings and working memory processing deficit [7] may testify to a neurobiological basis for schizophrenia [8]. Brugger and Howes [9] in their meta-analysis from 2017 based on MRI morphometry from 3901 patients with first-episode schizophrenia and 4040 controls discovered greater homogeneity of the ACC volume and significantly lower mean volume, which may signalize schizophrenia. Modified controllability of functional activity in dorsal ACC may also play an important role in the pathophysiology of schizophrenia, consistent with the importance of this region in cognitive and brain state control operations [10]. At the same time, available findings point to the fact that the ACC gray matter reductions

m

precede psychosis onset and that neurodevelopment of the ACC region might thus be in play [8].

All of the above underlines the importance of quantification of the ACC folding pattern in schizophrenia. Assessment of sulcal patterning in the ACC may serve as a macroscopic probe for hidden developmental events within this area.

Such insights might be expected to arise, especially from the study of the two major sulcal landmarks in the ACC region: the cingulate sulcus (CS) and the paracingulate sulcus (PCS). The CS runs along the corpus callosum and extends posteriorly into the parietal lobe as the marginal ramus. From the dorsal to the anterior portion of the CS, a sulcus that is often present and runs parallel to the CS is referred to as the paracingulate sulcus [11]. The PCS shows significant individual and hemispheric differences. While the CS is present in the majority of cases, the PCS is frequently missing or rudimentary [12]; although it was recently reported to be present in 70.1% of the human population [13]. Leftward asymmetry of PCS has been reported in healthy controls [12,14,15].

Inter-individual variation in the PCS presence is transposed into the prenatal formation of single or double parallel type of the ACC, which is reported in 76% and 24% of adults, respectively [16].

From the developmental perspective, the first appearance of the CS was reported in the 19th week of the fetal period, and the marginal branch of the CS at the 30th 3 weeks [17]. An ultrasound study in 677 term-born neonates clearly identified four distinct major folding patterns in the CS [18], which is consistent with reports of the adult brain folding patterns on the MRI and autopsy materials [16,19]. Subsequently, an individual ACC sulcal pattern remains fixed from childhood to adulthood, at the same time that quantitative structural ACC metrics are undergoing profound developmental change [20].

Empirical evidence for the neurodevelopmental and/or neurodegeneration origin of schizophrenia is still a matter of debate [21,22]. Both the CS and the PCS are positioned on the medial sides of brain hemispheres; however, the presence of the CS is constant, unlike the PCS. The CS is located above the callosal body with its rostral end either fusing or tapering off with superior rostral sulcus. Dorsally the CS continues along the callosal body and either abruptly terminates at the level of the central sulcus or continues upward as the marginal ramus towards the hemispheric perimeter. The course of the CS may be uninterrupted or split into one, two, or three distinct segments. The PCS is not present constantly and it is located cranially at the level of the anterior CS; its detailed morphology is irregular [23] (Figure 1).

The upper left picture shows an example of the CS1 type (without interruption), the upper middle shows the CS2 type (with one interruption), and the upper right shows the CS3 type (with two interruptions). The lower left picture shows an example of the PCS0 type (absent), the lower middle shows the PCS1 type (present), and the lower right shows the PCS2 type (prominent). The terms ‘absent’, ‘present’, and ‘prominent’ are according to Yücel’s nomenclature.

Several studies suggest that patients with schizophrenia have a less developed PCS in the left hemisphere compared to controls and may be less likely to have a PCS in either hemisphere [24–27]. A leftward bias in the PCS asymmetry has been suggested in healthy volunteer studies, and this asymmetry appears to be absent in patients, usually with a reduction in the left PCS prominence [26,28,29]. A well-formed PCS was also less common in high-risk participants compared to controls; however, this association was only present in males [30].

Bilateral absence of the PCS was associated with reductions in reality monitoring performance in healthy individuals with no neurological damage [31]. In one study, hallucinations were associated with specific brain morphology differences in the PCS; a 1 cm reduction in sulcal length in a medial prefrontal cortical fold increased the likelihood of hallucinations by 20%, regardless of the sensory modality in which hallucinations were experienced [32].

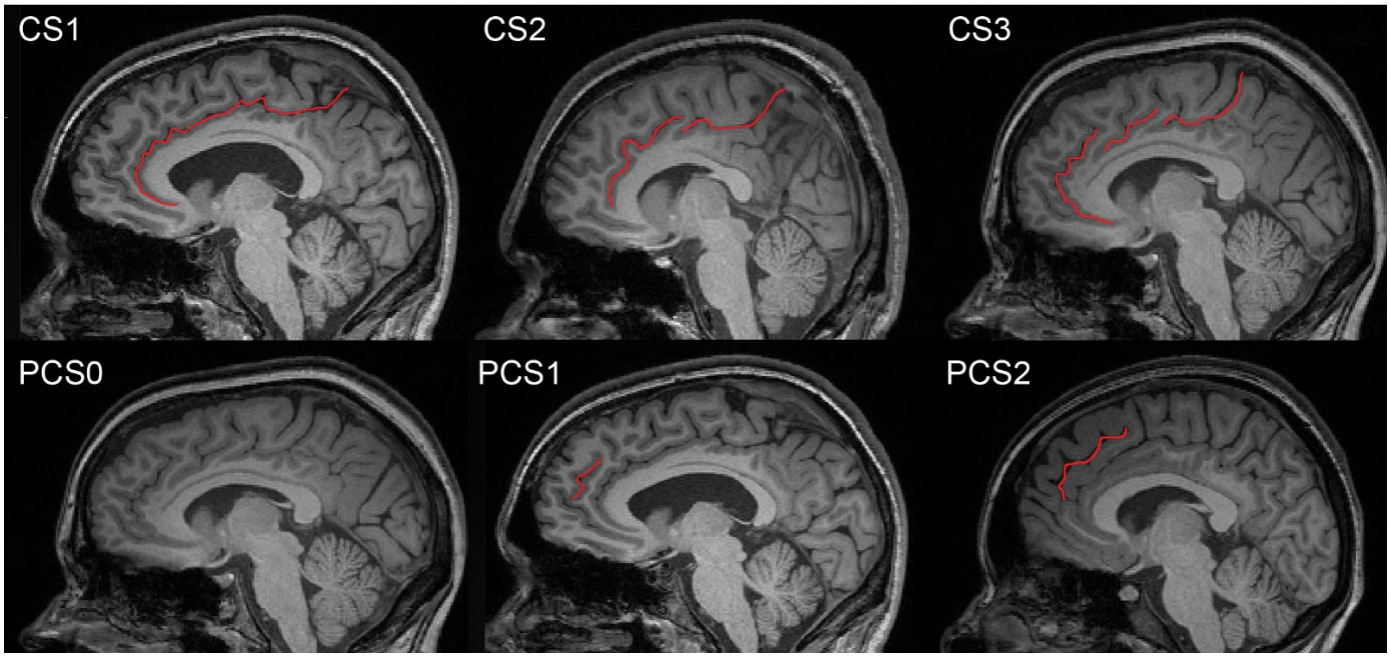

Figure 1. Illustrative examples of possible appearances of CS and PCS morphology types on the MRI images.

Studying the ACC sulcal morphology offers a powerful opportunity to use adult folding patterns to retrospectively assess the differences in earlier brain development between schizophrenia and the norm. Here, we investigate the CS/PCS morphology in both hemispheres in two age/sex matched groups: first-episode schizophrenia and healthy controls. The ACC folding patterns were measured using structural MRI scans.

In our study, we focused on various morphological subtypes of cingulate sulcus parcellations in vivo on the MRI that were not previously investigated in the context of schizophrenia, especially the CS1, CS2a,b, and CS3a,b,c subtypes.

2. Materials and Methods

2.1. Patient Characteristics and Demographics

We selected 93 patients with first-episode schizophrenia (FES, patients) and 42 age/sex matched healthy participants (controls). Demographic data (Table 1) and schizophrenia patient characteristics and diagnoses (Table 2) are presented below.

The patient sample originated from an Early-Stage Schizophrenia Outcome study (ESO), a prospective trial on FES subjects, conducted at the National Institute of Mental Health, Klecany, Czech Republic (NIMH). FES patients were recruited between 2015 and 2019 through the ESO Patient Enrolment Network, which involves five large psychiatric hospitals in the country (in total 3700 beds), with a total catchment area of 6.5 million people. The inclusion criteria for FES were: (1) the diagnosis of schizophrenia or the diagnosis of an acute polymorphic psychotic disorder, as made by a psychiatrist according to the International Classification of Diseases-10 criteria; (2) the first episode of psychotic illness; and (3) duration of untreated psychosis of less than 24 months. Any patients with psychotic mood disorders (including schizoaffective disorder, bipolar disorder, and unipolar depression with psychotic symptoms) were excluded from the study. All patients were treated with antipsychotic drugs at the time of the MRI scanning. The ESO was approved by the Ethical Committee of the NIMH. The study was carried out in accordance with the latest version of the Declaration of Helsinki.

Table 1. Demographic Data of Schizophrenia Patients and Healthy Controls. The Data are Presented as Mean Values SD.

Demographic Data	**Patients Sample Total (n = 93)**	**Healthy Controls (n = 42)**
Sex, n = male/female	47/46	17/25
Age at baseline MRI (V1), year	30.1 7.4	31.6 6.2
Age at second, follow up MRI (V2), year	31.3 7.4	32.6 5.6
Years of education at V2	14.8 3.1 *	17.9 3.6 *
Interscan interval (V1–V2), month	13.0 1.8	16.0 3.8

Values between groups were not significant, except for years of education (* $p < 0.0001$).

Table 2. Characteristics of the Patients and Diagnoses. The Data are Presented as Mean Values SD.

Detailed Overview of Patient's Examination	
Age at onset, year	29.4 7.3 7.7
Duration of illness (DUI) at baseline V1, month	11.2 4 11.9
Duration of untreated psychosis (DUP), month	65.6 15.4
Global Assessment of Functioning (GAF) at V1	79.9 13.0
Global Assessment of Functioning (GAF) at V2	15.7 5.8
Positive and Negative Syndrome Scale (PANSS) negative 1	13.3 5.4 60
Positive and Negative Syndrome Scale (PANSS) negative 2	16.0 48.2
Positive and Negative Syndrome Scale (PANSS) 1S	14.6
Positive and Negative Syndrome Scale (PANSS) 2S	
Final Diagnosis (M/F)	29/30
Schizophrenia	3/2
Acute polymorphic psychotic disorder without symptoms of schizophrenia	9/11
Acute polymorphic psychotic disorder with symptoms of schizophrenia	2/0
Acute schizophrenia-like psychotic disorder	1/0
Other acute predominantly delusional psychotic disorders	1/5
Schizoaffective disorder	

2.2. MR Imaging

All subjects underwent an MR examination on a 3T MRI TRIO scanner (Siemens Medical Systems, Erlangen, Germany) equipped with a 12-channel volume head coil. The protocol of MR imaging included T1-weighted sagittal images obtained using a three-dimensional (3D) magnetization-prepared rapid gradient-echo (MPRAGE) sequence (echo time (TE)/repetition time (TR)/number of acquisitions (NA) = 4.63 ms/2300 ms/1, iPAT = 2, resolution 1 mm 1 mm 1 mm); T2-weighted transversal images obtained using 2D Periodically Rotated Overlapping Parallel Lines with Enhanced Reconstruction (BLADE) sequence (TE/TR/NA = 128 ms/5850 ms/1, 2 concatenations, iPAT = 1, resolution 0.6 mm 0.6 mm 3 mm); and T2-weighted sagittal images obtained using 3D Fluid At-tenuated Inversion Recovery (FLAIR) sequence (TE/TR/NA = 318 ms/6200 ms/1, iPAT = 2, resolution 1 mm 1 mm 1 mm). MR images were visually assessed by neuroradiologists to preclude the presence of pathological changes.

2.3. Processing of the MRI Images

We accessed the NIMH MRI Hydra database by remote access to the mainframe computer with a standard PC. Within the Hydra database, we worked in Windows X-terminal with Image J software suite (https://imagej.net, accessed on 16 October 2022).

MRI images were examined in the sagittal plane and the regions of interest were manually delineated in both hemispheres in the Image J program.

CS and PCS were examined in more than one sagittal section of both brain hemispheres. Due to possible axial movement in the MRI scan and because of variations in the sulcal depth, it was necessary to verify several adjacent sagittal sections to ensure visibility of the entire course of sulci. Figure 1 shows pictures representing sulcal variants purposely depicted in different sagittal sections. Relevant brain structures are presented in more detail in Figure 2.

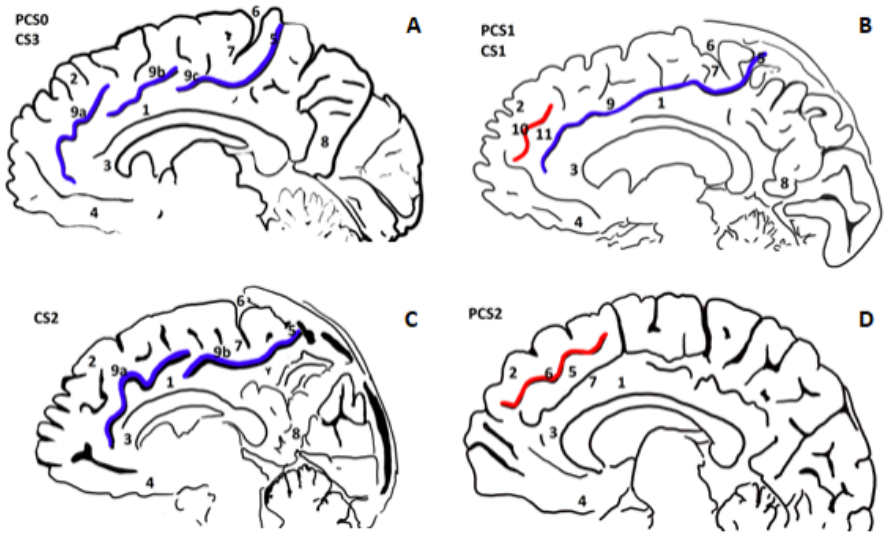

Figure 2. CS and PCS delineations on the medial hemisphere (right) of the brain. Combinations PCS0 and CS3, PCS1 and CS1, PCS2 alone, and CS2 alone do not reflect their co-occurrence in the patients; they were clustered together for better illustration. PCS0 means there is no paracingulate sulcus or its length is shorter than 2 cm. (**A**) PCS0 and CS3: 1—cingulate sulcus, 2—superior frontal gyrus, 3—genu corporis callosi, 4—gyrus rectus, 5—the marginal branch of cingulate sulcus, 6—central sulcus, 7—paracentral lobule, 8—precuneus gyrus, 9a—cingulate sulcus (part one, CS3a), 9b—cingulate sulcus (part two, CS3b) and 9c—cingulate sulcus (part three, CS3c); (**B**) PCS1 and CS1: 1—cingulate sulcus, 2—superior frontal gyrus, 3—genu corporis callosi, 4—gyrus rectus, 5—the marginal branch of cingulate sulcus, 6—central sulcus, 7—paracentral lobule, 8—precuneus gyrus, 9—cingulate sulcus (without interruption, CS1), 10—paracingulate sulcus, 11—paracingulate gyrus (without interruption, PCS1); (**C**) CS2: 1—cingulate sulcus, 2—superior frontal gyrus, 3—genu corporis callosi, 4—gyrus rectus, 5—the marginal branch of cingulate sulcus, 6—central sulcus, 7—paracentral lobule, 8—precuneus gyrus, 9a—cingulate sulcus (part one, CS2a), 9b—cingulate sulcus (part two, CS2b); (**D**) PCS2: 1—cingulate sulcus, 2—superior frontal gyrus, 3—genu corporis callosi, 4—gyrus rectus, 5—paracingulate gyrus, 6—paracingulate sulcus, 7—cingulate sulcus.

2.4. CS and PCS Neuroanatomy

Generally, the CS is always present in the brain while the PCS may not be present at all. The CS is located on the medial part of both the left and right hemispheres. In its major course, it separates the cingulate gyrus from the gyri located above. It often starts in the frontal lobe at the level of the anterior cingulate gyrus and continues dorsally upward between the paracentral lobule and the praecuneus. The PCS, if present, is located above the CS, usually at the level of the ventral portion of the anterior cingulate gyrus [12,32].

2.4.1. CS and PCS Manual Delineation and Morphology Considerations

Manual delineation of any brain structure requires advanced morphological and topographical expertise for precise delineation of the structures of interest.

The CS starts in the subcallosal area and has an arched course, running above the cingulate gyrus. This way it separates the medial frontal and the parietal cortices from the

limbic structure—the cingulate gyrus. Gross delineation of the cingulate sulcus on the MRI is associated with the cingulate gyrus, especially its anterior and posterior portions. The posterior cingulate gyrus is bordered by the marginal ramus of the cingulate sulcus (above), the callosal body (caudally), the parieto-occipital sulcus (dorsally), and the Brodmann area 24 (ventrally). This corresponds to the transition between the anterior and posterior cingulate gyri.

Near the connection between the isthmus of the cingulate gyrus and splenium of the corpus callosum, the marginal branch of the cingulate sulcus reaches the superior end of the hemisphere [33]. According to Terminologia Neuroanatomica [34], we did delineation of the ventral and dorsal borders of the CS in the Cartesian coordinate plane with the center at the level of Monro's interventricular foramen. We characterized borders in accordance with the following anatomical regions: the ventral anterior cingulate cortex (vACC), the dorsal anterior cingulate cortex (dACC), and the posterior cingulate cortex (PCC). The CS arises as a profound groove in the vACC, from under the genu of callosal body and the rostral gyrus and then it runs parallel to the upper frontal gyrus (Figure 1). The trajectory of the CS is interrupted in the dACC by the dorsal cingulate-frontal infolding. In the PCC, after a horizontal trajectory parallel to the body of the callosal body, CS is interrupted again by the anterior cingulate-parietal connective infolding [35].

2.4.2. Description of CS and PCS Parcellation and Its Nomenclature

First, we measured non-parcellated CS and PCS (without separation of the sulci course into interrupted segments). Next, we performed the segmentation of the CS and PCS.

We measured the linear length of the CS and observed how many parts it was composed of in the case of interruption—in other words, CS morphology was assessed depending on the integrity of the sulcal line. If there was no interruption of the sulcus, we labeled it as CS1, one interruption of the sulcus was labeled as CS2, and two interruptions were labeled as CS3. For the length measurement, two sulcal parts (segments) of CS2 were labeled as CS2a and CS2b, and three sulcal parts of CS3 were labeled as CS3a, CS3b, and CS3c, and their length was measured separately (Table 3). Indexing parts (segments) followed the ventro-dorsal position so that, for example, CS2a was located more ventrally compared to CS2b. The neuroanatomical delineation of the PCS was adapted according to J. R. Garrison's Paracingulate Sulcus Measurement Protocol [36], based on the original study [32]. We selected the PCS sulcal pattern parcellation identical with Yücel's nomenclature (three sulcal patterns type—absent, present, and prominent) [14]. PCS morphology was assessed as absent if the length was less than 2 cm (PCS0), present if it extended more than 2 cm (PCS1), and prominent if it was longer than 4 cm (PCS2) (Figure 1).

Table 3. Detailed analysis of the length of the parcellated CS and PCS on the left and right side in schizophrenia patients and controls and their incidences. The data are presented for all types of morphology (CS types 1, 2, 3 and PCS types 0, 1, 2). The length data are presented as mean values in mm SD. The incidence is presented as a number of cases (n) and their percentages. Incidences of CS types 2 and 3 are given as a single value for all relevant sulcal parts (segments). Statistical significance was calculated by nonparametric Mann–Whitney U test and Kruskal–Wallis test ($p < 0.05$ and $p < 0.001$).

Brain Structures	Patients		Controls	
	Length in mm	Incidence n (%)	Length in mm	Incidence n (%)
Left cingulate sulcus type 1 (CS1)	110.7 15.8	61 (66)	105.2 21.7	6 (14)
Left cingulate sulcus type 2a (CS2a)	59.8 16.3	26 (28)	52 19.3	17 (41)
Left cingulate sulcus type 2b (CS2b)	55.9 18.3		62.9 26	

Table 3. Cont.

Brain Structures	Patients		Controls	
Left cingulate sulcus type 3a (CS3a)	53.8 25.7 p < 0.05	6 (6)	32.7 19.4 p < 0.05	19 (45)
Left cingulate sulcus type 3b (CS3b)	20.5 9		22.3 12.9	
Left cingulate sulcus type 3c (CS3c)	36.2 12.9		52.5 22.5	
Right cingulate sulcus type 1 (CS1)	113.3 18.7	58 (63)	123.2 19.1	5 (12)
Right cingulate sulcus type 2a (CS2a)	65.9 23.8	30 (32)	57.2 26.7	18 (43)
Right cingulate sulcus type 2b (CS2b)	53.6 2.3		63.8 27.5	
Right cingulate sulcus type 3a (CS3a)	47.7 7.7	5 (5)	35.9 16.1	19 (45)
Right cingulate sulcus type 3b (CS3b)	39.2 17.2		24.9 19.7	
Right cingulate sulcus type 3c (CS3c)	34.5 16.3		49.3 20.1	
Left paracingulate sulcus type 0 (PCS0)	10.8 4.8	63 (68)	10.9 4.3	34 (81)
Left paracingulate sulcus type 1 (PCS1)	27.1 4.7	30 (32)	29.3 6.5	8 (19)
Left paracingulate sulcus type 2 (PCS2)	N / A	0 (0)	N / A	0 (0)
Right paracingulate sulcus type 0 (PCS0)	11.7 5.2 p < 0.001	51 (55)	6.2 6 p < 0.001	32 (76)
Right paracingulate sulcus type 1 (PSC1)	28.4 5.2	41 (44)	28.2 6.3	8 (19)
Right paracingulate sulcus type 2 (PCS2)	47.7 N / A	1 (1)	41.6 2	2 (5)

2.5. Statistics

For the purpose of general morphology, we fused all the subparts of each measurement into one number and did the overall statistics. For the more detailed view of morphology, we performed separate statistics for each part of the parcellation of the sulci.

2.5.1. t-Test between Groups

Overall length differences between patients with schizophrenia and controls in the non-parcellated PCS and CS were calculated by t-test for groups, and separately for cingulate sulcus right (CS R) and left (CS L) and paracingulate sulcus right (PCS R) and left (PCS L).

2.5.2. Mann–Whitney U Test and Kruskal–Wallis Test

The differences in the length of the CS (1, 2, and 3) as well as PCS (0, 1, and 2) between patients with schizophrenia and controls were calculated by nonparametric Mann–Whitney U test and Kruskal–Wallis test (because of unequal numbers of subjects in each category).

2.5.3. ROC Curve Analysis

We used an online ROC analysis web-based calculator with the data format 5 selection. ROC curve analysis was performed for the CS L and the PCS R only (because of the significant t-test) (Figure 3).

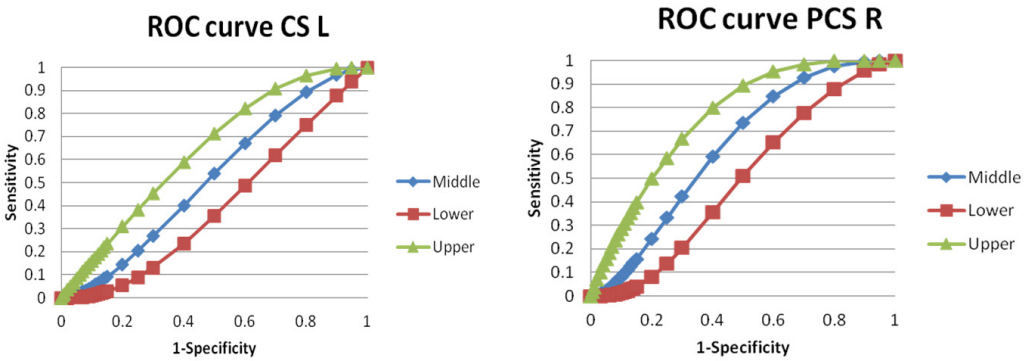

Figure 3. ROC curve analysis for length differences in left cingulate sulcus (CS L) and right paracingulate sulcus (PCS R) in schizophrenia patients vs. controls without morphological parcellation. The area under the fitted curve was 0.52 with SE = 0.056 (CS) and 0.63 with SE = 0.06 (PCS).

2.5.4. Chi-Squared Test and Cochran–Mantel–Haenszel Test

The differences between patients with schizophrenia and controls in their distribution within CS and PCS morphology were evaluated separately for the left and right hemispheres by a chi-squared test of the null hypothesis. The Cochran–Mantel–Haenszel test (bilateral) was used to calculate the null hypothesis, similarly to the chi-squared test, but with the sum of the left and right hemispheres results.

2.5.5. Generalized Additive Model

The differences between groups were also assessed in a formalized statistical model of GAM (generalized additive model) [37,38] of semiparametric nature, which allowed for careful adjustment of the group (control versus schizophrenia) effect to sex and age (age effect was modeled by penalized spline with penalty coefficient estimation via generalized cross validation) [39].

GAM and ANOVA/ANCOVA modeling, chi-squared and Cochran–Mantel–Haenszel testing was done in the R environment (R Core Team, Vienna, Austria [40]). Other statistics were calculated in Statistica v.6 software (StatSoft, Tulsa, OK, USA) and the ROC curve analysis by an online program (http://www.rad.jhmi.edu/jeng/javarad/roc/JROCFITi. html, accessed on 16 October 2022). Statistical significance is commented at the 5% level ($p < 0.05$).

2.5.6. Adjustment for Sex and Age

Adjustment for age and sex was performed by the generalized additive model for both patients with schizophrenia and controls for the left and the right side in the CS (1, 2, and 3) and the PCS (0, 1, and 2).

3. Results

3.1. Length of CS and PCS without Parcellation

Overall length differences of the CS and the PCS are shown in Table 4. The right hemisphere PCS was significantly longer in patients with schizophrenia compared to controls (19.4 10.2 mm vs. 12.1 12.4 mm).

Table 4. Left and right CS and PCS without parcellation overall length differences between schizophrenia patients and control groups. The data are presented as mean values SD in mm. Statistical significance was calculated by t-test for groups.

Brain Structures	Patients Length (mm)	Controls Length (mm)	p-Values
Left cingulate sulcus	112.4 16.3	111.5 18.8	n.s.
Right cingulate sulcus	114.7 22.7	116.6 24.4	n.s.
Left paracingulate sulcus	16.1 9.1	14.4 8.7	n.s.
Right paracingulate sulcus	19.4 10.2	12.1 12.4	$p < 0.001$

n.s. = non significant.

3.2. Length of Parcellated CS (1, 2, and 3) and PCS (0, 1, and 2)

Detailed analysis of the morphological subtypes of the CS and the PCS and their lengths in schizophrenia patients and controls are shown in Table 3. The length of CS3a in the left hemisphere was significantly longer in patients with schizophrenia (53.8 25.7 vs. 32.7 19.4 mm in controls) but in CS3c it was reversed—longer in controls (52.5 22.5 mm) compared to schizophrenia patients (36.2 12.9 mm), but without significance. The length of PCS0 in the right hemisphere was significantly longer in patients with schizophrenia (11.7 5.2 mm) compared to controls (6.2 6 mm) (it was not present at all).

3.3. Incidence and Distribution of Patients and Controls between CS and PCS Morphology Types

Table 5 shows the differences in numbers of patients with schizophrenia and controls for each CS and PCS morphology type and incidence of distribution of particular sulcal patterns within CS and PCS morphology. Higher incidences of appearance in patients compared to controls in CS1, PCS0, and PCS1 were observed in both hemispheres; a lower incidence in patients was observed in CS3 in both hemispheres; in CS2 on the left there was more incidence in controls compared to patients, and the opposite held true on the right—more in patients compared to controls (PCS2 in both hemispheres was not present).

Table 5. Comparison of patients and controls with CS1, 2, and 3 and PCS0, 1, and 2 types of morphology based on Table 3. The numbers show incidences (absolute values) of a particular morphology type in between patients with schizophrenia and controls. N/A—not applicable due to zero or low numbers of presence.

Group.	CS1 Left/Right	CS2 Left/Right	CS3 Left/Right	PCS0 Left/Right	PCS1 Left/Right	PCS2 Left/Right
Patients	61/58	2/30	6/5	63/51	30/41	N/A
Controls	6/5	17/19	19/19	34/32	8/8	N/A

The number of patients with schizophrenia who had concurrently present CS1 as well as PCS1 in both hemispheres was 9 (8.7%). The number of patients with PCS1 L and concurrently present CS1 L was 25 (83%); PCS1 R and concurrently, CS1 R was 28 (68%).

3.4. Adjustment for Age and Sex Performed by Generalized Additive Model

After the adjustment for age and sex, we found PCS on the right side to be significantly ($p < 0.001$) larger for schizophrenic patients than for controls (by about 7.346 on average). PCS on the left was not significantly different between patients and controls ($p = 0.304$). Similarly, CS did not differ significantly between patients and controls neither on the right ($p = 0.375$), nor on the left side ($p = 0.877$). The difference between PCS on the right and left (laterality of the PCS) was significantly larger for patients than for controls ($p = 0.019$)—by about 5.587 on average. Analogous laterality for CS was not significantly different between patients and healthy controls for CS ($p = 0.331$).

3.5. ROC Analysis Evaluation

ROC analysis was performed for statistically significant results of the length of the CS L and PCS R between patients and controls. For the CS L were estimates of binomial ROC parameters A = 0.097 with standard error (SE) (A) = 0.24, B = 1.36 with SE (B) = 0.19, and correlation (A, B) = 0.032. The area under the fitted curve was 0.52 with SE = 0.056, trapezoidal (Wilcoxon) area = 0.51 with estimated SE = 0.054. For the PCS, R were estimates of binomial ROC parameters A = 0.63 with SE (A) = 0.31, B = 1.58 with SE (B) = 0.26, and correlation (A, B) = 0.14. The area under the fitted curve was 0.63 with SE = 0.06, trapezoidal (Wilcoxon) area = 0.63 with estimated SE = 0.055 (Figure 3). Therefore, ROC analysis suggests that the practical classification schizophrenia patients and controls based only on the length of the CS L and PCS R is (obviously) far from being perfect.

4. Discussion

Numerous studies in the literature document the relationship between the morphological changes of the central nervous system and schizophrenia, e.g., cortical areas [41], amygdala [42], hippocampus [43], and others [44], but they are not suitable for morphological diagnosis of schizophrenia because of their non-specificity and frequent anatomical variability.

The CS and the PCS are two regions found within the ACC on the medial side of the brain hemisphere. Morphological variability of the PCS was described, for example, in [32]. Specificity of the morphological changes in ACC vs. other cortical areas were described by Fornito et al. [8]. Variability in the CS organization in human adult and fetal cadavers was described by Marinescu et al. [35]. The CS structure was analyzed in six groups of adult brains whose medial hemisphere was parcellated into I-III sectors, clockwise to the CS course. The major differences in the CS organization could be summarized into the following observations: in sector I the subgenual part of callosal body varies in the numbers and shape of the CS infoldings; in sector II there is broken trajectory of the CS by the dorsal cingulate-frontal infolding; and in sector III the trajectory is sinusoid and there is a convoluted aspect of the marginal branch. It is still difficult to account for these variations on the MRI where tiny details of the CS neuroanatomy are often blurred by the arachnoid.

4.1. Distribution of CS and PCS Morphological Patterns

We found significant differences between schizophrenia patients and controls in all types of the CS (1, 2, and 3) and the PCS (0, 1, and 2). Left-right asymmetries were not significant with the exception of PCS0 and PCS1 in schizophrenia patients. The most common in schizophrenia patients and controls was the presence of PCS0 morphology, followed by PCS1 and PCS2. Schizophrenia patients were found to have the most common CS1 morphology, followed by CS2 and CS3. This was in contrast with the control group, where the most common morphology was CS3 and CS2, followed by CS1. At least for the distribution of the morphological patterns of both PCS and CS, there are significant differences between schizophrenia patients and controls. The trend of these morphological distributions in healthy subjects described by Wei et al. [12] was similar to our results (although the effects of sex and handedness were included as well).

4.2. Length of the PCS

We found significantly longer non-parcellated PCS in the right hemisphere of schizophrenia patients compared to the control group. This is based on statistically significant difference only in the right PCS0 part in schizophrenia (see Table 3). Schizophrenia patients were reported to have a frequent absence of the left PCS. In healthy volunteers, prominent or present PCS was described more frequently in the left hemisphere compared to the right. On the contrary, schizophrenia patients were found to have no significant asymmetry and types prominent or absent. These all were found with the same frequency [27,28]. In our study, we found more often similar PCS1 in controls in the left hemisphere compared to the right. However, we did not observe enough cases of PCS2 (prominent) to create valid statements about their frequency neither in control nor in schizophrenia patients. We

observed left-right asymmetry in the PCS length in schizophrenia patients only and not in the control group. Leftward asymmetry was observed only in PCS0 (absent) and rightward asymmetry in PCS1 (present). This is also in contrast to the study by Le Prevost et al. [28]. Artiges et al. [45] measured the morphology of the PCS in relation to fMRI hypoactivation in the ACC in 13 patients with schizophrenia and 16 healthy controls. They did not observe a difference between healthy subjects and patients with the PCS (PCS1 and PCS2 in our classification), but patients with schizophrenia exhibited significant hypoactivation of the ACC, where the PCS was absent (PCS0 in our classification). According to our data, PCS0 were present in both schizophrenia patients and controls with the highest statistical occurrence, so that we support the notion that hypoactivation may take place even in the size of our studied group (patients with schizophrenia n = 93 and control group n = 42). The advantage of the Image J program is manual delineation, by which it is possible to distinguish the length of the PCS0 from 0 to 2 cm.

Shorter PCS (without parcellation) was observed in patients diagnosed with psychotic disease having hallucinations; they had shorter PCS compared to non-hallucinating psychotics and healthy controls [46].

In summary, we show that there is a reverse tendency in the PCS0 and PCS1 length between schizophrenia patients and controls. In PCS0 type morphology ("absent" type according to Yücel's nomenclature), we found a lower number of schizophrenic patients with the absent PCS compared to controls, regardless of the hemisphere (left 67% patients and 81% controls; right 55% patients and 76% controls). This finding is consistent with reports of [27,28]. We found the opposite for PCS1—a higher number of patients with schizophrenia having PCS1 type of morphology ("present" type according to Yücel's nomenclature) (left 32% patients and 19% controls; right 44% patients and 19% controls) compared to controls. These differences may explain the inconsistency between the observed leftward PCS hemispheric asymmetries in schizophrenia and healthy controls [47,48] versus reduced PCS asymmetries in schizophrenia patients [27,28] because of the intrinsic differences in both the CS and the PCS.

4.3. Length of the CS

It appears in schizophrenic patients that the CS is generally uninterrupted when viewed from the sagittal section, while in the control group this was rarely seen. On the contrary, the control group was almost equally split into half of participants having one and two interruptions of the CS. In other words, in the CS there is a reverse trend in the number of participants as for increase/decrease of the number of interruptions (in control groups the number of interruptions rises, while in schizophrenia patients it declines). It appears that it is an advantage to have an interrupted CS as opposed to the uninterrupted CS.

In summary, we show that there is a difference in length between CS1 and CS2 in schizophrenia patients and controls. In CS1 type morphology ("uninterrupted" type), we found a higher number of patients with schizophrenia with uninterrupted CS compared to controls, regardless of the hemisphere (left—66% patients and 14% controls; right—62% patients and 12% controls). On the contrary, in CS2 (one interruption) there was a higher number of controls compared to patients (left—41% controls and 26% patients; right—43% controls and 32% patients). In CS3, similarly to CS2, there was a higher number of controls than patients (left—45% controls and 6% patients; right—45% controls and 5% patients).

The length of the left CS3a was significantly longer in patients with schizophrenia, while the length of CS3c was longer in controls; CS3b did not differ between the groups. From the perspective of the study by Marinescu et al. [35], CS3a corresponds to sector I and CS3c to sector III. CS3a is close to the rostral area of the callosal body with the variability of connective infolding between the gyrus cinguli and the parolfactory area, and the infolding between gyrus cinguli and the rostral gyrus that continues with the gyrus frontalis superior. CS3c is the continuation of the main sulcal line into the marginal part of CS that also shows variability in the posterior cingulate-parietal connective infolding [35].

The length of the CS and PCS in the healthy population was described, for example, by Fornito et al. [47]; however, there are no such data in schizophrenia patients. We did not observe any gross morphological abnormalities of the CS and the PCS in schizophrenia patients, so we presume that the overall shape and morphology are not valid as clinical markers for the differential diagnosis of schizophrenia. On the contrary, the CS and the PCS length differ between both groups significantly, specifically, a decrease in length of the CS in schizophrenia patients is compensated by the length increase in the PCS. We found this valid for the right hemisphere only. Interestingly, we discovered two opposite trends in the left hemisphere. The length of CS3a was significantly longer in schizophrenia patients, while CS3c was significantly longer in controls. Our results partially correspond to the hypothesis of Rametti et al. [23], who studied the maximal depth and volume of the anterior cingulate sulcus and the PCS in 23 patients and 24 controls. However, they do not define the borders of the main measured area (the ACC) precisely in their study. The other difference is they used automated voxel-based morphometry measurements with manual correction, while we did all the measurements manually. The study found significant decrease in volume in the anterior cingulate sulcus in the left hemisphere and significant increase in the PCS volume in the right hemisphere of the patients with schizophrenia compared to controls [23].

The limitation of our study is the analysis of the sulcal shape that was performed in the sagittal plane view only. This way we may have missed invaginations of the CS in the white matter in a lateral direction. This could have led to the labeling of some sulci (CS2 and CS3) as interrupted; although they could have been present, if viewed on the coronal sections. Furthermore, general atrophy of the white matter in schizophrenia patients could lead to a merging of sulcus as a result of smoothening and unification of the surface cortical areas [49]. This observation could be supported by controls, who have relatively longer, although interrupted, courses of the CS. Another limitation is the demographic differences between the control group and the schizophrenia group; thus, analyzing a larger population sample may improve the understanding of CS and PCS morphology.

Delineation of the CS and PCS was done on MRI scans in sagittal projection—this is what clinicians would use, too. The problem with delineation of the ACC is that it is based on the cytoarchitectonic, post-mortem diagnosis. The posterior part of the ACC in the transition to the posterior cingulate gyrus (PCC) is difficult to evaluate on the MRI [50]. For this reason, it is not usable as a clinical diagnostic tool. We could not account for precise anatomical details of both sulci delineation, as described by, for example, Marinescu et al. [35], because their study was done on post-mortem brain tissue with many more anatomical details. Nevertheless, we described the Methods section in great detail so that it can be used as guidance for both sulci delineation on the MRI scans, which would minimize bias in interpretation of their occasionally variable course.

We analyzed each response separately, without corrections to multiple comparisons. This corresponds to univariate/marginal analyses and might lead to some inflation of falsely positive results. As we intend the study to be exploratory, or as a pilot study in the uncovered area, we do not want to be overly conservative. On the other hand, it is certainly in place to verify the significant findings on independent samples in the future.

Regarding the difference in educational attainment between the schizophrenia group and controls, other studies have shown that patients with schizophrenia have lower educational attainment than those without [51,52]. Attempts to create a pool of schizophrenia patients with the same level of education as controls is referred to in the literature as the "matching fallacy", as it can lead to the selection of atypical groups, such as patients with high education or, conversely, controls with low education [53,54].

4.4. Practical Use of CS and PCS Length as a Support Tool for Schizophrenia Diagnosis

The data in Table 3 could be useful as a guide for further MRI studies of schizophrenia. Depending on the MRI morphological typology of the CS and the PCS subsets in patients, it is possible to predict the following combinations of the medial hemisphere

sulcal appearance: (1) absent PCS and one of the CS type (1–3); (2) present PCS and one of the CS type (1–3); (3) prominent PCS and one of the CS type (1–3). Out of these, only the concurrent unilateral presence of PCS1 and CS1 in the left or the right hemisphere suggests a higher probability of schizophrenia. All other combinations point at the lack of disease. The morphological differences that we documented may potentially be of use as support tools demonstrating the differences present in schizophrenia. However, further research is required prior to implementing morphological measures as a support tool for schizophrenia diagnosis.

Brain ultrasound and magnetic resonance images of fetuses at 18–23 gestational weeks showing the structure of the sulcus cinguli suggest the possibility of comparing morphology between adult brains and possible changes in the ACC region from the prenatal period [55]. The deviation in cortical folding within the cingulate area suggests neurodevelopmental alterations within this area, albeit incomplete understanding of cellular, genetic, and experience-dependent plasticity behind aberrant cortical folding precludes, for the time being, conclusive statements about the neurobiological underpinnings of those changes. Given the current status of knowledge, further elucidation of the role of genes involved in driving the maturational trajectories of cortical patterning and the impact of events that disrupt fetal neurodevelopment are prerequisite for the whole understanding of those processes inflicting upon the composition of cortical architecture in schizophrenia.

5. Conclusions

Our study expands previously documented morphological classification of the sulcal patterns within the anterior cingulate area, especially the quantification of various morphology types of cingulate and paracingulate sulcus in patients with schizophrenia and the healthy population. Based on our results on ACC parcellation (CS1, 2, and 3; PCS0, 1, and 2), it is possible to postulate that the concurrent presence of PCS1 and CS1 in the left hemisphere as well as, to some extent, in the right hemisphere suggests a higher probability of schizophrenia. However, concurrent presence of PCS1 and CS1 in the left and right hemisphere at once is not very frequent.

Author Contributions: A.L.: investigation, data curation, and writing—original draft preparation. F.S.: data curation, formal analysis, and investigation. J.M.: methodology, formal analysis, and investigation. A.M.: critically revising the manuscript. M.B.: formal and statistical analysis. V.M.: visualization and critically revising the manuscript. P.Z.: conceptualization, methodology, formal analysis, investigation, funding acquisition, supervision, and writing—original draft preparation. All authors contributed to the article and approved the submitted version. All authors have read and agreed to the published version of the manuscript.

Funding: This research was funded by Charles University, grant Cooperatio 36—Medical Diagnostics and Basic Medical Sciences, Cooperatio 38—Neurosciences, Cooperatio 33—Intensive Care Medicine and grant 260388/SVV/2022; by Ministry of Health of the Czech Republic, grant number NU20-04-00393 as well as partially by the long-term strategic development financing of the Institute of Computer Science (Czech Republic RVO 67985807); by European Regional Development Fund-Project "Engineering applications of micro world physics" (Grant no. CZ.02.1.01/0.0/0.0/16019/0000766).

Institutional Review Board Statement: The Early-Stage Schizophrenia Outcome Study was approved by the Ethical Committee of the National Institute of Mental Health, Klecany, Czech Republic. The study was carried out in accordance with the latest version of the Declaration of Helsinki.

Informed Consent Statement: Informed consent was obtained from all subjects involved in the study.

Data Availability Statement: Not applicable.

Conflicts of Interest: The authors declare no conflict of interest.

References

1. Amiez, C.; Wilson, C.R.E.; Procyk, E. Variations of cingulate sulcal organization and link with cognitive performance. Sci. Rep. **2018**, 8, 13988. [CrossRef] [PubMed]
2. Haller, C.S.; Padmanabhan, J.L.; Lizano, P.; Torous, J.; Keshavan, M. Recent advances in understanding schizophrenia. F1000 Prime Rep. **2014**, 6, 57. [CrossRef] [PubMed]
3. Birnbaum, R.; Weinberger, D.R. Genetic insights into the neurodevelopmental origins of schizophrenia. Nat. Rev. Neurosci. **2017**, 18, 727. [CrossRef] [PubMed]
4. Rund, B.R. The research evidence for schizophrenia as a neurodevelopmental disorder. Scand. J. Psychol. **2018**, 59, 49–58. [CrossRef] [PubMed]
5. Chi, J.G.; Dooling, E.C.; Gilles, F.H. Gyral development of the human brain. Ann. Neurol. **1977**, 1, 86–93. [CrossRef]
6. Naidich, T.P.; Grant, J.L.; Altman, N.; Zimmerman, R.A.; Birchansky, S.B.; Braffmann, B.; Daniel, J.L. The developing cerebral surface. Preliminary report on the patterns of sulcal and gyral maturation—Anatomy, ultrasound, and magnetic resonance imaging. Neuroimaging Clin. N. Am. **1994**, 4, 201–240.
7. Feng, N.; Palaniyappan, L.; Robbins, T.W.; Cao, L.; Fang, S.; Luo, X.; Wang, X.; Luo, Q. Working memory processing deficit associated with a nonlinear response pattern of the anterior cingulate cortex in first-episode and drug-naïve schizophrenia. Neuropsychopharmacology **2022**. [CrossRef]
8. Fornito, A.; Yücel, M.; Dean, B.; Wood, S.J.; Pantelis, C. Anatomical abnormalities of the anterior cingulate cortex in schizophrenia: Bridging the gap between neuroimaging and neuropathology. Schizophr. Bull. **2009**, 35, 973–993. [CrossRef]
9. Brugger, S.P.; Howes, O.D. Heterogeneity and homogeneity of regional brain structure in schizophrenia: A meta-analysis. JAMA Psychiatry **2017**, 74, 1104–1111. [CrossRef]
10. Li, Q.; Yao, L.; You, W.; Liu, J.; Deng, S.; Li, B.; Luo, L.; Zhao, Y.; Wang, Y.; Wang, Y.; et al. Controllability of Functional Brain Networks and Its Clinical Significance in First-Episode Schizophrenia. Schizophr. Bull. **2022**. [CrossRef]
11. Smith, G.E. A New Topographical Survey of the Human Cerebral Cortex, being an Account of the Distribution of the Anatomically Distinct Cortical Areas and their Relationship to the Cerebral Sulci. J. Anat. Physiol. **1907**, 41, 237–254.
12. Wei, X.; Yin, Y.; Rong, M.; Zhang, J.; Wang, L.; Wu, Y.; Cai, Q.; Yu, C.; Wang, J.; Jiang, T. Paracingulate Sulcus Asymmetry in the Human Brain: Effects of Sex, Handedness, and Race. Sci. Rep. **2017**, 7, 42033. [CrossRef]
13. Amiez, C.; Sallet, J.; Novek, J.; Hadj-Bouziane, F.; Giacometti, C.; Andersson, J.; Hopkins, W.D.; Petrides, M. Chimpanzee histology and functional brain imaging show that the paracingulate sulcus is not human-specific. Commun. Biol. **2021**, 4, 54. [CrossRef]
14. Yücel, M.; Stuart, G.W.; Maruff, P.; Velakoulis, D.; Crowe, S.F.; Savage, G.; Pantelis, C. Hemispheric and gender-related differences in the gross morphology of the anterior cingulate/paracingulate cortex in normal volunteers: An MRI morphometric study. Cereb. Cortex **2001**, 11, 17–25. [CrossRef]
15. Paus, T.; Tomaiuolo, F.; Otaky, N.; MacDonald, D.; Petrides, M.; Atlas, J.; Morris, R.; Evans, A.C. Evans, Human cingulate and paracingulate sulci: Pattern, variability, asymmetry, and probabilistic map. Cereb. Cortex. **1996**, 6, 207–214. [CrossRef]
16. Ono, M.; Kubik, S.; Abarnathey, C.D. Atlas of the Cerebral Sulci; Georg Thieme: New York, NY, USA, 1990.
17. Nishikuni, K.; Ribas, G.C. Study of fetal and postnatal morphological development of the brain sulci. J. Neurosurg. Pediatr. **2013**, 11, 1–11. [CrossRef]
18. Meng, Y.; Li, G.; Wang, L.; Lin, W.; Gilmore, J.H.; Shen, D. Discovering cortical sulcal folding patterns in neonates using large-scale dataset. Hum. Brain Mapp. **2018**, 39, 3625–3635. [CrossRef]
19. Sun, Z.Y.; Perrot, M.; Tucholka, A.; Riviere, D.; Mangin, J.F. Constructing a dictionary of human brain folding patterns. In Proceedings of the Medical Image Computing and Computer-Assisted Intervention—MICCAI 2009, London, UK, 20–24 September 2009; Volume 12, pp. 117–124. [CrossRef]
20. Cachia, A.; Borst, G.; Tissier, C.; Fisher, C.; Plaze, M.; Gay, O.; Riviere, D.; Gogtay, N.; Giedd, J.; Mangin, J.F.; et al. Longitudinal stability of the folding pattern of the anterior cingulate cortex during development. Dev. Cogn. Neurosci. **2016**, 19, 122–127. [CrossRef]
21. Weinberger, D.R.; Marenco, S. Schizophrenia as A Neurodevelopmental Disorder. In Schizophrenia, 2nd ed.; Hirsch, S.R.W., Ed.; Blackwell Publishing: London, UK, 2003; pp. 326–348.
22. Woods, B.T. Is schizophrenia a progressive neurodevelopmental disorder? Toward a unitary pathogenetic mechanism. Am. J. Psychiatry **1998**, 155, 1661–1670. [CrossRef]
23. Rametti, G.; Junque, C.; Bartres-Faz, D.; Zubiaurre-Elorza, L.; Catalan, R.; Penades, R.; Bargallo, N.; Bernardo, M. Anterior cingulate and paracingulate sulci morphology in patients with schizophrenia. Schizophr. Res. **2010**, 121, 66–74. [CrossRef]
24. Fornito, A.; Yücel, M.; Wood, S.J.; Proffitt, T.; McGorry, P.D.; Velakoulis, D.; Pantelis, C. Morphology of the paracingulate sulcus and executive cognition in schizophrenia. Schizophr. Res. **2006**, 88, 192–197. [CrossRef] [PubMed]
25. Fujiwara, H.; Hirao, K.; Namiki, C.; Yamada, M.; Shimizu, M.; Fukuyama, H.; Hayashi, T.; Murai, T. Anterior cingulate pathology and social cognition in schizophrenia: A study of gray matter, white matter and sulcal morphometry. Neuroimage **2007**, 36, 1236–1245. [CrossRef] [PubMed]
26. Koo, M.S.; Levitt, J.J.; Salisbury, D.F.; Nakamura, M.; Shenton, M.E.; McCarley, R.W. A cross-sectional and longitudinal magnetic resonance imaging study of cingulate gyrus gray matter volume abnormalities in first episode schizophrenia and first episode affective psychosis. Arch. Gen. Psychiatry **2008**, 65, 746–760. [CrossRef] [PubMed]

27. Yücel, M.; Stuart, G.W.; Maruff, P.; Wood, S.J.; Savage, G.R.; Smith, D.J.; Crowe, S.F.; Copolov, D.L.; Velakoulis, D.; Pantelis, C. Paracingulate morphologic differences in males with established schizophrenia: A magnetic resonance imaging morphometric study. Biol. Psychiatry **2002**, 52, 15–23. [CrossRef]
28. Le Provost, J.B.; Bartres-Faz, D.; Paillere-Martinot, M.L.; Artiges, E.; Pappata, S.; Recasens, C.; Perez-Gomez, M.; Bernardo, M.; Baeza, I.; Bayle, F.; et al. Paracingulate sulcus morphology in men with early-onset schizophrenia. Br. J. Psychiat. **2003**, 182, 228–232. [CrossRef]
29. Marquardt, R.K.; Levitt, J.G.; Blanton, R.E.; Caplan, R.; Asarnow, R.; Siddarth, P.; Fadale, D.; McCracken, J.T.; Toga, A.W. Abnormal development of the anterior cingulate in childhood-onset schizophrenia: A preliminary quantitative MRI study. Psychiatry Res. **2005**, 138, 221–233. [CrossRef]
30. Meredith, S.M.; Whyler, N.C.; Stanfield, A.C.; Chakirova, G.; Moorhead, T.W.; Job, D.E.; Giles, S.; McIntosh, A.M.; Johnstone, E.C.; Lawrie, S.M. Anterior cingulate morphology in people at genetic high-risk of schizophrenia. Eur. Psychiatry **2012**, 27, 377–385. [CrossRef]
31. Buda, M.; Fornito, A.; Bergstrom, Z.; Simons, J.S. A specific brain structural basis for individual differences in reality monitoring. J. Neurosci. **2011**, 31, 14308–14313. [CrossRef]
32. Garrison, J.R.; Fernyhough, C.; McCarthy-Jones, S.; Haggard, M.; Simons, J.S. Paracingulate sulcus morphology is associated with hallucinations in the human brain. Nat. Commun. **2015**, 6, 8956. [CrossRef]
33. Destrieux, C.; Terrier, L.M.; Andersson, F.; Love, S.A.; Cottier, J.P.; Duvernoy, H.; Velut, S.; Janot, K.; Zemmoura, I. Practical guide for the identification of major sulcogyral structures of the human cortex. Brain Struct. Funct. **2017**, 222, 2001–2015. [CrossRef]
34. FIPAT. Terminologia Neuroanatomica. 2017. Available online: https://fipat.library.dal.ca/TNA/ (accessed on 12 July 2021).
35. Marinescu, I.; Melinte, P.R.; Dincă, I.; Pătrascu, E.; Botoran Mesină, M.I.; Drăgoi, G.S. Human gyrus cinguli as an anatomic marker in the neuronal system processing behavioural and cognitive act. Implications in forensic psychopathology. Rom. J. Leg. Med. **2018**, 26, 1–11. [CrossRef]
36. Garrison, J. Paracingulate Sulcus Measurement Protocol; University of Cambridge: Cambridge, UK, 2017. [CrossRef]
37. Hastie, T.J.; Tibshirani, R.J. Generalized Additive Models, 1st ed.; Chapman & Hall; CRC: London, UK, 1990.
38. Wood, S.N. Generalized Additive Models: An Introduction with R, 2nd ed.; Chapman & Hall; CRC: London, UK, 2017.
39. Wood, S.N.; Pya, N.; Saefken, B. Smoothing parameter and model selection for general smooth models (with discussion). J. Am. Stat. Assoc. **2016**, 111, 1548–1575. [CrossRef]
40. R Core Team. R: A Language and Environment for Statistical Computing; R Foundation for Statistical Computing: Vienna, Austria, 2019. Available online: https://www.R-project.org/ (accessed on 16 October 2022).
41. Vita, A.; Sacchetti, E.; Calzeroni, A.; Cazzullo, L.C. Cortical atrophy in schizophrenia. Prevalence and associated features. Schizophr. Res. **1988**, 1, 329–337. [CrossRef]
42. Mahon, P.B.; Eldridge, H.; Crocker, B.; Notes, L.; Gindes, H.; Postell, E.; King, S.; Potash, J.B.; Ratnanather, J.T.; Barta, P.E. An MRI study of amygdala in schizophrenia and psychotic bipolar disorder. Schizophr. Res. **2012**, 138, 188–191. [CrossRef]
43. Heckers, S. Neuroimaging studies of the hippocampus in schizophrenia. Hippocampus **2001**, 11, 520–528. [CrossRef]
44. Breier, A.; Buchanan, R.W.; Elkashef, A.; Munson, R.C.; Kirkpatrick, B.; Gellad, F. Brain morphology and schizophrenia. A magnetic resonance imaging study of limbic, prefrontal cortex, and caudate structures. Arch. Gen. Psychiatry **1992**, 49, 921–926. [CrossRef]
45. Artiges, E.; Martelli, C.; Naccache, L.; Bartres-Faz, D.; Leprovost, J.B.; Viard, A.; Paillere-Martinot, M.L.; Dehaene, S.; Martinot, J.L. Paracingulate sulcus morphology and fMRI activation detection in schizophrenia patients. Schizophr. Res. **2006**, 82, 143–151. [CrossRef]
46. Garrison, J.R.; Fernyhough, C.; McCarthy-Jones, S.; Simons, J.S.; Sommer, I.E.C. Paracingulate Sulcus Morphology and Hallucinations in Clinical and Nonclinical Groups. Schizophr. Bull. **2019**, 45, 733–741. [CrossRef]
47. Fornito, A.; Wood, S.J.; Whittle, S.; Fuller, J.; Adamson, C.; Saling, M.M.; Velakoulis, D.; Pantelis, C.; Yücel, M. Variability of the paracingulate sulcus and morphometry of the medial frontal cortex: Associations with cortical thickness, surface area, volume, and sulcal depth. Hum. Brain Mapp. **2008**, 29, 222–236. [CrossRef]
48. Noga, J.T.; Aylward, E.; Barta, P.E.; Pearlson, G.C. Cingulate gyrus in schizophrenic patients and normal volunteers. Psychiatry Res. **1995**, 61, 201–208. [CrossRef] [PubMed]
49. Kubicki, M.; McCarley, R.W.; Shenton, M.E. Evidence for white matter abnormalities in schizophrenia. Curr. Opin. Psychiatry **2005**, 18, 121–134. [CrossRef] [PubMed]
50. Rushworth, M.F.S.; Walton, M.E.; Kennerley, S.W.; Bannermann, D.M. Action sets and decisions in the medial frontal cortex. Trends Cogn. Sci. **2004**, 8, 410–417. [CrossRef] [PubMed]
51. Tesli, M.; Degerud, E.; Plana-Ripoll, O.; Gustavson, K.; Torvik, F.A.; Ystrom, E.; Ask, H.; Tesli, N.; Høye, A.; Stoltenberg, C.; et al. Educational attainment and mortality in schizophrenia. Acta Psychiatr. Scand. **2022**, 145, 481–493. [CrossRef]
52. Crossley, N.A.; Alliende, L.M.; Czepielewski, L.S.; Aceituno, D.; Castañeda, C.P.; Diaz, C.; Iruretagoyena, B.; Mena, C.; Mena, C.; Ramirez-Mahaluf, J.P.; et al. The enduring gap in educational attainment in schizophrenia according to the past 50 years of published research: A systematic review and meta-analysis. Lancet Psychiatry **2022**, 9, 565–573. [CrossRef]
53. Resnick, S.M. Matching for Education in Studies of Schizophrenia. Arch. Gen Psychiatry **1992**, 49, 246. [CrossRef]

54. Kremen, W.S.; Seidman, L.J.; Faraone, S.V.; Pepple, J.R.; Lyons, M.J.; Tsuang, M.T. The '3 Rs' and neuropsychological function in schizophrenia: A test of the matching fallacy in biological relatives. Psychiatry Res. **1995**, 56, 135–143. [CrossRef]
55. Ghai, S.; Fong, K.W.; Toi, A.; Chitayat, D.; Pantazi, S.; Blaser, S. Prenatal US and MR imaging findings of lissencephaly: Review of fetal cerebral sulcal development. Radiographics **2006**, 26, 389–405. [CrossRef]

10.1 Attachement no. 2

Co-author

2. ZACH, Petr; BARTOŠ, Aleš; **LAGUTINA, Anastasiya**; WURST, Zdeněk; GALLINA, Pasquale; RAI, Tanya; KIESLICH, Karel; RIEDLOVÁ, Jitka; IBRAHIM, Ibrahim; TINTĚRA, Jaroslav; MRZÍLKOVÁ, Jana. Easy identification of optimal coronal slice on brain magnetic resonance imaging to measure hippocampal area in Alzheimer's disease patients. *BioMed Research International*. 2020, (September), 5894021. ISSN 2314-6133. DOI: 10.1155/2020/5894021.

IF: 3.411/2020 (Q2/2020)

Hindawi
BioMed Research International
Volume 2020, Article ID 5894021, 6 pages
https://doi.org/10.1155/2020/5894021

Research Article

Easy Identification of Optimal Coronal Slice on Brain Magnetic Resonance Imaging to Measure Hippocampal Area in Alzheimer's Disease Patients

P. Zach,[1,2] **A. Bartoš**,[2,3] **A. Lagutina**,[1] **Z. Wurst**,[1] **P. Gallina**,[4] **T. Rai**,[1] **K. Kieslich**,[1] **J. Riedlová**,[1] **I. Ibrahim**,[5] **J. Tintěra**,[5] **and J. Mrzílková**[1]

[1]Department of Anatomy, Third Faculty of Medicine, Charles University, Prague, Czech Republic
[2]National Institute of Mental Health, Topolová 748, 250 67 Klecany, Czech Republic
[3]Department of Neurology, Third Faculty of Medicine, University Hospital Kralovske Vinohrady, Charles University, Prague, Czech Republic
[4]Department of Surgery and Translational Medicine, Neurosurgery Unit, Florence School of Neurosurgery, University of Florence, Florence, Italy
[5]Institute of clinical Clinical and Experimental Medicine, Prague, Czech Republic

Correspondence should be addressed to J. Mrzílková; jana.mrzilkova@lf3.cuni.cz

Received 4 June 2020; Accepted 3 August 2020; Published 24 September 2020

Academic Editor: Vida Demarin

Introduction. Measurement of an- hippocampal area or volume is useful in clinical practice as a supportive aid for diagnosis of Alzheimer's disease. Since it is time-consuming and not simple, it is not being used very often. We present a simplified protocol for hippocampal atrophy evaluation based on a single optimal slice in Alzheimer's disease. Methods. We defined a single optimal slice for hippocampal measurement on brain magnetic resonance imaging (MRI) at the plane where the amygdala disappears and only the hippocampus is present. We compared an absolute area and volume of the hippocampus on this optimal slice between 40 patients with Alzheimer disease and 40 age-, education- and gender-mateched elderly controls. Furthermore, we compared these results with those relative to the size of the brain or the skull: the area of the optimal slice normalized to the area of the brain at anterior commissure and the volume of the hippocampus normalized to the total intracranial volume. Results. Hippocampal areas on the single optimal slice and hippocampal volumes on the left and right in the control group were significantly higher than those in the AD group. Normalized hippocampal areas and volumes on the left and right in the control group were significantly higher compared to the AD group. Absolute hippocampal areas and volumes did not significantly differ from corresponding normalized hippocampal areas as well as normalized hippocampal volumes using comparisons of areas under the receiver operating characteristic curves. Conclusion. The hippocampal area on the well-defined optimal slice of brain MRI can reliably substitute a complicated measurement of the hippocampal volume. Surprisingly, brain or skull normalization of these variables does not add any incremental differentiation between Alzheimer disease patients and controls or give better results.

1. Introduction

Rating of medial temporal lobe atrophy is recommended in all current diagnostic guidelines [1]. However, it is seldom used in routine clinical dementia assessment. Total brain volume and volume-to-brain ratio in comparison to hippocampal and temporal horn measurements in traumatic brain injury showed hippocampal atrophy and temporal horn enlargement. The hippocampus and temporal horn volumes were inversely correlated in the group with traumatic brain injury [2]. The inverse relationship between the hippocampus and adjacent ventricle or the third ventricle is also used

for detection of Alzheimer's disease [3–9]. The measure of temporal atrophy (radial width of the temporal horn (rWTH)) was used to distinguish its asymmetry in AD patients [10]. Anatomical mapping of structural changes in AD showed more sensitive temporal horn expansion compared to hippocampal atrophy, but both maps correlated with clinical findings [11].

Our goal was to define single the most appropriate slice to measure the absolute hippocampal area, compare it with the hippocampal volume measurement, and find out whether normalization of the hippocampus to the area of the brain section, total intracranial volume, or skull area is useful in differentiation of AD patients and controls on MRI.

2. Material and Methods

2.1. Participants. Brain magnetic resonance imaging (MRI) and the Mini-Mental State Examination (MMSE) were examined in 80 individuals during our validation and normative study of the MMSE [12]. We included two groups of participants. The first group of patients ($n = 40$) was diagnosed with dementia due to Alzheimer's disease (AD) according to the National Institute on Aging-Alzheimer's Association (NIA-AA) criteria [13] at memory clinic of AD center, Department of Neurology, Charles University, Prague, Czech Republic. The second group of normal elderly controls (NC) ($n = 40$) had normal MMSE scores using our Czech norms and cut-offs for mild AD [12]. They were recruited mainly at Universities of Third Age (educational courses for seniors) or were spouses of the patients. Sociodemografic characteristics and cognitive scores of both groups are compared in (Table 1).

All participants signed informed consent. The research was approved by the Ethics Committee of the Prague Psychiatric Center/National Institute of Mental Health.

2.2. Acquisition of Magnetic Resonance Imaging. Brain MRI were acquired in 3D with scanner model SIEMENS TrioTim and software Syngo MR B13 4VB13A. Magnetic field strength was 3 T, voxel size 0:85 0:85 0:85 mm, slice thickness 0.85 mm, repetition time 2000 ms, echo time 4.73 s, scanning sequence GR/IR, acquisition matrix 320 384, and flip angle 10°. Participants were imaged at the Institute of Clinical and Experimental Medicine (IKEM), Prague, Czech Republic.

2.3. Specification of Optimal Brain Slice for Two-Dimensional Hippocampal Area Measurement Using Manual Delineation. In order to define hippocampal shrinkage on MRI for the clinical applications (dementia severity and its progression), we designed a protocol from a single coronal brain slice. We found gray matter located inside the temporal lobe (at the caudal part of the temporal horn of the lateral ventricle) by viewing the coronal slice on MRI in ventrodorsal orientation (Figure 1). Then, we located the amygdalar complex in the temporal lobe, below the lateral horn of the lateral ventricle. When we looked through coronal slices located more dorsally, we could see the hippocampus positioned below the amygdalar complex. With the increase in coronal slice numbers, we could see alveus in the caudal and lateral part of the hippocampus. Fimbria hippocampi was located on the top surrounded by several amygdalar nuclei. We considered the optimal coronal slice where amygdalar nuclei were no longer visible (at the level of fimbria hippocampi) so that we could observe the full extent of the hippocampus: alveus, dentate gyrus, and fimbria fornicis, located on the parahippocampal gyrus (Figure 2). In case of hippocampal atrophy, there was a significant reduction of both the gray and the white matter so that fissura hippocampi became clearly visible horizontally at the transition between the hippocampus and subiculum (part of parahippocampal gyrus).

Table 1: Characteristics of participants and group comparisons.

	AD group	Control group	p values
Numbers of participants	40	40	
Age at scan (years)	70:3 ± 6:8	67:8 ± 4:7	n.s.
Education (years)	13 ± 3	14 ± 3	n.s.
Male/female sex	13/27	15/25	n.s.
MMSE score (0-30 points)	21 ± 1	29 ± 4	<0.001

Data are expressed as the mean ± standard deviation. MMSE: Mini-Mental State Examination; n.s.: not significant.

2.4. Three-Dimensional Volumetry Using FreeSurfer Analysis. Images were processed using the most recent version of FreeSurfer (v6.0) software http://surfer.nmr.mgh.harvard.edu which creates virtual 3D reconstruction of human brain stacking slices of MR images in 3D space [14]. DICOM MR images from the MR scanner of the controls and the AD patients were converted into FS program .mgz files by mri_convert command. Full-image reconstruction (cortical and subcortical areas, brain stem, cerebrospinal fluid, ventricles, and white matter) was done by recon-all command. Then, brain structures were segmented due to different contrasts of brain tissue mapped on the Talairach atlas template derived from numerous human brains by creators of the software. The next step was the calculation of volumetric values of different brain structures. Volume datasets for statistical analysis were taken from /stats directory (aseg.stats, lh aparc.stats, etc.) within the FS program and exported into Statistica v.10 software. Two volumetric values were measured and calculated—an absolute volume of the hippocampus on the left and right and total intracranial volume (TIV).

2.5. Normalization of Hippocampal Area Measurements. The absolute area of the hippocampus in cm^2 separately for the left and right sides from a single optimal slice and absolute area of the brain and skull slice in the coronal section at the level of commissura anterior (CA) were manually delineated and calculated by an experienced neuroanatomist (JM) using FiJi (ImageJ software suite, https://imagej.net/Fiji).

The hippocampal area was normalized to the coronal section of the whole brain (and also the skull, unpublished data) at the level of the CA (in cm^2), separately for the left and right hippocampus, as the ratio of the hippocampal area in the optimal slice to the brain area at CA, multiplied by 100.

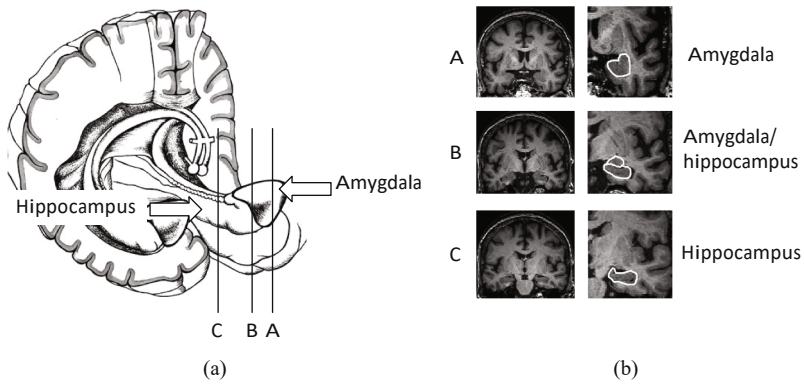

Figure 1: Three sections through the hippocampus and amygdala show their different proportions. Slice A through amygdala is the first notice/signal during viewing MRI slices from anterior/front to back. Slice B contains both hippocampal and amygdala areas on the slice, and it is not appropriate yet for evaluation. The optimal slice for hippocampal area measurement is slice C with the hippocampus only, without any part of amygdala. It is the first slice going back where amygdala disappears.

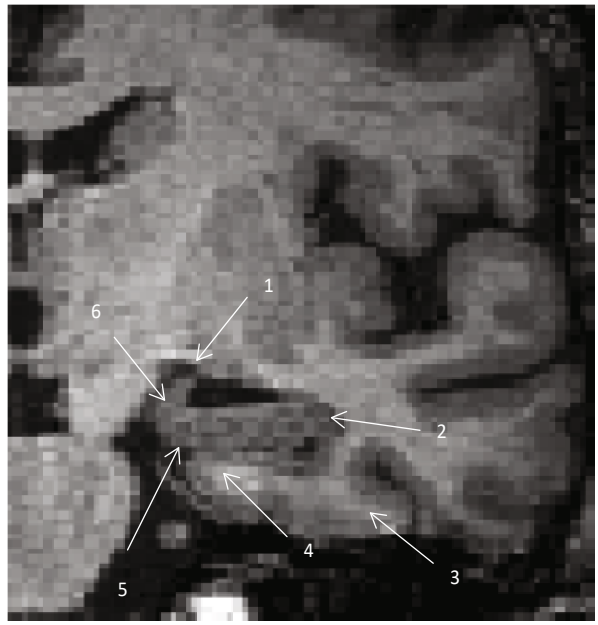

Figure 2: A detailed view of left mediotemporal structures on the optimal slice of brain MRI. Anatomical structures are labeled as follows: 1: hippocampal fimbria; 2: alveus; 3: parahippocampal gyrus; 4: subiculum; 5: hippocampal fissure; 6: uncus of the parahippocampal gyrus.

2.6. Normalization of Hippocampal Volume Measurements. The absolute volume of the hippocampus as well as total intracranial volume (TIV) in cm^3 was obtained by automated brain segmentation using FS (version 6.0 for Linux) [14, 15].

Intracranial volume, sometimes referred to as TIV, calculated from FreeSurfer (FS) was used for brain normalization, as described, e.g., in [16, 17]. We normalized the absolute hippocampal volumes to TIV separately for the left and right hippocampus as the ratio of hippocampal volume to TIV, multiplied by 100.

2.7. Statistics. A T-test for independent groups was used to calculate differences between the control and AD groups (grouping factor) and left and right sides (variables). The T-test was calculated separately for absolute hippocampal areas and volumes, hippocampal areas normalized to brain areas at CA and hippocampal volumes normalized to TIV. The T-test was used also for calculation of differences in demographic characteristics between the control and AD groups (mean ± standard deviation). Cohen's d test, AUC-ROC, and comparison of ROC curves evaluated differences between absolute and normalized measurements, separately for the left and right sides. The T-test was calculated in Statistica v.10 software, Cohen's d test in online Effect Size Calculator (https://lbecker.uccs.edu/), and AUC-ROC test in MedCalc v. 19.2.1. Statistical significance was accepted at $p \leq 0{:}05$.

3. Results

Table 1 shows that the AD patients were matched with the controls regarding age, education and sex, and significantly differed in MMSE scores.

Table 2: Absolute and normalized hippocampal areas and volumes in Alzheimer disease patients and controls.

Hippocampal measures	AD patients	Controls	p values	Cohen's d	AUC (SE)
Absolute measures (mm^2, mm^3)					
Area of the optimal slice on the left	118:1 ± 38:8	181:1 ± 25:7	<0.01	1.91	0.91 (0.0331)
Area of the optimal slice on the right	112:1 ± 40:2	169:6 ± 29	<0.01	1.64	0.87 (0.039)
Volume on the left (FreeSurfer)	2651 ± 746	3677 ± 948	<0.01	1.2	0.86 (0.0486)
Volume on the right (FreeSurfer)	2777 ± 930	3761 ± 760	<0.01	1.16	0.83 (0.0506)
Normalized measures (%)					
Area of the optimal slice on the left to brain area at anterior commissure	45:5 ± 11:8	63:6 ± 8:7	0.01	1.75	0.89 (0.034)
Area of the optimal slice on the right to brain area at anterior commissure	43:2 ± 13:3	59:5 ± 8:5	<0.01	1.46	0.85 (0.0416)
Volume on the left to TIV (FreeSurfer)	0:29 ± 0:09	0:35 ± 0:08	0.01	0.7	0.73 (0.061)
Volume on the right to TIV (FreeSurfer)	0:31 ± 0:12	0:42 ± 0:14	<0.01	0.84	0.78 (0.0551)

Absolute hippocampal areas in the optimal slice on the left and right are in mm^2. Absolute hippocampal volumes on the left and right are in mm^3. Normalized hippocampal areas of the optimal slice to the brain area at anterior commissure on the left and right and normalized hippocampal volumes to total intracranial volume (TIV) on the left and right are in percentages. All values are expressed as means ± standard deviations; SE means standard error of AUC (ROC).

Table 3: No differences were found between absolute and normalized measures using comparisons of areas under the receiver operating characteristic curves.

Absolute vs. normalized hippocampal measures	p value
Area on the left	0.7
Area on the right	1.0
Volume on the left	0.9
Volume on the right	0.5

3.1. Absolute Hippocampal Area and Volume. Hippocampal areas in the optimal slice on the left and right in the control group were significantly higher than those in the AD group ($p < 0:001$). Hippocampal volumes on the left and right in the control group were significantly higher than those in the AD group ($p < 0:001$) (Table 2).

3.2. Normalized Hippocampal Area and Volume. Normalized hippocampal areas on the left and right in the control group were significantly higher compared to the AD group ($p < 0:001$). Normalized hippocampal volumes on the left and right in the control group were significantly higher compared to the AD group ($p < 0:001$) (Table 2).

3.3. Comparison of Absolute and Normalized Hippocampal Areas and Volumes. Normalized hippocampal areas as well as normalized hippocampal volumes did not differ significantly from corresponding absolute hippocampal areas and volumes ($p > 0:5$) (Table 3).

4. Discussion

Our results show that hippocampal shrinkage in the AD patients could be reliably evaluated from the single coronal slice of the brain on the MRI and without normalization to the TIV or other brain measures. We combined manual and automated (FS) delineation of the hippocampus. It was found that there is high reliability and agreement between FreeSurfer and manual hippocampal protocols [18]. Our slice is at the level of the memory processing (ventral hippocampus) [19] but not at the level of 3D spatial navigation (dorsal hippocampus) [20]. Other studies used several slices and stages of Alzheimer's disease development but without having MRI slices precisely defined by space position of the anatomical structures [21]. These slices often seem to be localised at the level of the dorsal hippocampus.

Numerous protocols in clinical studies with Alzheimer's disease patients often use the hippocampus to brain TIV normalization [22, 23]. However, our results show that normalization is not necessary in order to evaluate hippocampal shrinkage as part of diagnosis. Possible mistake of total intracranial volume estimation by FS and suggestion for evaluation of intracranial volume by two intracranial areas and width are mentioned in [24, 25]. No effects of age-related changes on the MRI were observed in the temporal lobe width and temporal horn width measurements both on right and left sides [26]. Temporal horn volumes and temporal horn indexes measurements in AD were significant in AD compared to controls but not in MCI [4]. On the other hand, temporal horn expansion was found more reliable to predict conversion from MCI to AD than hippocampal volume alone because of smaller changes in it compared to the size of the temporal horn [27]. Other variants of a 2D single brain slice from which we could derive measurements of hippocampus atrophy represent study that measured manually 3 regions on coronal MRI at the level of the interpeduncular fossa to calculate the Medial Temporal Atrophy index [7]. Similarly, our design offers only one simple and easily distinguishable

marker that is enough for clinicians to analyze the optimal slice for Alzheimer's disease MRI diagnosis.

We also measured the area of the coronal slice of the skull at the same level as the area of the brain (at CA) to do experimental area normalization to the brain/skull ratio. We found a significantly lower brain area/skull area ratio in the AD group compared to the control group. Furthermore, another experimental normalization of hippocampal areas (left and right) to the brain area/skull area ratio showed similar results as the hippocampus to area of brain in CA normalization—significantly lower in the AD group compared to the control one. The same results showed the brain volume/skull volume ratio and normalization of the hippocampal volumes to brain volume/skull volume ratio (unpublished results). We did not include the above-mentioned data in the article because of similarity of results they revealed.

The limitations of our study include the normalization style we used. We normalized left and right hippocampal areas and volumes to the total brain area at the level of CA and total intracranial volume. TIV normalization does not make a difference between left and right hemispheres so that it compares right and left hippocampal volumes to the volume of the whole brain. More precise and valuable for the statistics would be comparison of hippocampal areas and volumes (left and right) to the area and volume of the corresponding left and right hemispheres, but this is not widely accepted.

5. Conclusion

We present a simplified protocol for hippocampal atrophy evaluation on MRI in Alzheimer disease based on single optimal coronal slice analysis. In order to prove it, we measured the absolute area of the hippocampus at the single optimal slice and compared it with the normalized area of the same slice. We found no difference between the hippocampal absolute and normalized area in control and AD patients. Similarly, we did not find a difference between absolute and normalized hippocampal volumes. We found that estimation of hippocampal shrinkage in Alzheimer disease on MRI could be reliably done without normalization.

Abbreviations

AD: Alzheimer's disease
AUC: Area under the curve (receiver operating characteristic)
CA: Anterior commissure
FS: FreeSurfer
MCI: Mild cognitive impairment
MRI: Magnetic resonance imaging
MMSE: Mini-Mental State Examination
rWTH: Radial width of the temporal horn
ROC: Receiver operating characteristic
TIV: Total intracranial volume.

Data Availability

All analyzed data are available upon request in the Institute of Anatomy, Third Faculty of Medicine, Prague, Czech Republic.

Conflicts of Interest

The authors declare that they have no conflicts of interest.

Authors' Contributions

Zach P worked on roles/writing (original draft); Bartoš A was assigned to participants selection, data collection and revisions of the manuscript; Lagutina A handled conceptualization; Wurst Z worked on software; Gallina P handled clinical verification; Rai T supervised the study; Kieslich K and Mrzílková J managed the methodology; Riedlová J worked on validation; Ibrahim I handled visualization; and Tintěra J managed the resources.

Acknowledgments

The project was supported by grants Q35, Q41, and 260388/SVV/2019 of Charles University, the Czech Science Foundation grant no. P30412G069; grants NV18-07-00272 and NV19-04-00090 of the Ministry of Health, and the project "Sustainability for the National Institute of Mental Health," under grant number LO1611, with a financial support from the Ministry of Education, Youth and Sports of the Czech Republic under the NPU I program, project CZ.02.1.01/0.0/0.0/16_019/0000766 and MH CZ-DRO ("National Institute of Mental Health (NIMH), IN: 00023752").

References

[1] L. Harper, F. Barkhof, N. C. Fox, and J. M. Schott, "Using visual rating to diagnose dementia: a critical evaluation of MRI atrophy scales," Journal of Neurology, Neurosurgery & Psychiatry, vol. 86, no. 11, pp. 1225–1233, 2015.

[2] E. D. Bigler, D. D. Blatter, C. V. Anderson et al., "Hippocampal volume in normal aging and traumatic brain injury," AJNR. American Journal of Neuroradiology, vol. 18, no. 1, pp. 11–23, 1997.

[3] A. Bartos, D. Gregus, I. Ibrahim, and J. Tintěra, "Brain volumes and their ratios in Alzheimer´s disease on magnetic resonance imaging segmented using Freesurfer 6.0," Psychiatry Research: Neuroimaging, vol. 287, pp. 70–74, 2019.

[4] F. L. Giesel, H. K. Hahn, P. A. Thomann et al., "Temporal horn index and volume of medial temporal lobe atrophy using a new semiautomated method for rapid and precise assessment," AJNR. American Journal of Neuroradiology, vol. 27, no. 7, pp. 1454–1458, 2006.

[5] F. L. Giesel, P. A. Thomann, H. K. Hahn et al., "Comparison of manual direct and automated indirect measurement of hippocampus using magnetic resonance imaging," European Journal of Radiology, vol. 66, no. 2, pp. 268–273, 2008.

[6] M. Menendez-Gonzalez, A. B. de Celis, J. Salas-Pacheco, and O. Arias-Carrion, "Structural neuroimaging of the medial temporal lobe in Alzheimer's disease clinical trials," Journal of Alzheimer's Disease, vol. 48, no. 3, pp. 581–589, 2015.

[7] M. Menéndez-González, A. López-Muñiz, J. A. Vega, J. M. Salas-Pacheco, and O. Arias-Carrión, "MTA index: a simple 2D-method for assessing atrophy of the medial temporal lobe using clinically available neuroimaging," Frontiers in Aging Neuroscience, vol. 6, p. 23, 2014.

[8] M. Menendez-Gonzalez, E. Suarez-Sanmartin, C. Garcia, P. Martinez-Camblor, E. Westman, and A. Simmons, "Manual planimetry of the medial temporal lobe versus automated volumetry of the hippocampus in the diagnosis of Alzheimer's disease," Cureus, vol. 26, no. 8, article e544, 2016.

[9] D. Schoemaker, C. Buss, S. Pietrantonio et al., "The hippocampal-to-ventricle ratio (HVR): presentation of a manual segmentation protocol and preliminary evidence," Neuroimage, vol. 203, article 116108, 2019.

[10] C. Geroldi, N. M. Akkawi, S. Galluzzi et al., "Temporal lobe asymmetry in patients with Alzheimer's disease with delusions," Journal of Neurology, Neurosurgery & Psychiatry, vol. 69, no. 2, pp. 187–191, 2000.

[11] P. M. Thompson, K. M. Hayashi, G. I. De Zubicaray et al., "Mapping hippocampal and ventricular change in Alzheimer disease," NeuroImage, vol. 22, no. 4, pp. 1754–1766, 2004.

[12] A. Bartos and M. Raisova, "The Mini-Mental State Examination: Czech norms and cutoffs for mild dementia and mild cognitive impairment due to Alzheimer's disease," Dementia and Geriatric Cognitive Disorders, vol. 42, no. 1-2, pp. 50–57, 2016.

[13] G. M. McKhann, D. S. Knopman, H. Chertkow et al., "The diagnosis of dementia due to Alzheimer's disease: recommendations from the National Institute on Aging-Alzheimer's Association workgroups on diagnostic guidelines for Alzheimer's disease," Alzheimer's and Dementia, vol. 7, no. 3, pp. 263–269, 2011.

[14] B. Fischl, D. H. Salat, E. Busa et al., "Whole brain segmentation: automated labeling of neuroanatomical structures in the human brain," Neuron, vol. 33, no. 3, pp. 341–355, 2002.

[15] M. Reuter, N. J. Schmansky, H. D. Rosas, and B. Fischl, "Within-subject template estimation for unbiased longitudinal image analysis," NeuroImage, vol. 61, no. 4, pp. 1402–1418, 2012.

[16] I. B. Malone, K. K. Leung, S. Clegg et al., "Accurate automatic estimation of total intracranial volume: a nuisance variable with less nuisance," NeuroImage, vol. 104, pp. 366–372, 2015.

[17] S. Sargolzaei, A. Sargolzaei, M. Cabrerizo et al., "A practical guideline for intracranial volume estimation in patients with Alzheimer's disease," BMC Bioinformatics, vol. 16, no. S7, p. S8, 2015.

[18] Y. L. Fung, K. E. T. Ng, S. J. Vogrin et al., "Comparative utility of manual versus automated segmentation of hippocampus and entorhinal cortex volumes in a memory clinic sample," Journal of Alzheimer's Disease, vol. 68, no. 1, pp. 159–171, 2019.

[19] A. Takashima, K. M. Petersson, F. Rutters et al., "Declarative memory consolidation in humans: a prospective functional magnetic resonance imaging study," Proceedings of the National Academy of Sciences of the United States of America, vol. 103, no. 3, pp. 756–761, 2006.

[20] B. S. Porter, R. Schmidt, and D. K. Bilkey, "Hippocampal place cell encoding of sloping terrain," Hippocampus, vol. 28, no. 11, pp. 767–782, 2018.

[21] F. Li, H. Takechi, R. Saito et al., "A comparative study: visual rating scores and the voxel-based specific regional analysis system for Alzheimer's disease on magnetic resonance imaging among subjects with Alzheimer's disease, mild cognitive impairment, and normal cognition," Psychogeriatrics, vol. 19, no. 2, pp. 95–104, 2019.

[22] S. Estévez-Santé, A. Jiménez-Huete, and ADNI group, "Comparative analysis of methods of volume adjustment in hippocampal volumetry for the diagnosis of Alzheimer disease," Journal of Neuroradiology, vol. 47, no. 2, pp. 161–165, 2020.

[23] X. Hu, D. Meiberth, B. Newport, and F. Jessen, "Anatomical correlates of the neuropsychiatric symptoms in Alzheimer's disease," Current Alzheimer Research, vol. 12, no. 3, pp. 266–277, 2015.

[24] N. Klasson, E. Olsson, C. Eckerström, H. Malmgren, and A. Wallin, "Estimated intracranial volume from FreeSurfer is biased by total brain volume," European Radiology Experimental, vol. 2, no. 1, 2018.

[25] N. Klasson, E. Olsson, C. Eckerström, H. Malmgren, and A. Wallin, "Delineation of two intracranial areas and the perpendicular intracranial width is sufficient for intracranial volume estimation," Insights Into Imaging, vol. 9, no. 1, pp. 25–34, 2018.

[26] I. Salk, M. H. Atalar, F. Sezer, H. Egilmez, A. Cetin, and M. Arslan, "An MRI study of age-related changes in the dimensions related temporal lobe," International Journal of Clinical and Experimental Medicine, vol. 7, no. 3, pp. 515–522, 2014.

[27] K. E. Macdonald, J. W. Bartlett, K. K. Leung, S. Ourselin, and J. Barnes, "The value of hippocampal and temporal horn volumes and rates of change in predicting future conversion to AD," Alzheimer Disease and Associated Disorders, vol. 27, no. 2, pp. 168–173, 2013.

10.1 Attachement no. 3

Co-author

3. WURST, Zdeněk; BIRČÁK KUCHTOVÁ, Barbora; KŘEMEN, Jan; **LAHUTSINA, Anastasiya**; IBRAHIM, Ibrahim; TINTĚRA, Jaroslav; BARTOŠ, Aleš; BRABEC, Marek; RAI, Tanya; ZACH, Petr; MUSIL, Vladimír; OLYMPIOU, Nicoletta; MRZÍLKOVÁ, Jana. Basal ganglia compensatory white matter changes on DTI in Alzheimer's disease. *Cells*. 2023, **12**(April), 1220. ISSN 2073-4409. DOI: 10.3390/cells12091220.

IF: 7.666/2021 (Q2/2021)

cells

MDPI

Article

Basal Ganglia Compensatory White Matter Changes on DTI in Alzheimer's Disease

Zdeněk Wurst [1,†], Barbora Birčák Kuchtová [2,†], Jan Křemen [1], Anastasiya Lahutsina [1], Ibrahim Ibrahim [3], Jaroslav Tintěra [3], Aleš Bartoš [4], Marek Brabec [5], Tanya Rai [1], Petr Zach [1,*], Vladimír Musil [6,*], Nicoletta Olympiou [1] and Jana Mrzílková [1]

1 Department of Anatomy, Third Faculty of Medicine, Charles University, Ruska 87, 100 00 Prague, Czech Republic
2 Klinik für Neurologie, Universitätsklinikum Schleswig-Holstein Campus Lübeck, Ratzeburger Allee 160, 23562 Lübeck, Germany
3 Department of Radiodiagnostic and Interventional Radiology, Institute for Clinical and Experimental Medicine, Videnska 1958/9, 140 21 Prague, Czech Republic
4 Department of Neurology, Third Faculty of Medicine, University Hospital Kralovske Vinohrady, Charles University, Ruska 87, 100 00 Prague, Czech Republic; ales.bartos@lf3.cuni.cz
5 Department of Statistical Modeling, Institute of Computer Science, Academy of Sciences of the Czech Republic, Pod Vodarenskou vezi 271/2, 182 07 Prague, Czech Republic
6 Centre of Scientific Information, Third Faculty of Medicine, Charles University, Ruska 87, 100 00 Prague, Czech Republic
* Correspondence: petr.zach@lf3.cuni.cz (P.Z.); vladimir.musil@lf3.cuni.cz (V.M.); Tel.: +420-267102494 (P.Z.); +420-267102532 (V.M.)
† These authors contributed equally to this work and share first authorship.

Abstract: The volume reduction of the gray matter structures in patients with Alzheimer's disease is often accompanied by an asymmetric increase in the number of white matter fibers located close to these structures. The present study aims to investigate the white matter structure changes in the motor basal ganglia in Alzheimer's disease patients compared to healthy controls using diffusion tensor imaging. The amounts of tracts, tract length, tract volume, quantitative anisotropy, and general fractional anisotropy were measured in ten patients with Alzheimer's disease and ten healthy controls. A significant decrease in the number of tracts and general fractional anisotropy was found in patients with Alzheimer's disease compared to controls in the right caudate nucleus, while an increase was found in the left and the right putamen. Further, a significant decrease in the structural volume of the left and the right putamen was observed. An increase in the white matter diffusion tensor imaging parameters in patients with Alzheimer's disease was observed only in the putamen bilaterally. The right caudate showed a decrease in both the diffusion tensor imaging parameters and the volume in Alzheimer's disease patients. The right pallidum showed an increase in the diffusion tensor imaging parameters but a decrease in volume in Alzheimer's disease patients.

Keywords: DTI; Alzheimer's disease; basal ganglia; white matter; compensatory changes

Citation: Wurst, Z.; Birčák Kuchtová, B.; Křemen, J.; Lahutsina, A.; Ibrahim, I.; Tintěra, J.; Bartoš, A.; Brabec, M.; Rai, T.; Zach, P.; et al. Basal Ganglia Compensatory White Matter Changes on DTI in Alzheimer's Disease. Cells **2023**, 12, 1220. https://doi.org/10.3390/cells12091220

Academic Editor: Damian Holsinger

Received: 9 March 2023
Revised: 17 April 2023
Accepted: 21 April 2023
Published: 23 April 2023

1. Introduction

Structural changes of the basal ganglia (BG) are typically the domain of the neurodegenerative diseases, such as Parkinson's disease (PD). Conversely, there are not many studies of the white matter (WM) changes around the principal BG (e.g., putamen, caudate and pallidum) in Alzheimer's disease (AD). In a three-year longitudinal study of AD, unilateral atrophy in the right caudate nucleus and bilateral atrophy in the putamen was reported [1]. However, after the progression of AD over time this atrophy was also found in the left caudate nucleus [1]. Besides the morphological changes, the differences in the BG perfusion were also found in AD. For example, hyperperfusion in the right putamen and in the head of the right caudate nucleus was observed in magnetic resonance imaging

s

(MRI) in AD [2]. Thus, it is plausible that changes in the perfusion of the BG may lead with time to hypo- or hypertrophy of the WM located nearby [3,4]. Even though these changes in the perfusion may be typical for vascular dementia, hyper-perfusion could lead to the opposite effect, such as an increase in the structural and functional parameters. In the carriers of the apolipoprotein E (APOE) epsilon 4 allele with AD, the regional blood supply to many areas of the cerebral cortex and subcortical structures was significantly and asymmetrically reduced. [5].

Both diffusion-weighted imaging (DWI) and diffusion tensor imaging (DTI) are promising methods that can be used to assess the microstructure of axonal bundles and depict the axonal integrity of both normal and pathological brain tracts based on the diffusion properties of the brain tissue [6].

In our previous study [7], we found a significant reduction in the diffusion tensor imaging parameters in the fornix of AD patients compared to controls, likely due to neuronal degeneration and white matter loss. However, we simultaneously observed a surprising increase in values of tractographic parameters in the subcallosal area and the paraterminal gyrus in the patients with AD compared to the control group. Our explanation was that the patients with AD compensate for the loss of the ability to consolidate memory by redirecting and utilizing other structures, such as the subcallosal area and the paraterminal gyrus, especially if the fornix fibers are affected at the same time.

Given our previous data on DTI-based tractography demonstrating asymmetrical compensatory changes in the white matter structure of the subcallosal area and the paraterminal gyrus in AD patients, the present research aimed to determine whether there are compensatory changes in the findings related to the white matter diffusion tensor imaging data in the motor basal ganglia of the AD patients compared to the healthy controls. Our hypothesis was that the AD patients would show an increase in the DTI parameters (NT and/or QA) in some but not all of the BG compared to the healthy controls.

2. Materials and Methods

2.1. Subjects/Participants

In this study, we recruited 10 patients with a confirmed AD diagnosis and 10 healthy controls (Table 1). MRI and mini-mental state examination (MMSE) tests were performed on all subjects at the Alzheimer's Disease Center, Department of Neurology, Third Faculty of Medicine, Charles University, Prague, Czech Republic. For the purpose of the study, we used two groups of participants: (1) patients with mild cognitive impairment and dementia caused by AD according to NIA-AA criteria [8,9] and (2) cognitively normal older adults. At the beginning of the study, there was a separate third MCI patient group, which was classified as the AD group later since all the MCI group participants got diagnosed with AD by the end of the study. The AD diagnosis was made by an experienced neurologist through a thorough neurological and neuropsychological examination, functional assessments, blood work-up, brain MRI, single photon emission computed tomography (SPECT), and measurements of the total and phosphorylated tau proteins as well as -amyloid peptides in the cerebrospinal fluid upon the patients' consent to a lumbar puncture [10]. Most patients with the diagnosis were followed up for several years before they showed a cognitive and functional decline. Adults (controls) with normal cognitive abilities were recruited for the study at the University of the Third Age (adult education courses) of the Third Faculty of Medicine, Charles University, Czech Republic. These had normal MMSE scores (given recent Czech norms and limits) for mild AD [11]. In the control group, only those who were over 70 years of age were selected in order to stay consistent with the age of the AD patients. For a more detailed description, see our previous article [6]. The research was approved by the Ethics Committee of the Prague Psychiatric Center/National Institute of Mental Health and the Human Ethics Committee of the Third Faculty of Medicine, Charles University, Prague, Czech Republic, (Protocol No. 2016/3), and informed consent was obtained for all patients according to the Declaration of Helsinki.

Table 1. Characteristics of A D and control group.

	A D Group	Control Group	p Values
Numbers of participants	10	10	
Age at scan (years)	70.1 6.5	67.6 4.2	n.s
Education (years)	13 1	14 6	n.s
Male/female sex	6/10	5/10	n.s
MMSE score (0–30 pts.)	21 3	29 8	p < 0.001

Data are expressed as mean standard deviation. MMSE—the Mini-Mental State Examination, n.s.—not significant.

2.2. MRI Data Acquisition

All the recruited subjects in the present study were scanned on a 3T MRI scanner (Siemens Magnetom Trio, Erlangen, Germany) using a 24-channel head coil (adaptive coil combine mode was used) according to the following procedure:

(1) T1-weighted 3D MPRAGE had the following parameters: voxel size of 0.85 0.85 0.85 mm^3, 192 sagittal slices, TE of 4.73 ms, TR of 2000 ms, flip angle of 10, FOV of 326 mm, and TA:10:42 min.

(2) 3D T2-weighted FLAIR had the following parameters: voxel size of 1 1 1 mm^3, 176 sagittal slices, TE of 422 ms, TR of 6000 ms, FOV of 256 mm, and TA: 6:38.

(3) Diffusion-weighted images using SE EPI sequence had the parameters: voxel size of 2 2 2 mm^3, TR of 6000 ms, TE of 93 ms, 44 axial slices, three averages, FOV of 256 mm, number of diffusion directions 20, and two b values: 0, 1000 s/mm^2, TA: 6:38 min.

2.3. DTI Analysis

The DTI data were adjusted for distortion and countercurrents using the FSL Studio program (www.fmrib.ox.ac.uk/fsl/index.html, accessed on 8 March 2023). For correction of the head motion and eddy current distortion, the Eddy program within FSL (version 6.0.1) was used [12]. The DTI image set having b = 0 EPI was co-registered to T1-weighted 3D MPRAGE to obtain a co-registration matrix; this was further used for other EPI diffusion images. FLIRT (FMRIB's Linear Image Registration Tool), which is a fully automated robust tool for affine (linear) inter- and intra-modal registration, was used [13]. A Tri-Linear interpolation method in the final (reslice) transformation was performed using FLIRT/Advanced Options.

The potential influence of various factors leading to bias (e.g., use of only one MRI scanner or system errors) or distortion in the results is discussed in our previous article [7].

2.4. Anatomical Considerations

All the analyzed BG structures were manually delineated by two experienced anatomists to precisely differentiate between the GM and the WM structures (the internal and the external capsule). All the DTI parameters were measured on the WM surrounding the BG, although the BG themselves were used as a landmark for the anatomical orientation in the WM (see the supplementary material videos: R caudate ROI, R pallidum ROI, and L putamen ROI).

2.5. DTI Data Reconstruction

The diffusion-weighted imaging (DWI) data were first corrected for distortions and countercurrent effects using the FSL; then, the data were evaluated in the DSI studio using the generalized q-sampling imaging (GQI) algorithm with the Q-space diffeomorphic reconstruction (QSDR), thus reconstructing the data in the MNI space. QSDR is a model-free method that calculates an approximate density distribution of diffusing water in a standard space to preserve the orientation of fibers so that they can be traced [14]. The diffusion gradient table (see the Supplement Table S1) was rotated for each data unit according to the co-registration matrix before proceeding with the QSDR.

2.6. Tractography

The fiber tracking was performed using the following tracking parameters: the anisotropy (nQA) threshold was set at 0.05, the angular threshold was 60, and the step size was 1 mm. The tracts that were less than 60 mm in length were not counted. A total of 1,000,000 seeds were placed. The obtained values were used for further statistical procedures.

2.7. Measured Parameters

The DTI tractography resulted in the following values and parameters: the number of tracts (NT), tract length (TL), tract volume (TV), quantitative anisotropy (QA) as a marker of the tract directionality, and general fractional anisotropy (GFA) as a marker of the tract connectivity (Table 2). These parameters were analyzed further.

Table 2. Overview of the DTI parameters in patients with Alzheimer's disease and controls. NT = the number of tracts, TL = tract length, TV = tract volume, QA = quantitative anisotropy, nQA = normalized quantitative anisotropy, GFA = generalized fractional anisotropy, unit = stands for absolute numbers, AD = Alzheimer's disease patients, ctrl = healthy control group. The data are reported as mean values standard deviation (SD); * p 0.01, ** p 0.001.

	NT (Unit)	nQA (Unit)	TV (mm^3)	GFA (Unit)	QA (Unit)	TL (mm)
right caudate ctrl	10,945 2816 *	0.13 0.05	46,594 16,341	0.1 0.004	0.6 0.13	71 11.1
right caudate AD	7667 3557 *	0.17 0.05	39,382 18,303	0.09 0.006	0.62 0.13	68.6 15
left caudate ctrl	13,873 3813	0.13 0.05	55,388 16,471	0.1 0.005 0.1	0.61 0.13	77.6 8.1
left caudate AD	10,527 5558	0.18 0.06	46,135 21,453	0.01 0.11	0.66 0.15	74.6 16.2
right pallidum ctrl	18,202 3649 **	0.15 0.06 *	87,140 30,651	0.003 0.11	0.68 0.1	110 16.8
right pallidum AD	24,882 5633 **	0.21 0.05 *	107,239 23,390	0.003 0.11	0.74 0.14	115.8 16
left pallidum ctrl	20,728 4002	0.15 0.06 *	92,296 23,687	0.005 0.11	0.7 0.09	116.3 13.4
left pallidum AD	24,105 6108	0.21 0.05 *	102,759 23,521	0.005 0.1	0.74 0.15	117.8 19.3
right putamen ctrl	27,172 5618 **	0.13 0.05 *	102,896 35,726	0.004 0.1	0.62 0.12	98.2 15.9
right putamen AD	38,715 9724 **	0.19 0.05 *	127,691 30,643	0.005 0.1	0.7 0.12	104 9.7
left putamen ctrl	35,368 4250 *	0.15 0.06 *	115,491 23,729	0.004	0.68 0.11	104.6 11.3
left putamen AD	42,603 9387 *	0.2 0.05 *	128,184 29,395	0.1 0.007	0.74 0.16	107.8 15

2.8. FreeSurfer Volume Analysis

The MRI images were processed with the latest version of the freely available reconstruction software FreeSurfer (FS) (version: v6.0; http://surfer.nmr.mgh.harvard.edu (accessed on 8 March 2023)). This software creates a virtual 3D reconstruction of the brain structures from magnetic resonance images [15]. The DICOM MRI images from the AD patients and controls were transferred to the FS software environment in a standard way. For the purpose of the study, the values of the basal ganglia volumes, and the total brain volume (white and grey matter) were used. After processing, all the data were stored in an Excel spreadsheet for further statistical evaluation.

2.9. Statistical Analysis

The statistical analysis was performed using the STATISTICA 13 software and the R statistical computing environment [16]. The two-way ANOVA with repeated measures was applied for the analysis of the two independent groups (the AD patients and controls) and the two dependent variables (the left and the right side). The Wilks lambda test was used to evaluate the differences between the AD and control groups with the left and right sides as variables for both the DTI analysis and the FreeSurfer volumetric analysis (Tables 2 and 3). Pearson correlation coefficients were calculated to assess the relationship between the measures taken for the same person at different locations (Figure 1). Subsequently, we tested the differences in these correlations computed in the AD and control groups separately,

using the Fisher z-transform [17] and the two-sided test (for which we cite p-values). In particular, we tested the AD versus control difference in correlations for both the number of tracts and the connectivity characteristics, comparing—(i) the laterality (correlating the left and the right value of the same patient) of the putamen, pallidum, and the caudate, (ii) the structure (correlating the putamen, pallidum, and the caudate, separately for the left and right hemisphere), and then (iii) the structure segmentation volume (correlating the brain segmentation volumes in the putamen, pallidum, and the caudate, separately for the left and right hemisphere), plus (iv) the number of tracts/connectivity related to the volume of the putamen, pallidum, and the caudate. We acknowledge that different characteristics (like the number of tracts on the left and on the left) might be, to some extent, correlated.

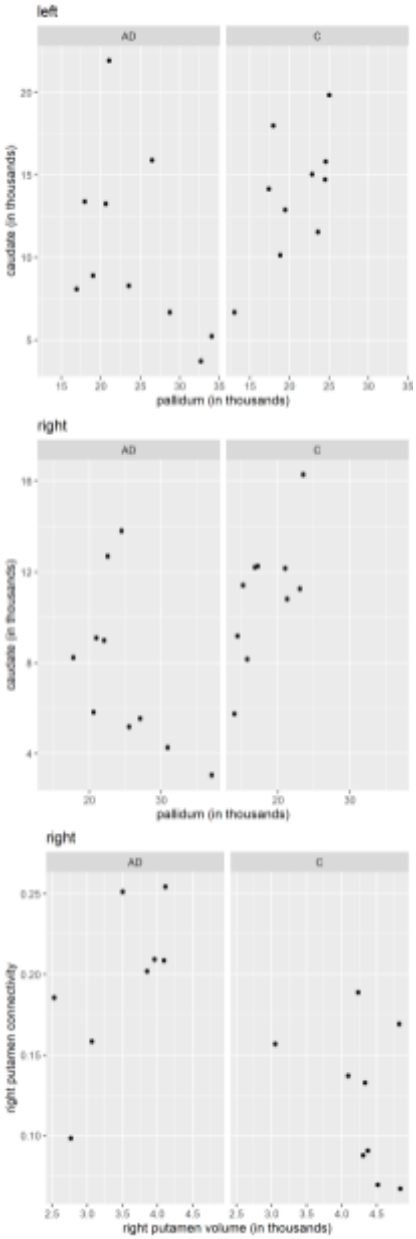

Figure 1. Comparison of the number of tracts, connectivity, and volume in the caudate, pallidum, and putamen (Pearson correlation coefficients). Upper panels: left pallidum vs. left caudate, number of tracts. Middle panels: right pallidum vs. right caudate, number of tracts. Bottom panels: right putamen volume vs. right putamen connectivity. AD—Alzheimer's disease patients; C—controls. Values on the x- and y-axis are reported in absolute units.

Table 3. The difference in the basal ganglia structures volumes and the total brain volume in Alzheimer's disease patients and controls as estimated by FreeSurfer. The values are reported in m^3, n.s. = not significant.

Structure	AD Patients	Controls	p-Value
left caudate	3016.7	3304.8	n.s.
left putamen	3656.5	4302.2	p = 0.01
left pallidum	1843.1	1747.9	n.s.
right caudate	3043.4	3321.4	n.s.
right putamen	3487.3	4283.9	p = 0.01
right pallidum	1897.5	1813.8	n.s.
brain segmentation volume	10.1 10^5	10.37 10^5	n.s.

The volume datasets from the FS program were extracted, converted into Excel spreadsheets, and subsequently processed in the STATISTICA software.

3. Results

The age, education, sex, and MMSE score comparison between the AD patients and the healthy controls are shown in Table 1. The samples of the 3D rotatory videos of the caudate, pallidum, and putamen DTIs, as well as their ROIs, are included in the supplementary material (Caudate AD, Caudate ctrl, Pallidum AD, Pallidum ctrl, Putamen AD, Putamen ctrl; R caudate ROI, R pallidum ROI, L putamen ROI).

3.1. DTI Analysis

Differences between the AD patients and the healthy controls were observed only in the NT and the normalized quantitative anisotropy (nQA). There were no significant differences in the TL, TV, and QA, as reported in Table 2.

3.2. Number of Tracts (NT)

Compared to the controls, the patients with AD (AD SD/ctrl SD) showed decreased NT in the right caudate (7667 3557/10,945 2816) and increased in the right pallidum (24,882 5633/18,202 3649), the right putamen (38,715 9724/27,172 5618, and the left putamen (42,603 9387/35,368 4250) (Figure 2, Table 2).

3.3. Normalized Quantitative Anisotropy (nQA)

Patients, compared to controls, showed higher nQA values in the right pallidum (0.21 0.05/0.15 0.06), left pallidum (0.21 0.05/0.15 0.06), right putamen (0.19 0.05/0.13 0.05), and the left putamen (0.2 0.05/0.15 0.06) (Table 2).

3.4. FreeSurfer Volume Analysis

The differences between the patients with AD and the controls were observed in the volume of the left and right putamen and in the nucleus accumbens area. On the other hand, no significant differences were observed in the left and right caudate nucleus and also in the brain segmentation volume. Further, a volume decrease in the right and left putamen was found in the AD patients in comparison to controls (respectively, 3487.3 m^3 vs. 4283.9 m^3 and 3656.5 m^3 vs. 4302.2 m^3), as reported in Table 3.

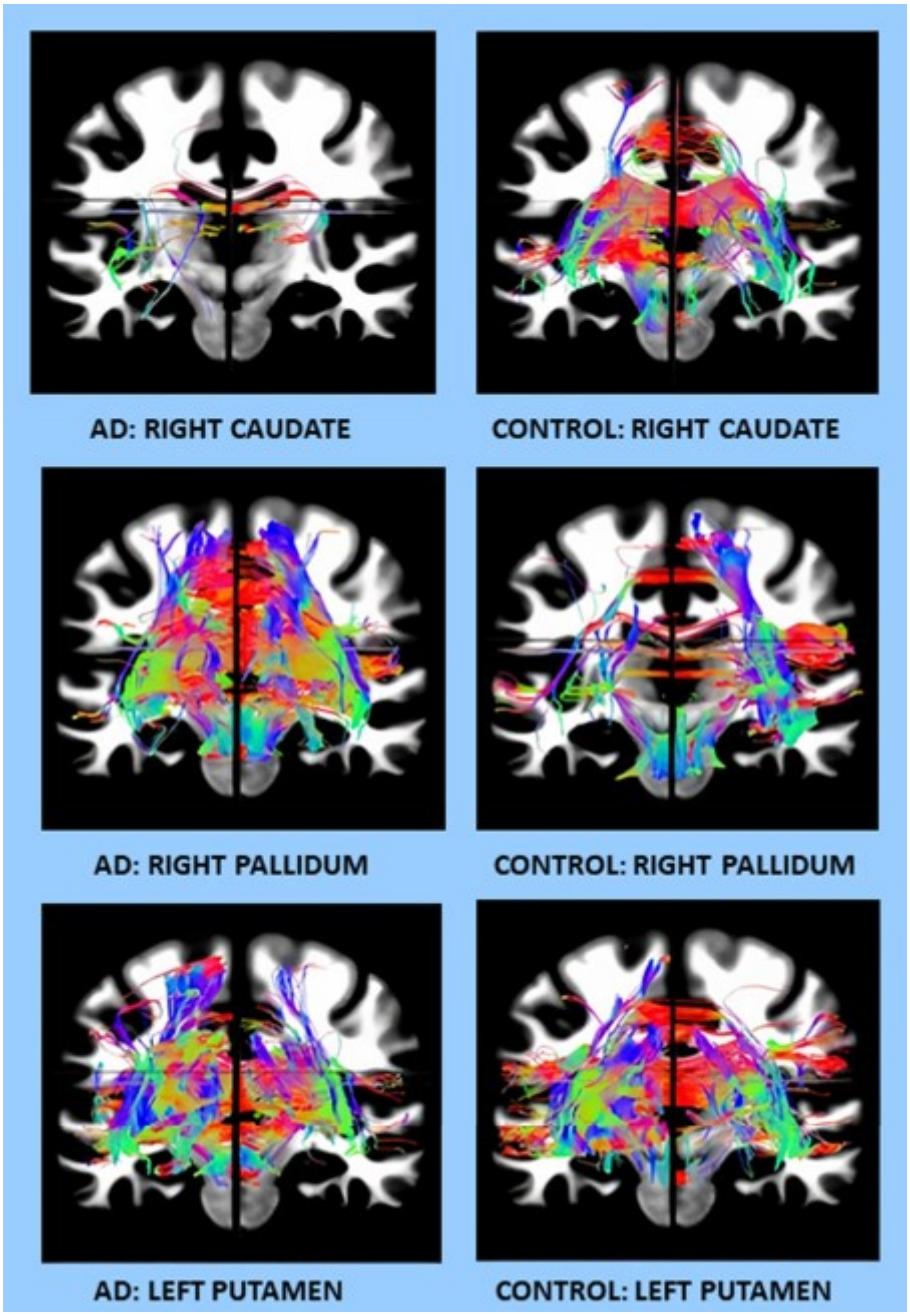

Figure 2. Examples of DTI changes in AD patients compared to controls on coronal sections for different brain regions (the right caudate, right pallidum, and the left putamen).

3.5. Pearson Correlation Coefficients

Significant changes in the correlations of several characteristics were observed between the patients with AD and the controls. In particular, the correlation between the number of tracts in the left pallidum and the number of tracts in the left caudate was 0.609 for the controls and 0.493 for the AD patients. The difference was highly significant, with the p-value = 0.019. The correlation between the number of tracts in the right pallidum and the number of tracts in the right caudate was 0.691 for the controls and 0.566 for the AD patients; hence, their difference was highly significant, p-value = 0.005. The correlation between the right putamen connectivity and the right putamen volume was 0.367 for the controls and 0.678 for the AD patients; hence, their difference was significant, with the p-value = 0.04. The qualitative differences in correlation patterns between the AD patients and the controls are shown graphically in Figure 1.

4. Discussion

DTI is challenging, and the fiber tract reconstruction depends on the quality of the diffusion data. The theoretical basics and a number of factors influencing the reconstruction results are covered in the literature [18,19].

For example, the gradient field inhomogeneity causes artifacts that affect the results of the reconstructed fibers. The gradient field can be efficiently mapped using the b-matrix spatial distribution in DTI (BSD-DTI) technique to correct the magnitude and the direction of the diffusion gradient [20].

In our study, the nQA parameter has been used for the fiber tracking (FT) instead of the FA due to the fact that QA-aided tractography has reached a better resolution and is less sensitive to partial volume effects of the crossing fibers than the tractography based on the FA [21]. FA is defined for all the fiber populations within a voxel and suffers from the partial volume effect.

Therefore, the data were reconstructed using the DSI studio with the GQI method. GQI is a free model that can be applied to any diffusion scheme that provides a quantitative anisotropy (QA) parameter, which is based on the spin distribution function (SDF) of diffusing water at different orientations. QA measures the spin density of anisotropy along a fiber pathway for each fiber population and contributes to more reliable tractography. QA can be normalized (nQA), which stabilizes the proton density across subjects [22].

An increase in values of the quantitative DTI parameters in the WM of the AD patients was observed only in the left and the right putamen, while their volumes were reduced compared to the controls. The right caudate showed, as expected, a decrease in both the DTI parameters and the volume in the AD patients compared to the controls. The right pallidum showed, similarly to the putamen, an increase in the DTI parameters but a decrease in volume in the AD patients compared to the controls.

An increase in the values of the quantitative DTI parameters of the WM observed in AD patients suggests the plasticity of specific tracts. The question is whether the whole process should be labeled as degeneration. Deposition of the amyloid plaques and deposits is typically present at the inferior part of the temporal lobe and the posterior cingulum [10,23]. These are also anatomical targets of the projections that undergo the WM hypertrophy or increase in the tract fibers on the DTI.

Why is there a decrease in the number of tracts in the caudate nucleus but an increase in the pallidum and the putamen? When considering the loops of the BG circuits, the motor loop skips the caudate nucleus but not the pallidum and the putamen. On the contrary, the executive/associative loop of the BG skips the putamen but deploys the caudate nucleus [24]. Since the motor skills are not affected in the early and mid-stages of AD, while cognition and memory decline, the observed compensatory WM hypertrophy in the putamen and the pallidum does not seem to be effective even though it is present. Since the caudate nucleus inhibits the pallidum, the increase in the WM of the pallidum could be due to its spontaneous activation after the caudate atrophies.

Given that the caudate is evolutionarily older compared to the relatively younger putamen [25], we hypothesize that the caudate could be the first to suffer the loss of structure and function. Thus, the putamen may not undergo neurodegeneration so easily; it could stay intact for longer and may, to some extent, substitute for the loss of function of the caudate. However, the observed caudate/putamen volume ratio in early caudate dysfunction in PD patients suggests this is not the case [26]. Although the WM compensatory changes in AD on the DTI were not described frequently, they were observed in PD [27], Tourette's syndrome [28], schizophrenia, and bipolar disorder [29,30]. Interestingly, increased connectivity in the right caudate nucleus was observed in cognitively normal PD patients [31].

Recently, we proposed that an increase in values of the quantitative DTI parameters of the WM in the subcallosal area and the paraterminal gyrus is an aftermath of the hippocampal atrophy [7,32]. We now propose another structural/functional compensatory mechanism for hippocampal atrophy in AD in terms of the BG white matter volume

increase. The reason for this compensatory hypertrophy could be their participation in the association loop of the BG circuit (association cortex—BG—thalamus—cortex). This circuit is responsible not only for motor skills but also for memory formation (emotional memory and positive reward reaction, episodic memory, and association cortices bound to memory formation).

In AD, attention has been paid to the brain areas with clinically proven morphological atrophy (the hippocampus, various cortical areas, the brain stem, and others). Recently, there were attempts to include clinical diagnostics and atrophy of neuroanatomical heterogeneous areas, i.e., basal forebrain cholinergic system [33].

We suggest another option: what if there are numerous compensatory shifts in motor/association/sensory and other brain structures, including the tracts in AD patients, detectable on the DTI (such as NT, TL, TV, QA, and GFA) that manifests by default when the atrophied primary memory circuits fail to work properly?

Limitations of the study: A small sample size (10 subjects) of our study represents some limitations; the observed asymmetric changes may be the result of a small sample, and further study with more patients is needed to confirm our conclusions. White matter changes around the basal ganglia were not specifically parcellated into the afferents or the efferents, nor were they classified into any kind of intrinsic or extrinsic projections in regards to the cortex, the brain stem, or the diencephalon. This way, it was compared only to the sum of three-directional projections between the AD patients and the controls. For future research it would be good to compare the DTI-based tractography of separate tracts and pathways of the BG in AD patients and controls, the cortical ones in particular.

5. Conclusions

Our data show there is an asymmetrical increase in the DTI parameters in patients with AD, which is consistent with our hypothesis stating that the same pattern may appear in other brain areas as well (which has not been proven yet). More specifically, a decrease in the volume of the left and the right putamen in the AD patients compared to controls was expected when measured by the FS. Interestingly, there was an increase in the NT in their proximity. If this was the effect of the compensatory changes (i.e., reduced volume of the structure and an increase in the amount of the WM fibers around it), then it remains unclear why the pallidum or caudate would not show a similar compensatory effect as well. Moreover, the timing of these changes remains unclear. Do they arrive prior to the decrease in the volume of the putamen and the increase in the white matter NT follows, or is it the other way around? Or rather, do all the changes occur relatively simultaneously?

Supplementary Materials: The following supporting information can be downloaded at: https://www.mdpi.com/article/10.3390/cells12091220/s1; Supplementary material contains nine example videos (AVI format) of DTI tractography and region of interest (ROI) delineation of caudate, pallidum, and putamen. Example video files: Video S1: Caudate AD; Video S2: Caudate ctrl; Video S3: Pallidum AD; Video S4: Pallidum ctrl; Video S5: Putamen AD; Video S6: Putamen ctrl; Video S7: R caudate ROI; Video S8: R pallidum ROI; Video S9: L putamen ROI. Table S1: The diffusion gradient table.

Author Contributions: Conceptualization, Z.W., A.L., P.Z. and N.O.; Data curation, A.B.; Formal analysis, B.B.K., I.I., J.T. and M.B.; Funding acquisition, P.Z.; Investigation, A.B.; Methodology, A.B.; Software, J.K., I.I. and J.T.; Supervision, P.Z. and J.M.; Visualization, V.M.; Writing—original draft, T.R. and P.Z.; Writing—review & editing, V.M. and J.M. All authors have read and agreed to the published version of the manuscript.

Funding: This research was funded by Charles University, grant numbers COOP 33, 36 and 38, and 260388/SVV/2023" and by the Ministry of Health of the Czech Republic, grant number NU20-04-00393, and conceptual development of research organization IKEM, IN 00023001, as well as partially by the long-term strategic development financing of the Institute of Computer Science, grant number RVO 67985807, and the European Regional Development Fund-Project, grant number CZ.02.1.01/0.0/0.0/16 019/0000766.

Institutional Review Board Statement: The study was conducted in accordance with the Declaration of Helsinki and approved by the Ethics Committee of the Prague Psychiatric Center/National Institute of Mental Health and the Human Ethics Committee of the Third Faculty of Medicine, Charles University, Prague, Czech Republic, (Protocol No. 2016/3) and informed consent was obtained from all the patients.

Informed Consent Statement: Informed consent was obtained from all the subjects involved in the study. Written informed consent was obtained from the patients to publish this paper.

Data Availability Statement: The data presented in this study are available on request from the corresponding author. The data are not publicly available due to ethical reasons.

Conflicts of Interest: The authors declare no conflict of interest.

Abbreviations

AD—Alzheimer's disease; APOE—apolipoprotein E; BFCS—basal forebrain cholinergic system; BG—basal ganglia; DTI—diffusion tensor imaging; DWI—diffusion-weighted imaging; FS—FreeSurfer; GFA—general fractional anisotropy; MMSE—mini-mental state examination test; MRI—magnetic resonance imaging; nQA—normalized quantitative anisotropy; NT—number of tracts; PD—Parkinson's disease; QA—quantitative anisotropy; QSDR—Q-space diffeomorphic reconstruction; SPECT—single photon emission computed tomography; TL—tract length; TV—tract volume; WM—white matter.

References

1. Cho, H.; Kim, J.H.; Kim, C.; Ye, B.S.; Kim, H.J.; Yoon, C.W.; Noh, Y.; Kim, G.H.; Kim, Y.J.; Kim, C.H.; et al. Shape changes of the basal ganglia and thalamus in Alzheimer's disease: A three-year longitudinal study. J. Alzheimer's Dis. **2014**, 40, 285–925. [CrossRef] [PubMed]
2. Ding, B.; Ling, H.W.; Zhang, Y.; Huang, J.; Zhang, H.; Wang, T.; Yan, F.H. Pattern of cerebral hyperperfusion in Alzheimer's disease and amnestic mild cognitive impairment using voxel-based analysis of 3D arterial spin-labeling imaging: Initial experience. Clin. Interv. Aging **2014**, 9, 493–500. [CrossRef] [PubMed]
3. Wright, S.; Kochunov, P.; Chiappelli, J.; McMahon, R.; Muellerklein, F.; Wijtenburg, S.A.; White, M.G.; Rowland, L.M.; Hong, L.E. Accelerated white matter aging in schizophrenia: Role of white matter blood perfusion. Neurobiol. Aging **2014**, 35, 2411–2418. [CrossRef]
4. Wen, W.; Sachdev, P.; Shnier, R.; Brodaty, H. Effect of white matter hyperintensities on cortical cerebral blood volume using perfusion MRI. Neuroimage **2004**, 21, 1350–1356. [CrossRef] [PubMed]
5. Kim, S.M.; Kim, M.J.; Rhee, H.Y.; Ryu, C.W.; Kim, E.J.; Petersen, E.T.; Jahng, G.H. Regional cerebral perfusion in patients with Alzheimer's disease and mild cognitive impairment: Effect of APOE epsilon4 allele. Neuroradiology **2013**, 55, 25–34. [CrossRef]
6. Andica, C.; Kamagata, K.; Hatano, T.; Saito, Y.; Ogaki, K.; Hattori, N.; Aoki, S. MR biomarkers of degenerative brain disorders derived from diffusion imaging. J. Magn. Reson. Imaging **2020**, 52, 1620–1636. [CrossRef]
7. Kuchtova, B.; Wurst, Z.; Mrzilkova, J.; Ibrahim, I.; Tintera, J.; Bartos, A.; Musil, V.; Kieslich, K.; Zach, P. Compensatory Shift of Subcallosal Area and Paraterminal Gyrus White Matter Parameters on DTI in Patients with Alzheimer Disease. Curr. Alzheimer Res. **2018**, 15, 590–599. [CrossRef]
8. McKhann, G.M.; Knopman, D.S.; Chertkow, H.; Hyman, B.T.; Jack, C.R., Jr.; Kawas, C.H.; Klunk, W.E.; Koroshetz, W.J.; Manly, J.J.; Mayeux, R.; et al. The diagnosis of dementia due to Alzheimer's disease: Recommendations from the National Institute on Aging-Alzheimer's Association workgroups on diagnostic guidelines for Alzheimer's disease. Alzheimer's Dement. **2011**, 7, 263–269. [CrossRef]
9. Albert, M.S.; DeKosky, S.T.; Dickson, D.; Dubois, B.; Feldman, H.H.; Fox, N.C.; Gamst, A.; Holtzman, D.M.; Jagust, W.J.; Petersen, R.C.; et al. The diagnosis of mild cognitive impairment due to Alzheimer's disease: Recommendations from the National Institute on Aging-Alzheimer's Association workgroups on diagnostic guidelines for Alzheimer's disease. Alzheimer's Dement. **2011**, 7, 270–279. [CrossRef]
10. Grothe, M.J.; Barthel, H.; Sepulcre, J.; Dyrba, M.; Sabri, O.; Teipel, S.J. In vivo staging of regional amyloid deposition. Neurology **2017**, 89, 2031–2038. [CrossRef]
11. Bartos, A.; Raisova, M. The Mini-Mental State Examination: Czech Norms and Cutoffs for Mild Dementia and Mild Cognitive Impairment due to Alzheimer's Disease. Dement. Geriatr. Cogn. Disord. **2016**, 42, 50–57. [CrossRef]
12. Andersson, J.L.R.; Sotiropoulos, S.N. An integrated approach to correction for off-resonance effects and subject movement in diffusion MR imaging. Neuroimage **2016**, 125, 1063–1078. [CrossRef] [PubMed]
13. Jenkinson, M.; Bannister, P.; Brady, M.; Smith, S. Improved optimization for the robust and accurate linear registration and motion correction of brain images. Neuroimage **2002**, 17, 825–841. [CrossRef] [PubMed]

14. Yeh, F.C.; Tseng, W.Y. NTU-90: A high angular resolution brain atlas constructed by q-space diffeomorphic reconstruction. Neuroimage **2011**, 58, 91–99. [CrossRef] [PubMed]
15. Fischl, B.; Salat, D.H.; Busa, E.; Albert, M.; Dieterich, M.; Haselgrove, C.; van der Kouwe, A.; Killiany, R.; Kennedy, D.; Klaveness, S.; et al. Whole brain segmentation: Automated labeling of neuroanatomical structures in the human brain. Neuron **2002**, 33, 341– 355. [CrossRef] [PubMed]
16. RC Team. A Language and Environment for Statistical Computing. Available online: https://www.R-project.org/ (accessed on 6 March 2023).
17. Fisher, R.A. Frequency Distribution of the Values of the Correlation Coefficient in Samples from an Indefinitely Large Population. Biometrika **1915**, 10, 507–521. [CrossRef]
18. Jones, D.K.; Cercignani, M. Twenty-five Pitfalls in the Analysis of Diffusion MRI Data. NMR Biomed. **2010**, 23, 803–820. [CrossRef] [PubMed]
19. Borkowski, K.; Klodowski, K.; Figiel, H.; Krzyzak, A.T. A theoretical validation of the B-matrix spatial distribution approach to diffusion tensor imaging. Magn. Reson. Imaging **2017**, 36, 1–6. [CrossRef]
20. Borkowski, K.; Krzyżak, A.T. Analysis and correction of errors in DTI-based tractography due to diffusion gradient inhomogeneity. J. Magn. Reson. **2018**, 296, 5–11. [CrossRef]
21. Yeh, F.C.; Verstynen, T.D.; Wang, Y.; Fernandez-Miranda, J.C.; Tseng, W.Y. Deterministic diffusion fiber tracking improved by quantitative anisotropy. PLoS ONE **2013**, 8, e80713. [CrossRef]
22. Zhang, H.; Wang, Y.; Lu, T.; Qiu, B.; Tang, Y.; Ou, S.; Tie, X.; Sun, C.; Xu, K. Differences between generalized q-sampling imaging and diffusion tensor imaging in the preoperative visualization of the nerve fiber tracts within peritumoral edema in brain. Neurosurgery **2013**, 73, 1044–1053. [CrossRef]
23. Tucholka, A.; Grau-Rivera, O.; Falcon, C.; Rami, L.; Sanchez-Valle, R.; Llado, A.; Gispert, J.D.; Molinuevo, J.L. Structural Connectivity Alterations Along the Alzheimer's Disease Continuum: Reproducibility Across Two Independent Samples and Correlation with Cerebrospinal Fluid Amyloid-beta and Tau. J. Alzheimer's Dis. **2018**, 61, 1575–1587. [CrossRef] [PubMed]
24. DeLong, M.R.; Wichmann, T. Circuits and circuit disorders of the basal ganglia. Arch. Neurol. **2007**, 64, 20–24. [CrossRef]
25. Grillner, S.; Robertson, B. The Basal Ganglia Over 500 Million Years. Curr. Biol. **2016**, 26, R1088–R1100. [CrossRef]
26. Pasquini, J.; Durcan, R.; Wiblin, L.; Gersel Stokholm, M.; Rochester, L.; Brooks, D.J.; Burn, D.; Pavese, N. Clinical implications of early caudate dysfunction in Parkinson's disease. J. Neurol. Neurosurg. Psychiatry **2019**, 90, 1098–1104. [CrossRef]
27. Sanjari Moghaddam, H.; Dolatshahi, M.; Mohebi, F.; Aarabi, M.H. Structural white matter alterations as compensatory mechanisms in Parkinson's disease: A systematic review of diffusion tensor imaging studies. J. Neurosci. Res. **2020**, 98, 1398–1416. [CrossRef] [PubMed]
28. Jackson, S.R.; Parkinson, A.; Jung, J.; Ryan, S.E.; Morgan, P.S.; Hollis, C.; Jackson, G.M. Compensatory neural reorganization in Tourette syndrome. Curr. Biol. **2011**, 21, 580–585. [CrossRef]
29. Ji, E.; Guevara, P.; Guevara, M.; Grigis, A.; Labra, N.; Sarrazin, S.; Hamdani, N.; Bellivier, F.; Delavest, M.; Leboyer, M.; et al. Increased and Decreased Superficial White Matter Structural Connectivity in Schizophrenia and Bipolar Disorder. Schizophr. Bull. **2019**, 45, 1367–1378. [CrossRef] [PubMed]
30. Xekardaki, A.; Giannakopoulos, P.; Haller, S. White Matter Changes in Bipolar Disorder, Alzheimer Disease, and Mild Cognitive Impairment: New Insights from DTI. J. Aging Res. **2011**, 2011, 286564. [CrossRef]
31. Wright, N.; Alhindi, A.; Millikin, C.; Modirrousta, M.; Udow, S.; Borys, A.; Anang, J.; Hobson, D.E.; Ko, J.H. Elevated caudate connectivity in cognitively normal Parkinson's disease patients. Sci. Rep. **2020**, 10, 17978. [CrossRef]
32. Deeb, W.; Salvato, B.; Almeida, L.; Foote, K.D.; Amaral, R.; Germann, J.; Rosenberg, P.B.; Tang-Wai, D.F.; Wolk, D.A.; Burke, A.D.; et al. Fornix-Region Deep Brain Stimulation-Induced Memory Flashbacks in Alzheimer's Disease. N. Engl. J. Med. **2019**, 381, 783– 785. [CrossRef] [PubMed]
33. Kilimann, I.; Grothe, M.; Heinsen, H.; Alho, E.J.; Grinberg, L.; Amaro, E., Jr.; Dos Santos, G.A.; da Silva, R.E.; Mitchell, A.J.; Frisoni, G.B.; et al. Subregional basal forebrain atrophy in Alzheimer's disease: A multicenter study. J. Alzheimer's Dis. **2014**, 40, 687–700. [CrossRef] [PubMed]

10.1 Attachement no. 4

Co-author

4. GAŠPAR, Branislav; MRZÍLKOVÁ, Jana; HOZMAN, Jiří; ZACH, Petr; **LAHUTSINA, Anastasiya**; MOROZOVA, Alexandra; GUARNIERI, Giulia; RIEDLOVÁ, Jitka. Micro-Computed Tomography Soft Tissue Biological Specimens Image Data Visualization. *Applied Sciences*. 2022, **12**(10), 4918. ISSN 2076-3417. DOI: 10.3390/app12104918.

IF: 2.838/2021 (Q2/2021)

applied sciences

MDPI

Article

Micro-Computed Tomography Soft Tissue Biological Specimens Image Data Visualization

Branislav Gaspar [1], Jana Mrzilkova [2], Jiri Hozman [1], Petr Zach [2,*], Anastasiya Lahutsina [2], Alexandra Morozova [2], Giulia Guarnieri [3] and Jitka Riedlova [2]

[1] Department of Biomedical Technology, Faculty of Biomedical Engineering, Czech Technical University in Prague, Nam. Sitna 3105, 272 01 Kladno, Czech Republic; gaspabra@student.cvut.cz (B.G.); hozman@fbmi.cvut.cz (J.H.)

[2] Department of Anatomy, Third Faculty of Medicine, Charles University, Ruska 87, 100 00 Prague, Czech Republic; mrzilkova.jana@seznam.cz (J.M.); anastasiya.lahutsina@lf3.cuni.cz (A.L.); alexandra.morozova@lf3.cuni.cz (A.M.); jitka.riedlova@lf3.cuni.cz (J.R.)

[3] Department of Experimental and Clinical Medicine, Anatomy and Histology Section, University of Firenze, Largo Brambilla 3, 50134 Firenze, Italy; giulia.guarnieri@unifi.it

* Correspondence: zach.petr@post.cz

Abstract: Visualization of soft tissues in microCT scanning using X-rays is still a complicated matter. There is no simple tool or methodology on how to set up an optimal look-up-table while respecting the type of soft tissue. A partial solution may be the use of a contrast agent. However, this must be accompanied by an appropriate look-up-table setting that respects the relationship between the soft tissue type and the Hounsfield units. The main aim of the study is to determine experimentally derived look-up-tables and relevant values of the Hounsfield units based on the statistical correlation analysis. These values were obtained from the liver and kidneys of 24 mice in solutions of ethanol as the centroid value of the opacity look-up-table area under this graph. Samples and phantom were scanned by a Bruker SkyScan 1275 micro-CT and Phywe XR 4.0 and processed using CTvox and ORS Dragonfly software. To reconstruct the micro-CT projections, NRecon software was used. The main finding of the study is that there is a statistically significant relationship between the centroid of the area under the look-up-table curve and the number of days for which the animal sample was stored in an ethanol solution. H1 of the first hypothesis, i.e. that suggested the Spearman's correlation coefficient does not equal zero ($r_1 = 0$) regarding this relationship was confirmed. On the other hand, there is no statistically significant relationship between the centroid of the area under the look-up-table curve and the concentration of the ethanol solution. In this case, H1 of the second hypothesis, i.e. that the Spearman's correlation coefficient does not equal zero ($r_2 = 0$) regarding this relationship was not confirmed. Spearman's correlation coefficients were 0.27 for the concentration and 0.87 for the number of days stored in ethanol solution in the case of the livers of 13 mice and 0.06 for the concentration and 0.94 for the number of days stored in ethanol solution in the case of kidneys of 11 mice.

Keywords: micro-CT; transfer function; look-up-table; soft tissue; CT number; Hounsfield unit; visualization

Citation: Gaspar, B.; Mrzilkova, J.; Hozman, J.; Zach, P.; Lahutsina, A.; Morozova, A.; Guarnieri, G.; Riedlova, J. Micro-Computed Tomography Soft Tissue Biological Specimens Image Data Visualization. Appl. Sci. **2022**, 12, 4918. https://doi.org/10.3390/app12104918

Academic Editors: Cecilia Di Ruberto, Andrea Loddo, Lorenzo Putzu, Alessandro Stefano and Albert Comelli

Received: 25 February 2022
Accepted: 11 May 2022
Published: 12 May 2022

Publisher's Note: MDPI stays neutral with regard to jurisdictional claims in published maps and institutional affiliations.

1. Introduction

Computed tomography (CT) imaging is widely used in medical practice, mainly due to the non-invasiveness of this method, its good spatial resolution, and the relatively short acquisition time of the required images. In addition to conventional CT, which is mainly used both for diagnostic and therapeutic procedures [1], high spatial resolution CT or micro-CT (CT) are also used in practice [2]. These systems work on the same basic principle as the typical CT, except that the X-ray-tube-detector system does not perform rotational motion, but rotates the specimen. However, their advantage lies in their ability to scan samples with much higher spatial (<50 m) and contrast resolution.

ci

It is because of the non-destructiveness of this method in evaluating the scanned volume with high resolution that CT devices are much used in both research and industry. Furthermore, even if the intrinsic noise of commercial CT detectors is not a problem in many cases (especially in industry), the imaging of more delicate structures with a lower range of CT numbers (the same as Hounsfield units = HU), and the associated lower attenuation contrast between structures, such as soft tissues, is greatly hampered by this noise.

The present work, in collaboration with the Department of Anatomy at the 3rd Faculty of Medicine, Charles University (Prague, Czech Republic), is primarily focused on the visualization of soft tissues in particular, as well as the search for a methodology that could optimize the overall visualization process and make it easier. This also involves research and experimentation with new procedures and contrast agents to achieve the required contrast between soft tissues that is needed for visualization [3–7].

Two papers dealt with similar issues. The first one, i.e., [8], used an image histogram for optimal look-up-table (LUT) setup. Thus, it is not the same intention. The second work, i.e., [9], uses only the LUT settings. However, in neither case was it possible to find a link between soft tissue type and Hounsfield units.

We have been using CT for a long time and we need to visualize soft tissues in experimental animals. For a long time, there is a tradition of contrast agent usage, but they are not always best and/or we often encounter problems when using them. This is why we tried to figure out some connection between LUT setting and HU values for individual structures and organs; even mentioned contrast agents could have been of some value in this. Additionally, we wanted to find out if there exist other possibilities of contrast enhancement, e.g., because of air bubbles in contrast agent for ultrasound. Especially this is considered when experimenting with PHYWE XR 4.0 in various structures in chicken tissues (phantom). Finally, we also think about semiautomated, or fully automated settings of LUT with fuzzy logic. Some of these ideas were verified within this study.

The main aim of this study is to optimize soft tissue contrast visualization of biological specimens (mouse liver, kidneys) using a contrast agent and a proper LUT. Based on this aim we would like to statistically verify the relationship between the centroid of the area under the look-up-table curve and the number of days for which the animal sample was stored in the ethanol solution, as well as the concentration of the ethanol solution. Therefore, two hypotheses were formulated. H1 (Each occurrence of H1 means that it is an allernative hypothesis) of the first hypothesis states that the Spearman's correlation coefficient does not equal zero ($r_1 = 0$) in the case of relationship between the coordinates of the center of gravity (centroid) of the area under the LUT and the number of days for which the sample was stored in the ethanol solution. H1 of the second hypothesis states that the Spearman's correlation coefficient does not equal zero ($r_2 = 0$) in the case of relationship between the coordinates of the center of gravity (centroid) of the area under the LUT and the ethanol concentration in the solution.

2. Materials and Methods

2.1. Materials, Devices, and Software

The database of CT images from the Dept. of Anatomy of the 3rd Medical Faculty of Charles University was used for the study.

All intravenous contrast agent's applications follow similar pattern. At first there is introduced the contrast agent into the tail vein. After that follows animal euthanasia and CT scanning. Concerning Aurovist contrast agent, solution from the ampoule is injected into tail vein under isoflurane anesthesia into the bloodstream. Follows scanning in the CT apparatus. Concerning the timing, scanning is performed after complete distribution of Aurovist gold nanoparticles to the tissues of the animal, including both arteries and veins of the circulatory system.

Preparation steps for experimental animals were the following.

Animals (mice) were housed in the standard light/dark cycle in the First Faculty of Medicine, Charles University at standard room temperature. Mice were applied one ampulla of Aurovist contrast agent (15 nm of Aurum particles in 40 mg of solution, Nanoprobes, Yaphank, NY, USA) in the tail vein per one mouse. In case of whole mouse experiment, 2 h after Aurovist application were mice euthanized with pentobarbital and scanned in micro-CT. Timing was selected because rigor mortis develops within 2 h after death.

Animals (chickens) were obtained by micro-surgery from the eggs in their 19 days of development. Firstly, a rectangular window was dissected out of the egg wall and solution of 40% KI to euthanize chicken (heartbeat stop) was applied intra-amniotically. After the removal of dead chicken from the egg it was placed into 80% of Ethanol for 7 days.

Animals (rabbits) were donated by Prof. Berndt Minnich, University of Salzburg, Vascular Unit, Austria. Post-mortem, rabbits were pinned in supine position onto a wax plate. After opening of the abdomen, the aorta abdominalis was identified and separated from each other. A ligature around the aorta abdominalis ensured exclusive upper body casting. A tube was inserted into the artery cranially to the first ligature and tied in place (6.0 sutures). Blood vessels were rinsed after opening the aorta with 0.9% Ringer's solution (60 mL/h) at 37 C until clear reflux appeared. Thereafter, the casting medium (Mercox-Cl-2B, Ladd Research Inc., Burlington, VT, USA) diluted with monomeric methyl methacrylate was injected at 99 mL/h by an electric syringe pump (Habel PSA 50, Sky Electronics S.A., Grenoble, France) or a pneumatic injection pump (ComServ OG, Ebenau, Austria). When the injected resin became viscous, animals were left in place for at least 30 min at room temperature (RT) to initiate resin polymerization. The upper bodies of the rabbits were cut off and tempered in water (60 C, 24 h). Subsequently, water was replaced by potassium hydroxide (7.5%, 40 C, twice for 24 h), followed by hydrochloric acid (2%, RT, 24 h) and formic acid (5%, RT, 15 min). Finally, casts were washed thrice and frozen in distilled water (20 C) and freeze-dried (FreeZone 77520, Labconco Corp., Kansas City, MO, USA).

The database consisted of ex vivo chickens in and out of the shell and aged 5 to 19 days. Chickens outside the shell were preserved in 50–100% ethanol solution, some of them additionally in formaldehyde solution. In addition, a few chicken samples contained injected gold nanoparticles from the Aurovist contrast agent. Prior to acquisition, samples were left in air after removal from the solution and scanned with Bruker's SkyScan 1275 (Bruker MicroCT, Kontich, Belgium) after evaporation of the solution.

Another part of the database consisted of ex vivo preparations of mice injected with Aurovist contrast agent containing 15 nm gold nanoparticles (AuNPs) prior to scanning.

A 50% solution of Omnipaque contrast agent was then used intravenously before scanning the mouse organs themselves (liver, lungs, spleen, and heart).

Some mouse organs, such as liver, kidney, brain, heart, and leg, were kept for one week in a solution of potassium iodide with concentration 100 mM (KI, Merck, Czech Republic) in 20% ethanol before scanning.

Lastly, the database included corrosive preparations in which a resin (Mercox) [10] was infused into the vascular system and allowed to harden, the remaining tissue was then dissolved in lye by maceration and the sample was scanned. Corrosive preparations of rabbit and rat lung and heart were selected for the purpose of this study.

For the implementation of the idea of blood vessels visualization in soft tissue using the contrast that would be created by the presence of air in the vascular cavities, chicken flesh was used as a phantom in which cylindrical tubes/capillaries of various diameters made of different materials were placed. These were two tubes (silicone), a glass capillary with sealed ends, and a plastic straw (bioplastic PLA). This phantom, depicted in Figure 1, was then scanned with the Phywe XR 4.0 (PHYWE Systeme GmbH & Co. KG, Göttingen, Germany) experimental setup.

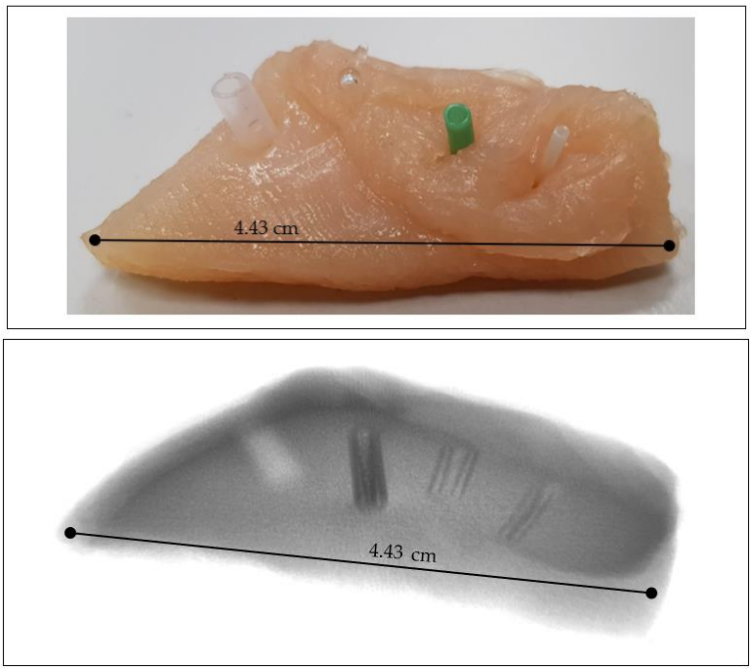

Figure 1. Chicken sample with capillaries as vascular phantom (**top**) and phantom X-ray image (**bottom**); materials from left: bioplastic PLA, glass, green silicone, and transparent silicone. Scale is in [cm].

Two CT systems were used to scan the above samples. The ex vivo chicken samples were scanned with a professional CT system Bruker SkyScan 1275 located at the Department of Anatomy, 3rd Faculty of Medicine, Charles University, while the Phywe XR 4.0 experimental setup was used to scan the phantom of the chicken vasculature and capillaries at the Dept. of Biomedical Technology, Fac. of Biomedical Engineering, Czech Technical University in Prague.

Bruker's SkyScan 1275 has been specifically designed for fast scanning using advances in X-ray source technology and efficient flat-panel detectors. This X-ray source has the selectable anode voltage of the assembly ranging from 20 to 100 kV and the max. available power is 10 W. The assembly includes an active 3 megapixel CMOS flat-panel detector with a maximum possible resolution of up to 4 m (at maximum magnification) and it is capable of accommodating a sample diameter of 96 mm and a height of 120 mm. All used setups of the above mentioned CT are available within the Appendix B, i.e., Tables A2–A19.

The XR 4.0 experimental setup from the German company Phywe was designed for teaching purposes and for laboratory experiments with X-rays. Its advantage lies, among other things, in the relatively easy and quick interchangeability of the X-ray tube and, therefore, facilitates experiments with different anode materials [11,12].

The XR 4.0 can also be used as a CT system thanks to an expansion kit supporting the computed tomography function. This set consists of a fixed copper X-ray tube that illuminates the specimen on a rotary table driven by a stepper motor with a minimum adjustable table rotation angle of 0.086. The attenuated X-ray radiation is then incident on an XRIS detector (CMOS) with an active area of 5 5 cm^2 and a maximum possible resolution of 48 m [11,12]. The selectable anode voltage of the assembly is 5–35 kV with an adjustable emission current in the range up to 1 mA. Setup with detailed setting is available within the Appendix B, i.e., Table A1.

As regards the software, CTvox (Version 3.3.1, 3D.SUITE Software, Bruker MicroCT, Kontich, Belgium) [13] and ORS Dragonfly (Version 2020.2 Build 941, Montreal, QC, Canada) [14] software were used for suitable visualization. Within an additional part of the study there were used NRecon (Version 1.7.4.2, Bruker MicroCT, Kontich, Belgium) [15] and Measure CT (Version 2.0, PHYWE Systeme GmbH & Co. KG, Göttingen, Germany) [12]

software to reconstruct the CT projections. Software MIPS (Version 2.0, Czech Technical University in Prargue, Faculty of Biomedical Engineering, Kladno, Czech Republic) [16] was used for illustration purposes only.

2.2. Methods

In the field of digital image data processing (digital images), various point operators or functions are very often used to perform single-point assignment, or transform the value of an image point (pixel) from an input image (labeled a) at a given position (x, y) to another value within the output image (labeled b), but at the same position (x, y). In general, this situation is indicated in Figure 2.

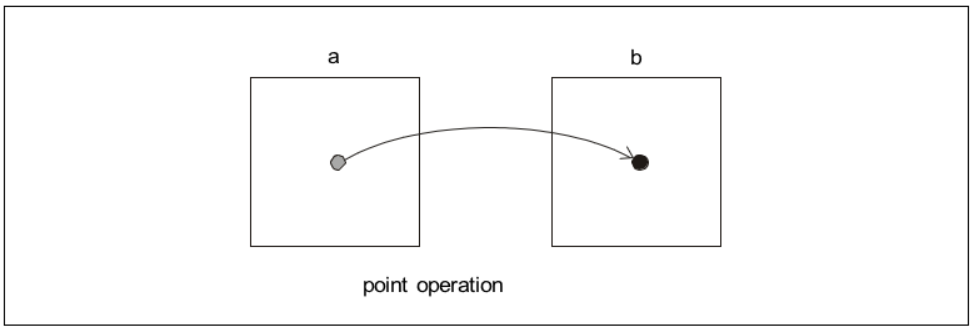

Figure 2. Diagram of general principle of the point operator (function)—the output of which is an unambiguous assignment of the value of a pixel in the output image. It is related to the value of a pixel in the input image.

2.2.1. Transfer Functions, Resp. Look-up-Table Concept

Let us consider an experiment where we multiply the pixel values in the input image by 1. If we consider the usual input dynamic range of grayscale digital images (i.e., 0 to 255, where 0 represents the black level and 255 represents the white level), then the output image will produce a result that is identical to the values in the input image. For example, an input value of 10 would be multiplied by 1 and the result would also be 10 and this would continue for all pixel values in all positions. This then results in a simple linear function that can be represented as a straight line at a 45 angle and passing through the origin of the coordinates, or it is a simple copy of the input image. Such an example can also be expressed very simply in mathematical notation, namely the slope equation of the straight line as reported in Figure 3.

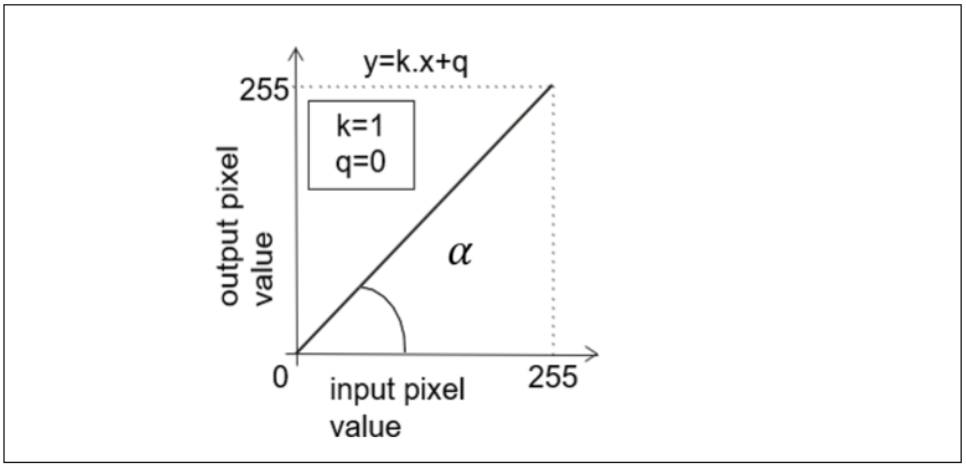

Figure 3. Example of a point operator (function) that implements a copy of the input image on the output. In this case, the value of the slope (i.e., k = 1), and the value of the y-intercept of a straight line where a line crosses y-axis of a graph (i.e., q = 0).

With this defined operator, we can easily adjust various changes to image parameters such as brightness and contrast, both when we need to highlight selected gray levels or when we need to suppress them. Examples of different transfer functions are shown in Figures 4 and 5.

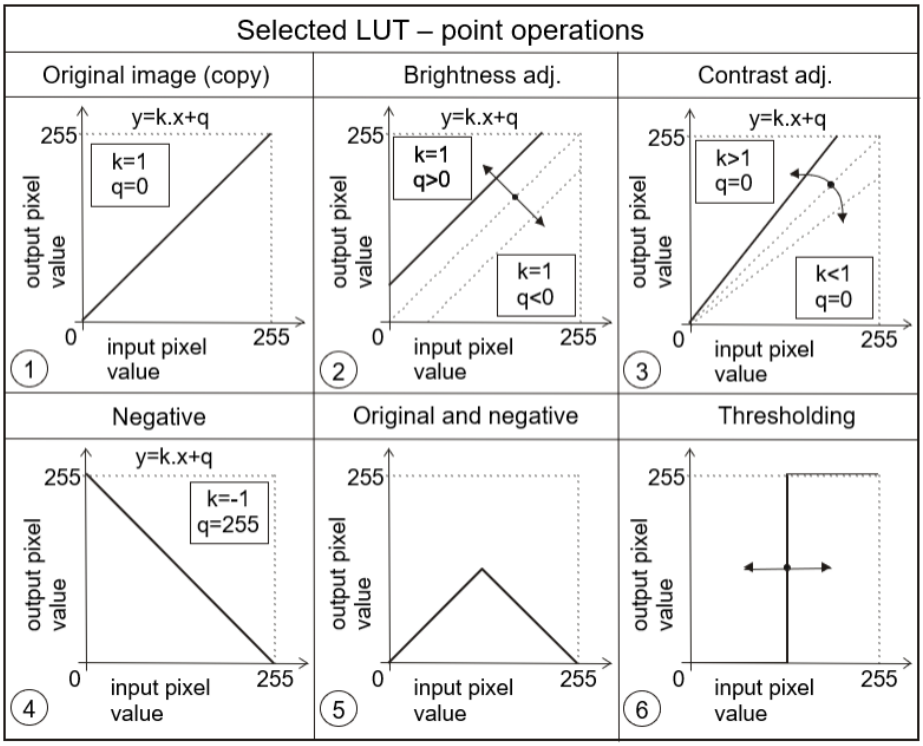

Figure 4. Examples of different point operators (functions) being very often used.

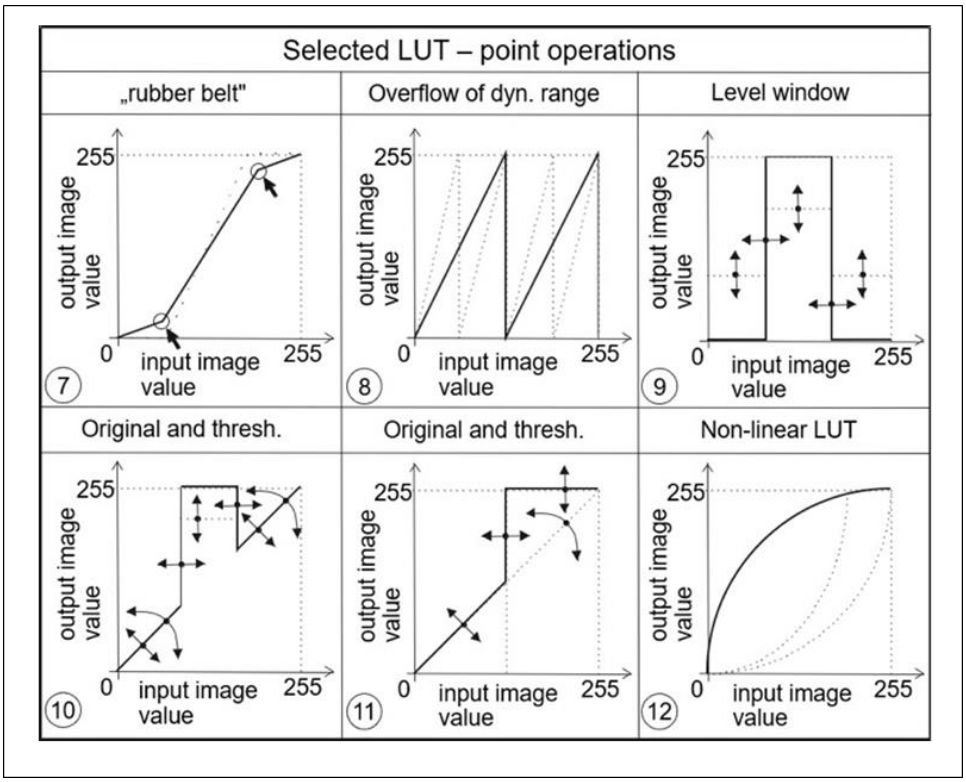

Figure 5. Examples of other point operators (functions) that could also be utilized.

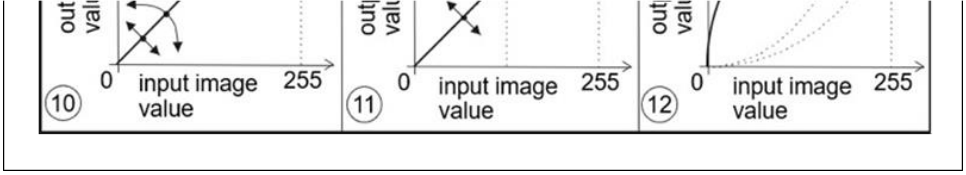

From the above examples, it is clear that these transfer functions or LUTs allow to significantly influence the visualization process of the given image data. Thus, for example, the transfer function in Figure 4 (panel 2) affects the brightness of the image, in Figure 4 (panel 3) it affects the contrast, in Figure 4 (panel 6) a transfer function for realizing a so-called binary image (i.e., an image that contains only two levels, most often black and white) is shown, and yet another suitable example can be seen in Figure 5 (panel 12), which is suitable for correcting an image that was taken under greatly reduced or increased lighting conditions. The latter two examples are further illustrated in the image data, respectively, in Figures 6 and 7.

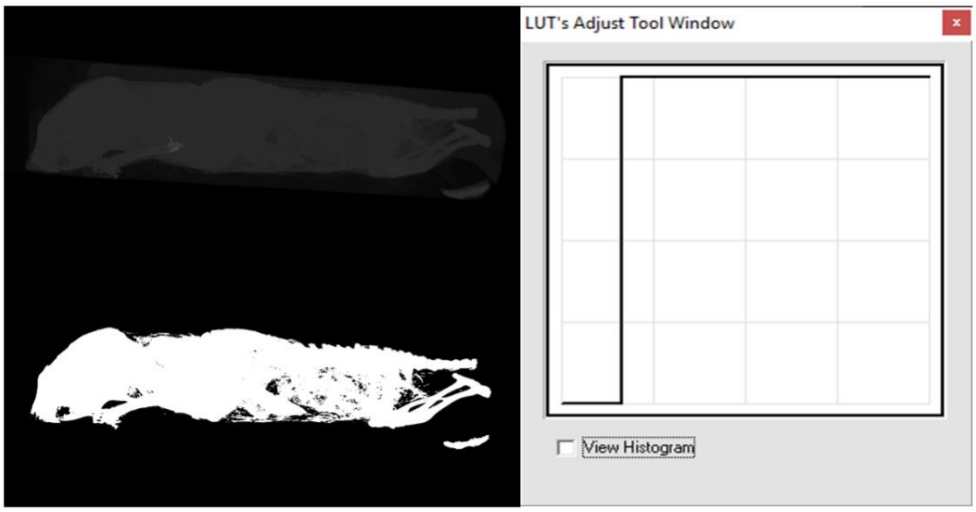

Figure 6. Example of a point operator (function)—thresholding or binarization [16].

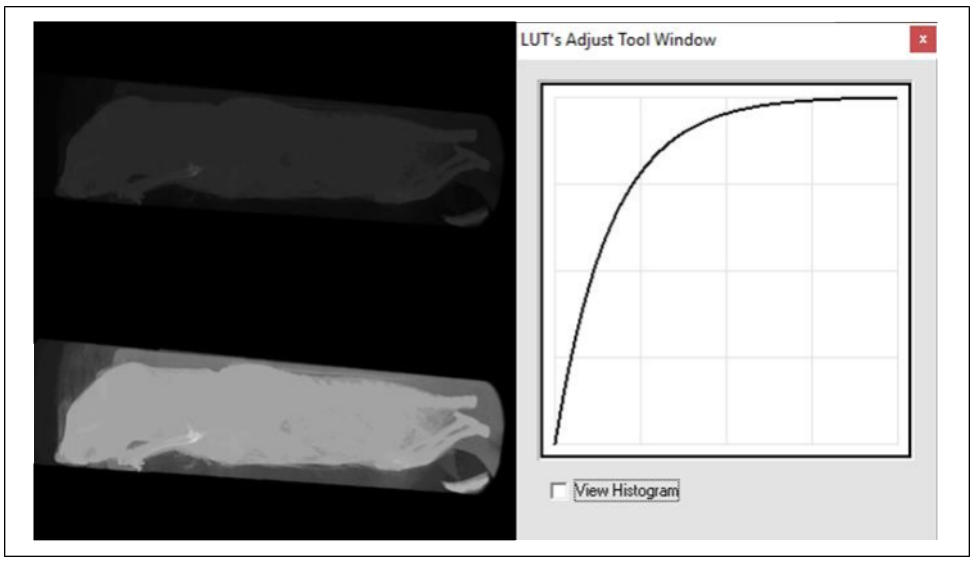

Figure 7. Examples of point operator (function)—logarithmic function [16].

2.2.2. Transfer Functions Related to the Hounsfield Units (HU)

There is a very important process in CT and CT imaging, that is the actual conversion of the attenuation of the passing X-rays to the grey level. Based on the physiological properties of human vision, 256 gray levels are very often used. The range of so-called Hounsfield units (HU) is typically in the range 1024 to +3071, which is 4096 values, and this is a much larger dynamic range than the 256 gray level values. For this reason, only the so-called windows on a given tissue (limited HU range), which has a width of 256 values or greater, need to be displayed. Thus, it is never possible to see all tissues at once, see

soft tissue window, bone window, etc. Realistically, this situation is often implemented by a transfer function that has HU values on the x-axis and gray level values from 0 to 255 on the vertical axis. The situation is also depicted in Figure 8, which is an example of this situation in NRecon software [15].

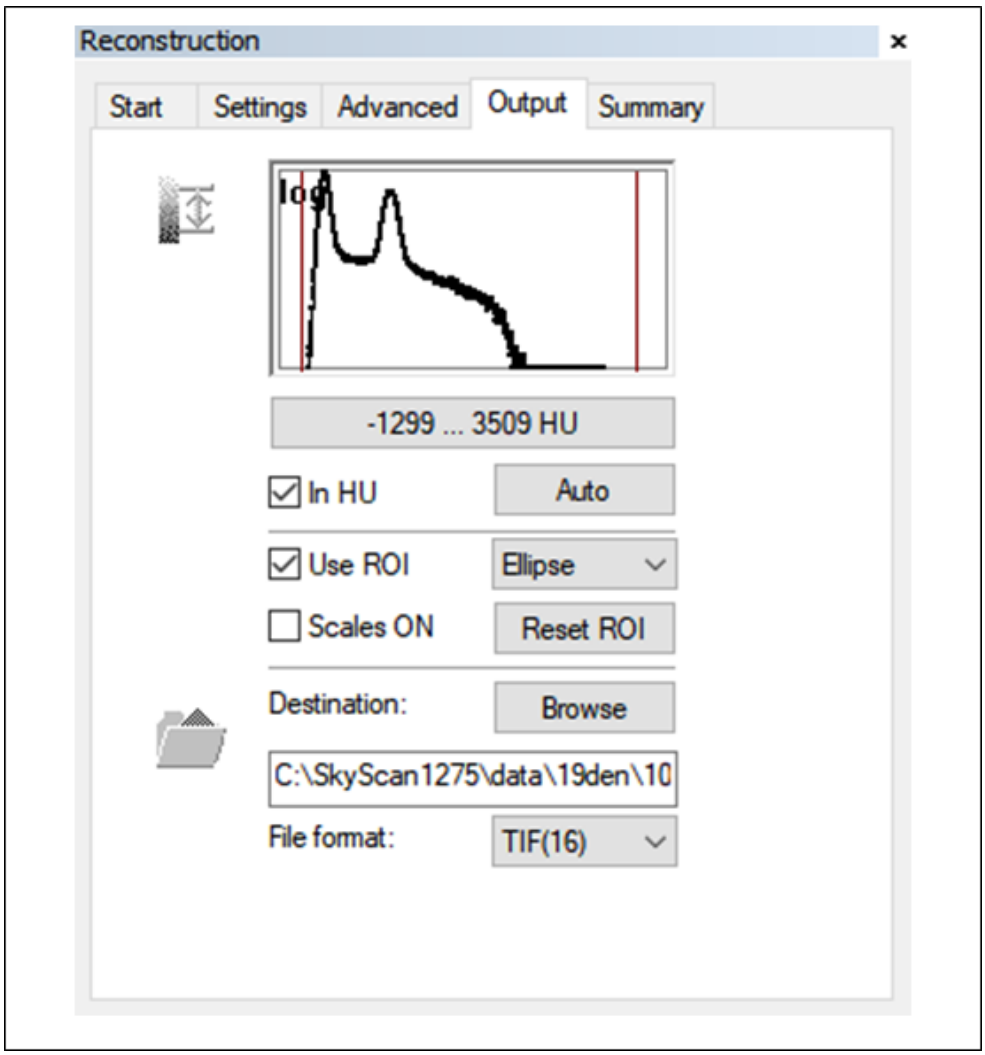

Figure 8. Nrecon SW MENU detail—reconstruction of outputs (parameter settings).

The practical impact of this situation is also the arrangement of the image data format in the form of so-called DICOM (Digital Imaging and Communications in Medicine) files. This file contains both image data and metadata [17] and each DICOM browser can display both. The structure of DICOM files consists of so-called tags and an example of these tags in relation to HU are the following items (i.e., the DICOM attribute number (0028,1053) whose name is "Rescale slope" and the DICOM attribute number (0028,1052) whose name is "Rescale intercept"). These parameters can then be substituted into the equation after the parameters k and q in Figure 3. These items can also be read.

2.2.3. Transfer Functions Design Possibilities

Within the Ctvox software a histogram of the attenuation is available together with an editor that can be used to freely modify the transfer functions as LUTs, i.e., the program can either simply connect individual markers or use them as nodes to create a so-called spline curve. The program then assigns to each voxel the corresponding degree of the currently selected parameter (the so-called emission color [18]) depending on the attenuation of the voxel in the spline mode called volume rendering.

There are five parameters to choose from—opacity, red (R) channel, green (G) channel, blue (B) channel, and luminance (L), as reported in Figure 9c. If all three RGB channels are combined, only two parameters are available (i.e., opacity and luminance), and the voxels are assigned to their opacity and grayscale. In the other case, four parameters are available, namely, opacity together with all three RGB channels. In addition to assigning opacities, individual voxels can also be colored differently in this way, or segmented by color. In the case of opacity, there is available a purple opacity curve (initially a straight line, with just two markers) appears, in order to indicate that it is active. Opacity is the opposite of transparency. Hence, we will need to map low intensities to low opacities (i.e., high transparency), as shown in Figure 9c.

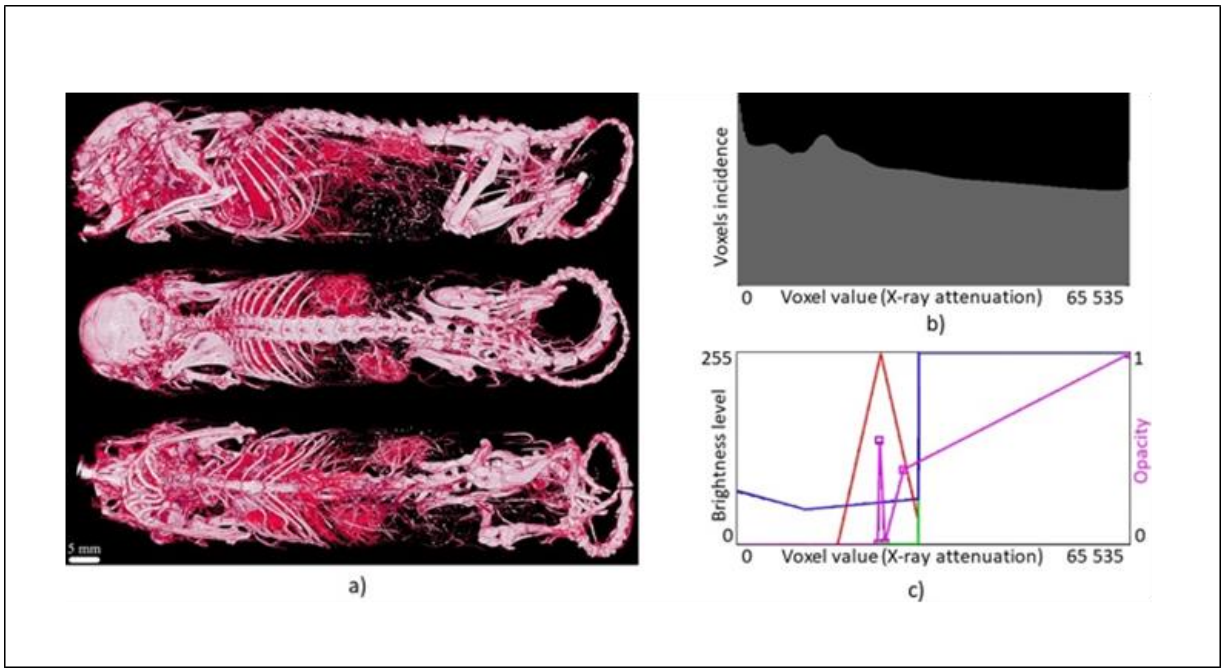

Figure 9. Transfer functions design—(**a**) mouse (Aurovist, 42 kV), (**b**) histogram, and (**c**) transfer functions (opacity, RGB).

3. Results

A total of 53 transfer functions (LUTs) were designed, 42 of which were validated and optimized to emphasize the soft tissues of selected biological samples from CT (mouse, rat, rabbit) using selected contrast agents (Aurovist, Omnipaque, KI in the ethanol solution, Mercox). The remaining 11 transfer functions could not be verified due to the absence of contrast in soft tissue samples from chickens. In total, 18 images and transfer functions are included within this text.

Out of the 53 transfer functions, one transfer function was able to be suggested that would likely highlight the tongue of a 19-day-old chick scanned with the Bruker SkyScan 1275 [19] at an anode voltage of 40 kV.

A total of 24 mice samples were statistically processed via correlation. Normality test was performed for all these samples in Matlab (Campus Wide Matlab, R2021a, The MathWorks, Inc., Natick, MA, USA) via Lilliefors test. These values were obtained for liver and kidneys of 24 mice in solutions of ethanol as a centroid value of the opacity LUT area under this graph (see example on Figure 10). Except for one dataset, all the others do not have a normal distribution according to this test. Results are available within Tables 1–4 below. From this follows that there is required to use Spearman·s correlation coefficient.

In Figure 10, we can see example of the opacity LUT with marked points, i.e., [X1,Y1], [X2,Y2], and [X3,Y3] whereby coordinate Y1 = 0 and Y3 = 0. These points form a homogenous triangle that enables simplified computation of the centroid.

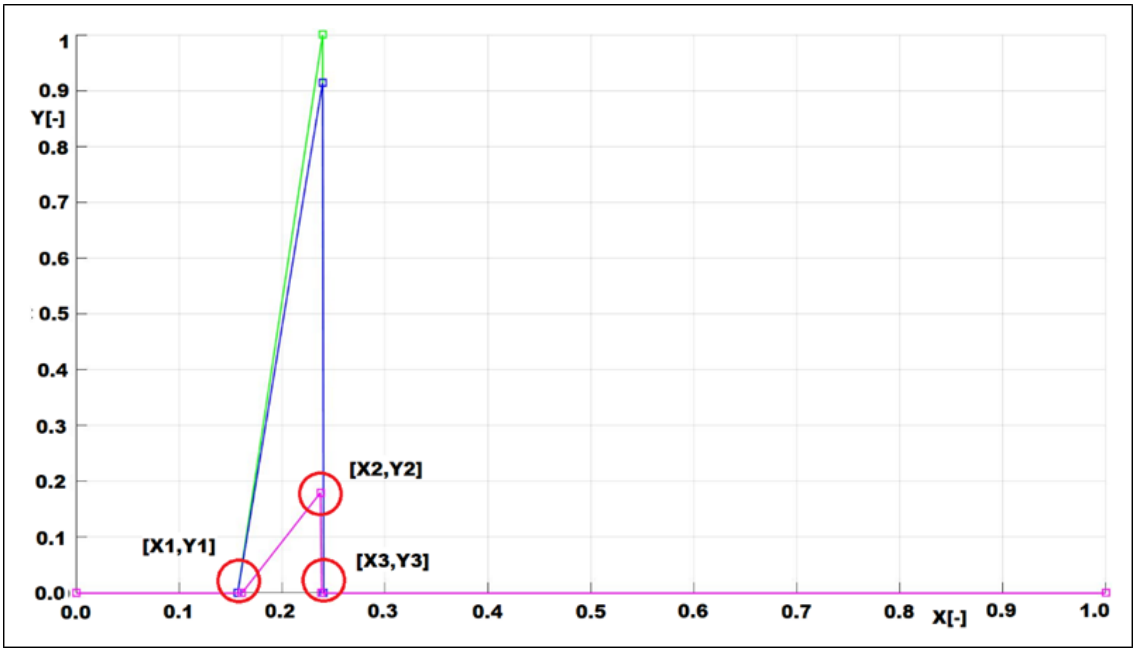

Figure 10. Example of the opacity (pink color) LUT with marked points that are used for computation of the centroid. Such figure exists for every included image (mouse_1_liver_ethanol_100_%_day_16).

Table 1. p-values of the Lilliefors test of normality.

Parameter	Value p-Value	Note
X^0—x coordinate of centroid [1]	0.2605	liver
Ethanol solution concentration [%]	0.0010	liver
X'—Storage time of the sample in Ethanol solution [days]	0.0010	liver
X^0—x coordinate of centroid [1]	0.0223	kidneys
Ethanol solution concentration [%]	0.0010	kidneys
Storage time of the sample in Ethanol solution [days]	0.0055	kidneys

[1] Centroid was computed according to the formula available on the link within [29]. In case of a homogenous triangle, the resulting centroid's x coordinate is the average of the x coordinates of its vertices.

Table 2. Ethanol concentrations and Spearman correlation coefficients computation.

Solution and Soft Tissue	Value X1 [1] [-]	Value X2 [2] [-]	Value Y2 [3] [-]	Value X3 [4] [-]	Value X^0 [5] [-]	Value c [6] [%]	Value d [7] [Days]
Ethanol, liver	0.2461	0.4303	0.1898	0.4320	0.3695	50	8
Ethanol, liver	0.1200	0.1994	0.1551	0.2004	0.1733	50	17
Ethanol, liver	0.1476	0.2230	0.1343	0.2241	0.1982	50	17
Ethanol, liver	0.1329	0.1827	0.1828	0.1838	0.1665	50	17
Ethanol, liver	0.2410	0.3718	0.2465	0.3735	0.3288	100	8
Ethanol, liver	0.1610	0.2374	0.1801	0.2385	0.2123	100	16
Ethanol, liver	0.2771	0.4010	0.4626	0.4028	0.3603	100	8
Ethanol, liver	0.1103	0.1467	0.2474	0.1900	0.1492	100	16
Ethanol, liver	0.1994	0.2048	0.3019	0.2099	0.2358	100	8
Ethanol, liver	0.1153	0.1687	0.2756	0.1704	0.1515	100	16
Ethanol, liver	0.0978	0.0989	0.1842	0.1378	0.1115	100	37

Table 2. Cont.

Solution and Soft Tissue	Value X1 [1] [-]	Value X2 [2] [-]	Value Y2 [3] [-]	Value X3 [4] [-]	Value X^0 [5] [-]	Value c [6] [%]	Value d [7] [Days]
Ethanol, liver	0.0836	0.1213	0.1607	0.1519	0.1189	100	37
Ethanol, liver	0.0707	0.1425	0.1233	0.1437	0.1190	100	37

[1] X1—horizontal coordinate of the homogenous triangle (Y1 = 0); [2] X2—horizontal coordinate of the homogenous triangle; [3] Y2—vertical coordinate of the homogenous triangle; [4] X3—horizontal coordinate of the homogenous triangle (Y3 = 0); [5] X·—horizontal coordinate of centroid; [6] c—Ethanol solution concentration; [7] d—storage time of the sample in Ethanol solution.

Table 3. Ethanol kidney raw data for centroid and Spearman·s correlation coefficient computation.

Solution and Soft Tissue	Value X1 [1] [-]	Value X2 [2] [-]	Value Y2 [3] [-]	Value X3 [4] [-]	Value X^0 [5] [-]	Value c [6] [%]	Value d [7] [Days]
Ethanol, kidneys	0.1279	0.1478	0.2493	0.1814	0.1524	50	16
Ethanol, kidneys	0.1170	0.1515	0.1565	0.1532	0.1406	50	7 50
Ethanol, kidneys	0.1112	0.1753	0.1247	0.1762	0.1542		16
Ethanol, kidneys	0.1188	0.1411	0.1385	0.1429	0.1343	100	7
Ethanol, kidneys	0.1055	0.1739	0.1925	0.1747	0.1514	100	16
Ethanol, kidneys	0.1170	0.1463	0.2091	0.1480	0.1371	100	7
Ethanol, kidneys	0.1117	0.2443	0.2452	0.2455	0.2005	100	16
Ethanol, kidneys	0.0669	0.0932	0.0997	0.0939	0.0847	100	7
Ethanol, kidneys	0.1849	0.2733	0.0693	0.2744	0.2442	100	37
Ethanol, kidneys	0.1979	0.2379	0.0568	0.3286	0.2548	100	37
Ethanol, kidneys	0.2002	0.2792	0.1981	0.3239	0.2678	100	37

[1] X1—horizontal coordinate of the homogenous triangle (Y1 = 0); [2] X2—horizontal coordinate of the homogenous triangle; [3] Y2—vertical coordinate of the homogenous triangle; [4] X3—horizontal coordinate of the homogenous triangle (Y3 = 0); [5] X^0—horizontal coordinate of centroid; [6] c—Ethanol solution concentration; [7] d—storage time of the sample in Ethanol solution.

Table 4. Related parameters computed from raw data.

Parameter	Value 7D	Value 8D	Value 16/17D	Value 37D	Note
N day avg centroid x coord.	0.1242	N A	0.1646	0.2556	Ethanol, kidneys
CT number [1]	379.25	N A	176.92	277.94	Ethanol, kidneys
N day avg centroid x coord.	NA	0.3236	0.1752	0.1165	Ethanol, liver
CT number [1]	NA	617.92	124.22	417.67	Ethanol, liver

[1] CT_number = 5000 N_day_{avg}—1000.

The hypotheses mentioned within the Introduction were evaluated based on these data. This was a test of the alternative hypothesis that the Spearman correlation coefficient is not equal to 0. We used a relationship (see link within the [21]) where, given H0: r = 0, the t Student's statistic has a distribution with d.f. (degree of freedom): N—2 (see also link within the [22]).

Ethanol liver: D.f.: 11, p-value: 0.3774 (for ethanol concentration) and D.f.: 11, p-value: 0.0001 (for days stored of the sample in ethanol solution).

Ethanol kidneys: D.f.: 9, p-value: 0.8504 (for ethanol concentration) and D.f.: 9, p-value: 0.00001 (for days stored of the sample in ethanol solution).

Overall, 18 LUTs from 53 LUTs were also validated on selected biological samples, selection of which is illustrated within this section and reported in Figures 9 and 11–13.

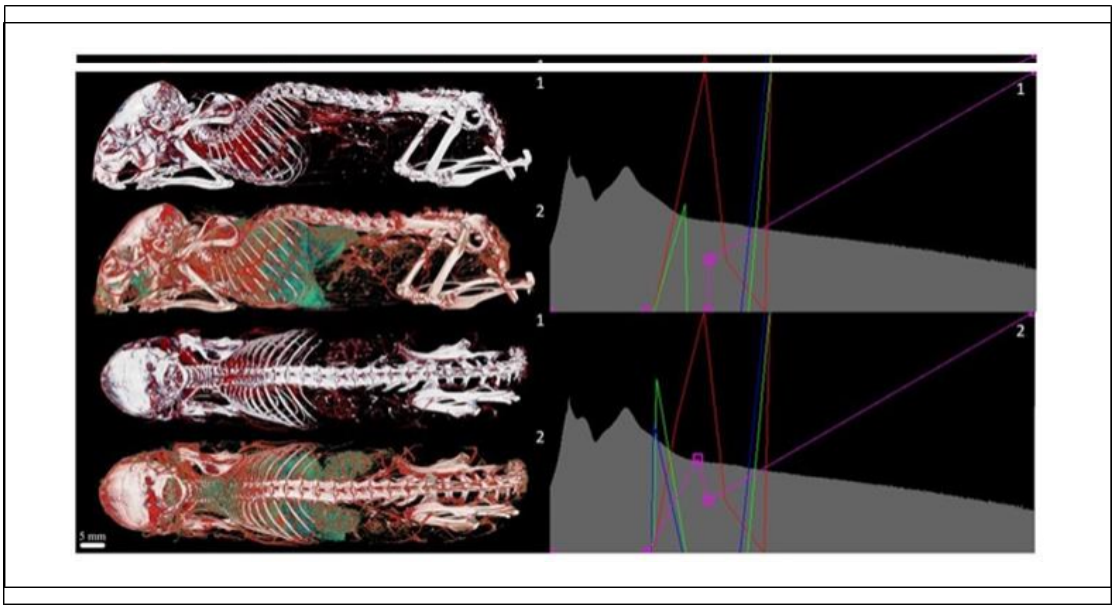

Figure 11. Transfer functions comparison—mouse (Aurovist, 42 kV).

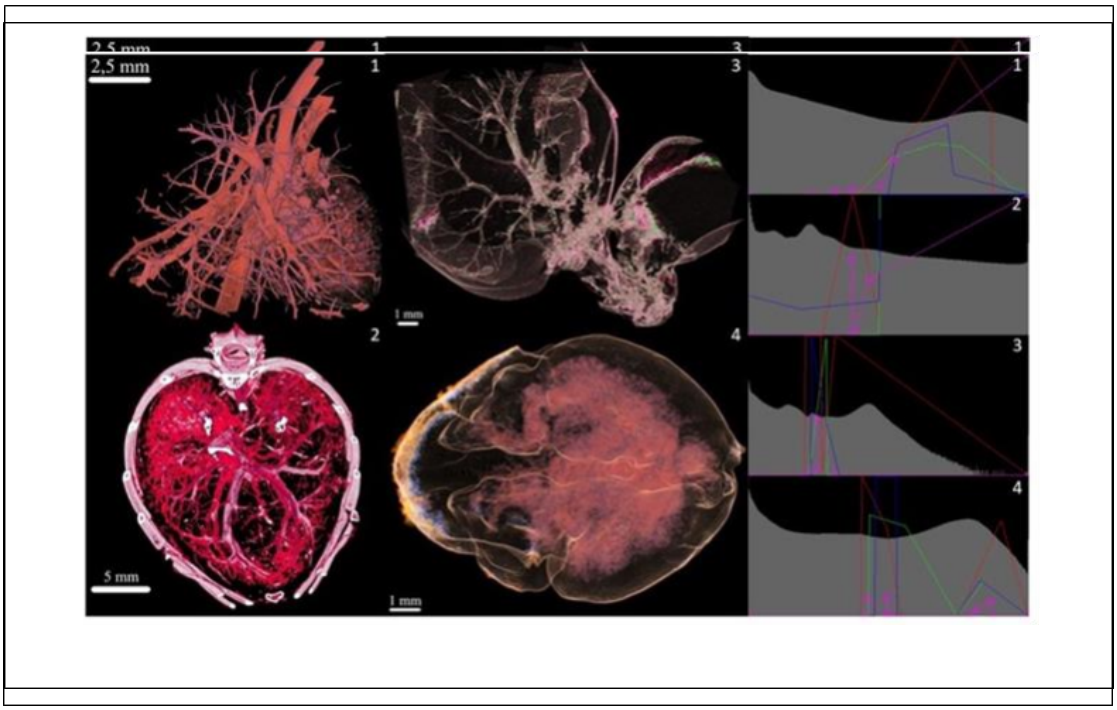

Figure 12. Contrast agents (**left panels**) and relevant transfer functions comparison (**right panels**): 1: Rat lungs and heart (Mercox, 34 kV); 2: Mouse hull (Aurovist, 42 kV); 3: Mouse liver (Omnipaque, 40 kV); and 4: Mouse brain (KI (potassium iodide) + Ethanol, 80 kV).

Due to the large number of results in the form of image data and transfer function, and due to the limited space for publication, only a few ones are presented below. Further significant visualizations, i.e., 18 examples, are available at higher resolution, i.e., with more details according to the contrast agent used, in Appendix A, specifically in Figures A1–A18. Part A1 (Figures A1 and A2) is related to the ethanol contrast, part A2 (Figures A3–A7) to Aurovist, part A3 (Figures A8–A11) to Omnipaque, part A4 (Figures A12–A16) to potassium iodide (KI) in 20% ethanol solution and part A5 (Figures A17 and A18) to Mercox resin. Captions of these figures content detailed descriptions of all possible findings due to the

better contrast visualization. It is the reason why these figures are included with higher spatial resolution within the Appendix A.

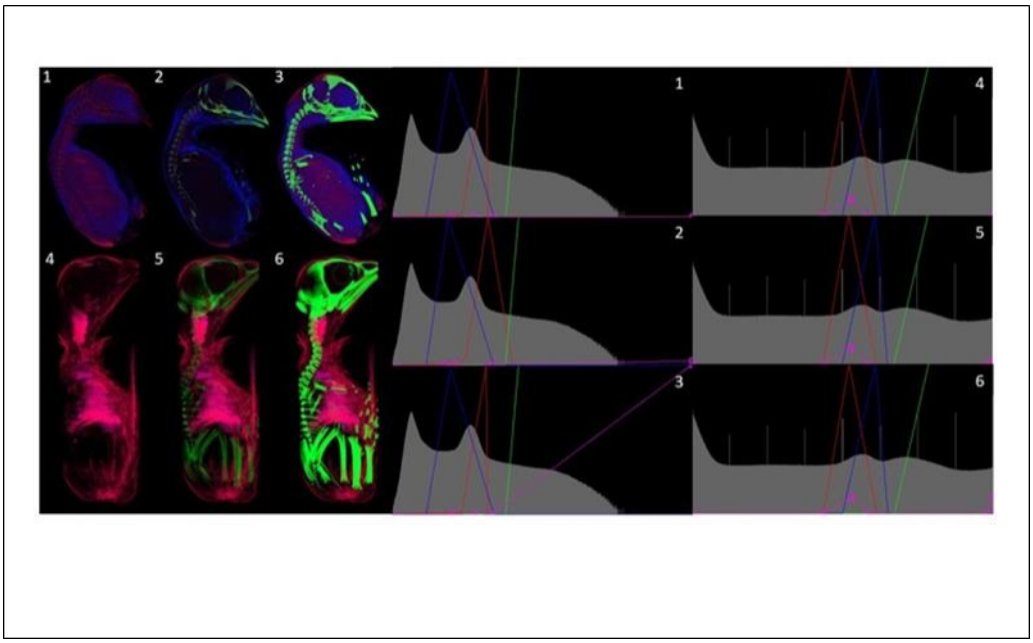

Figure 13. Acquisition voltage comparison in 19 days old chicken. Ethanol, 100 kV (1–3) and 40 kV (4–6).

4. Discussion

The main finding of this study is that there is a statistically significant monotonic relationship between the centroid of the area under the LUT curve and the number of days for which the animal sample was stored in the ethanol solution. H1 of the first hypothesis that the Spearman's correlation coefficient does not equal zero ($r_1 = 0$) regarding this relationship was confirmed. On the other hand, there is no statistically significant monotonic relationship between the centroid of the area under the LUT curve and the concentration of the ethanol solution, see Tables 1–4. In this case, H1 of the second hypothesis that the Spearman's correlation coefficient does not equal zero ($r_2 = 0$) regarding this relationship was not confirmed. Within Table 4, we can see relevant average values for selected storage days of the specimen and related Hounsfield units, i.e., CT numbers as well. These values are very important and can be assigned to the centroid parameters of a LUT curve incorporating the relevant parameter of days for which the animal sample (mouse liver or kidney) was stored in ethanol solution.

Another finding of the study is that it is not possible to use one universal transfer function for proper soft tissue visualization of CT images. The use of an appropriate contrast agent has a very significant effect on soft tissue visualization. It was possible to visualize the capillaries inside the chicken flesh in the phantom vasculature. In the case of the mouse heart, it was possible to segment and colorfully distinguish the tissue of the heart muscle from the rest of the blood vessels.

Due to the lack of one optimal and universal transfer function (LUT), a total of 53 transfer functions were designed using CTvox software [13] and optimized to highlight soft tissues in particular.

In the case of the mouse liver, mainly its external structures can be seen, while in the case of the kidney, brain, and heart, the internal structures are partially visible. In the mouse leg specimen, the transfer function emphasizes partly soft tissue and partly hard tissue (bone).

For the corrosive preparations, the soft tissue structures are shown by the contrast created between the Mercox resin and the air. Since the CT numbers of the synthetic resin

are around 70 HU [2], it is possible to speak of a soft tissue equivalent in this case (range 40–80 HU).

Unfortunately, it was not possible to properly visualize soft tissues or organs from any of the chick scans. In fact, it is not certain that the scan of a stained chicken head of a 19-day-old chick at an anode voltage of 40 kV succeeded in highlighting just the tongue of this chick, or whether it is only the cartilaginous part of its beak.

In ex vivo samples of chickens prepared in ethanol and formaldehyde solutions, there was a presumption of contrast in the CT images through protein coagulation. This assumption was probably only partially borne out and the result shows the interior of the chicken stained differently in blue and red, corresponding to a slight difference in CT numbers of otherwise further visualizable soft tissue. Furthermore, the ethanol solution in whole chickens did not have the opportunity to penetrate and subsequently evaporate from the animal cavities, which would have caused the solution to be replaced by air, which would have further caused better contrast in the CT images (comparable to the evaporation of ethanol from the cavities of the animal organs evaporated therein).

It is also interesting to note that the plastic straw made of polyethylene has approximately the same CT number as the chicken meat and therefore cannot be distinguished from the meat as it passes through it. The glass capillary was the best of all materials to see, as the glass–air interface is a very high contrast object against soft tissue. This was followed by a larger diameter silicone capillary and the third was a smaller diameter capillary. Thus, in contrast to polyethylene, all other materials were clearly distinguishable from chicken meat (Figure 1).

In the majority of cases, the output of CTvox shows that using a lower anode voltage is the optimal choice for scanning soft tissue on CT. In the case of bone segmentation, the choice of voltage did not play any significant role. For a more prominent presentation of the results, the processing of the oldest chicks prepared in ethanol was deliberately chosen, mainly because the chick is not sufficiently anatomically developed until around day 19 after egg fertilization, as this is the age at which chicks usually hatch. When younger chicks were examined, many structures were not yet sufficiently developed and, therefore, not visible.

Four chicken samples also contained the contrast agent Aurovist, consisting of 15 nm gold nanoparticles. Specifically, there were two scans at 10 days of age and another two at 12 days of age; unfortunately, no internal (soft) anatomical structures could be identified in this case either. This may have been due to the short age of the chicks, which may not have developed these structures properly yet. A second explanation could be that very low amount of Aurovist contrast agent was injected into the sample.

The limitation of this study is the relatively small number of included images and contrast agents. Another limitation is the use of the purely experimental-based level of visualization, i.e., there is subjective dependence of operator and possible variable deviation. In the case of statistical processing of the data with different KI concentrations, only two different concentrations were used—50% and 100%—this was a limitation, also.

5. Conclusions

In addition to the contrast agents used above, there is possible to use other more suitable contrast agents with very interesting properties. The idea is to perform next study based on the optimal contrast agent selection with relevant LUT. There are prepared comparative experiments with the set of such contrast agents as Sonovue, Iomeron, Optison, Omnipaque, Visipaque, Xenetix, Optiray, and Ultravist to be able to select appropriate one. However, there is assumed utilization of the semi-automatic/automatic LUT setup.

Author Contributions: Conceptualization and methodology, J.M. and J.H.; software, B.G.; validation, J.M. and P.Z.; formal analysis, J.R.; investigation, J.R.; resources, J.M.; data curation, J.M.; writing—original draft preparation, B.G. and J.H.; writing—review and editing, P.Z., G.G., A.L., A.M.; visualization, B.G.; supervision, P.Z.; project administration, J.M.; funding acquisition, J.M. All authors have read and agreed to the published version of the manuscript.

Funding: This research was funded by EU (European Regional Development Fund) and state budget of the Czech Republic, grant number CZ.02.1.01/0.0/0.0/16_019/0000766. The project was supported by Ministry of Education, Youth and Sports of the Czech Republic, Czech Technical University in Prague and Charles University.

Institutional Review Board Statement: The study was approved by the local Ethical Committees of the First and Third Faculty of Medicine, Charles University, Prague, Czech Republic (24185/2019). The animals were treated in accordance with the guidelines defined by the ethical committee, which follows the National Advisory Committee for Laboratory Animal Research (NAC LAR) guidelines. Handling of animals was performed in accordance with the Helsinki Declaration (seventh revision, 2013).

Informed Consent Statement: Not applicable.

Data Availability Statement: The complete original data are not publicly available due to large volume. However, there are available all LUTs as images and *.tf files and relevant images as well. Please, use the link within the [23].

Acknowledgments: There were used uncommercial licenses of software measure CT from Phywe [11,12], CTvox [13] and NRecon [15] from Bruker and Dragonfly [14] from ORS. We would like to thank Phywe, Bruker, and Object Research Systems for their kind support and feedback.

Conflicts of Interest: The authors declare no conflict of interest.

Appendix A

After reconstructing the data with NRecon, we designed several transfer functions in CTvox to emphasize the different structures of the selected samples, especially soft tissues. The CTvox outputs are divided into 5 subsections—according to the method of sample preparation or contrast used. This appendix is an additional section that contains details and data supplemental to the main text above (see the Results section). Figures of replicates for experiments of which representative data are shown in the main text above are added here with higher spatial resolution and detailed description.

Appendix A.1. Ethanol

For the preparations of chickens in ethanol solutions, we have designed transfer characteristics/functions highlighting their structures with different intensities of bone highlighting and then stained the samples with them.

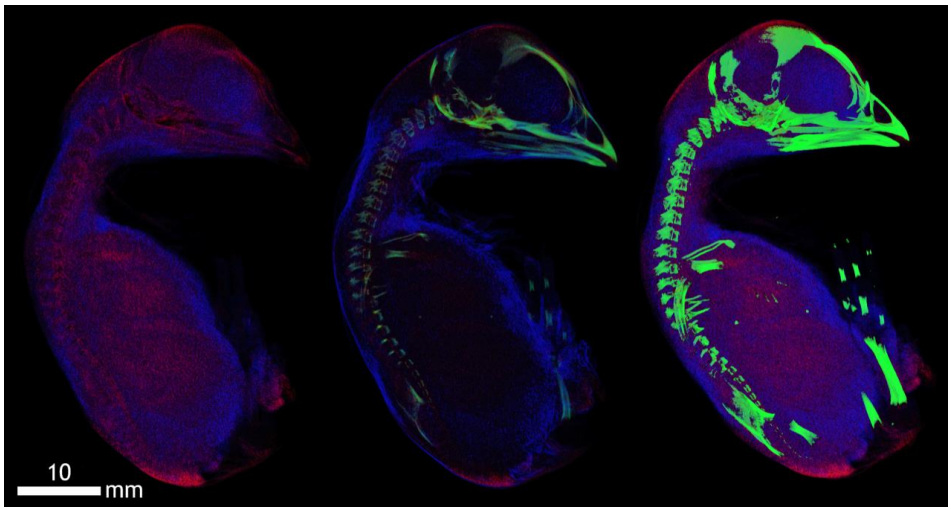

Figure A1. Dyed 19-day-old chicken (acquisition at anode voltage 100 kV, contrast agent ethanol). Ethanol fixed the surface structures of the soft tissues of the skin. The transition of the cartilaginous base of the skeleton (spine, skull, limbs) into bone forms is also shown.

Figure A2. Dyed 19-day-old chicken (acquisition at anode voltage 40 kV, contrast agent ethanol). Imaging after 5 days of ethanol fixation with incipient soft tissue contrast of the trachea, diaphragm, and heart muscle. The contrast in this phase of fixation also corresponds to the density of the surface structures of skin derivatives (feathers).

Appendix A.2. Aurovist

In ex vivo mice with a gold nanoparticles contrast agent (Aurovist), we have designed transfer characteristics/functions that colorfully highlight soft tissue structures, particularly in blood vessels and airways.

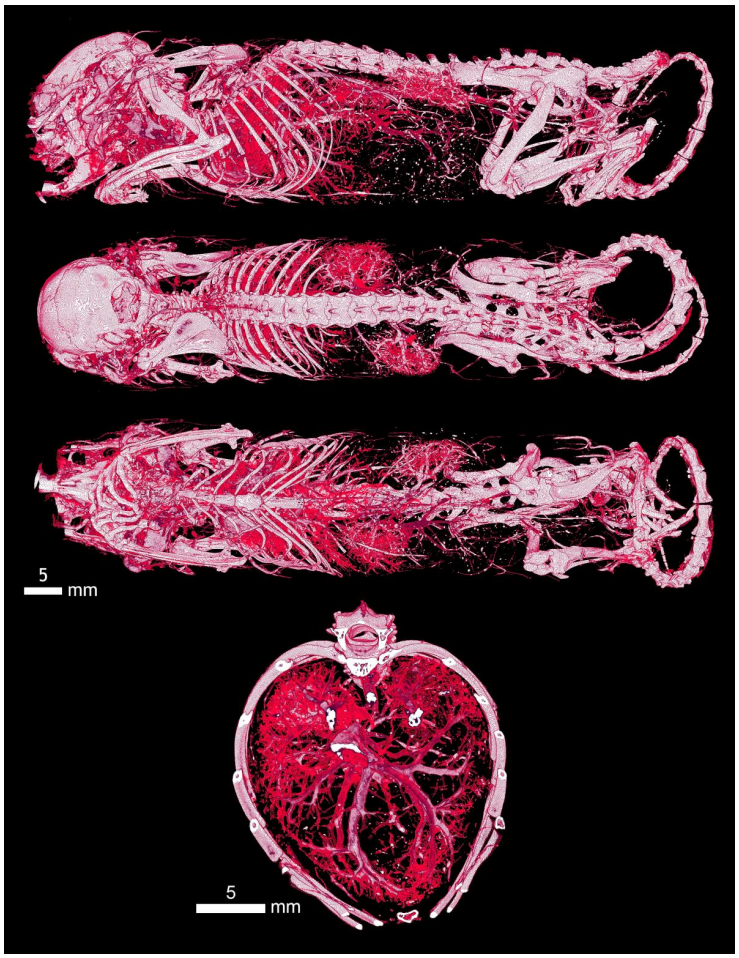

Figure A3. The Aurovist intravascular contrast displayed the entire vascular bed of the mouse. Here, is clearly visible the vasculature of the kidneys and their placement in the retroperitoneum on the

sagittal section, the vessels of the thoracic organs, the hepatic vessels of all lobes, and the supply of the intestines in the abdominal cavity and pelvic plexus. In the section at the level of the thorax, there is a detail of the pulmonary system, where, according to the symmetry of the distribution and branching of the vessels, we can also describe their loss due to occlusion.

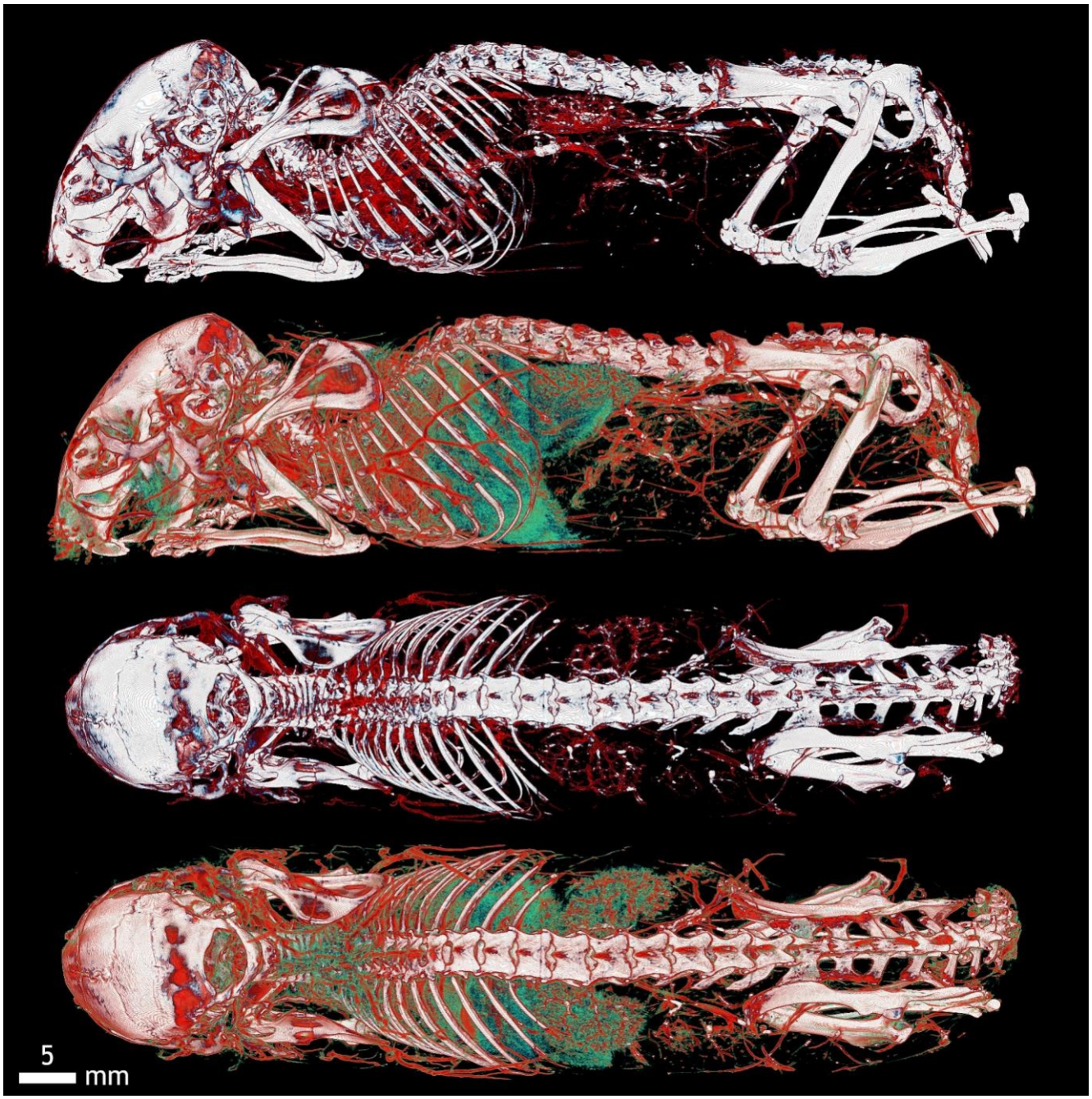

Figure A4. Color resolution of mouse vessels on the body surface (red) and internal organs (green). This distinction also offers a comprehensive view important for the orientation and description of superficial and parietal vessels. In the head area is visible in the external carotid artery branching, then interscapular brown fat vessels, superficial thoracic branching of the thoracic artery and intercostal vessels, parietal lumbar and sacral vessels, as well as plexuses around the spinal canal and limb vessels. The blood vessels of the kidneys and liver here form a network corresponding to the location of the organs in the abdominal cavity, the blood vessels of the heart and lungs to the organs in the chest. This arrangement allows the vessels to be compared at different topographic sites in the body.

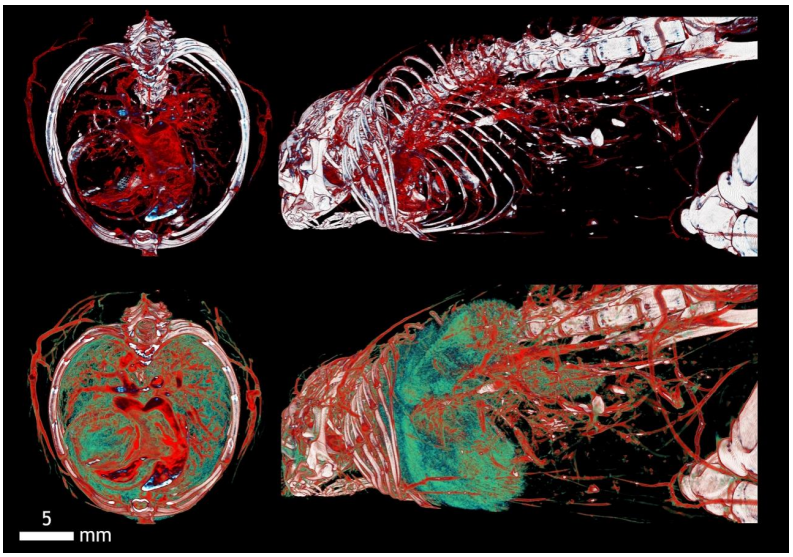

Figure A5. Due to the intravascular contrast of Aurovist, a detailed section of the chest shows the vascular supply of the lungs and its perfusion. Simultaneous view of the bronchial tree allows comparison with respect to the ventilation of individual lung segments. Thus, it is possible to distinguish pathologies in the vascular system in terms of occlusion, embolism, or proliferation in tumor pathology and at the same time monitor the bronchial tree due to air contrast and pathology of reduced aeration in atelectasis and increased air space due to disruption of intrabronchial septum in emphysema.

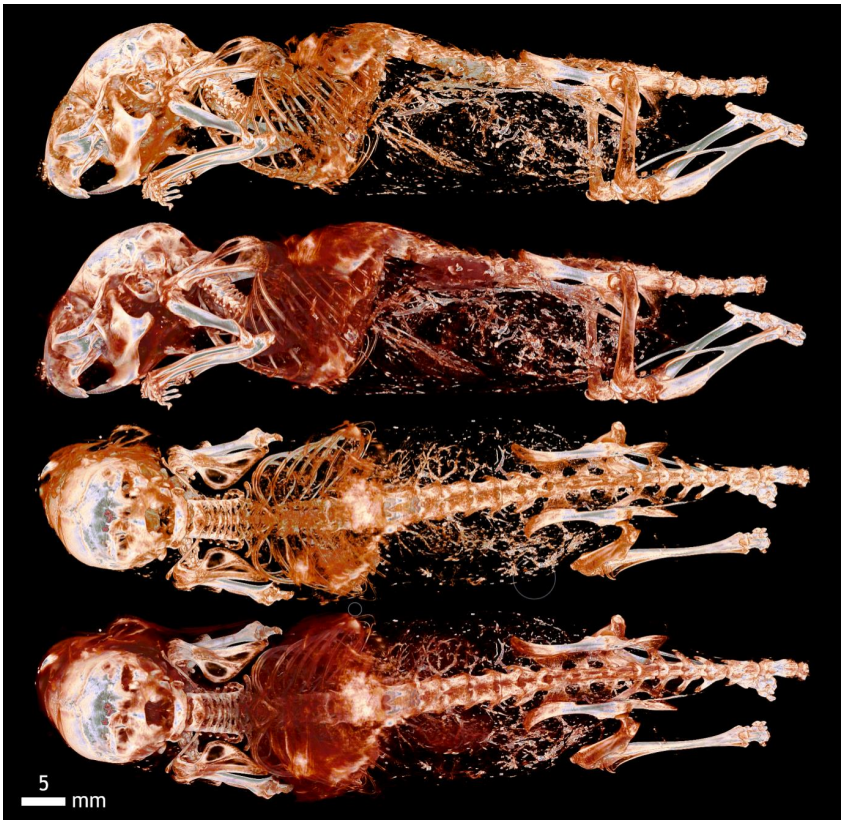

Figure A6. Detail view of the vascular system of the lungs in the chest of the mouse with Aurovist contrast in the sagittal and ventrodorsal scans and detail of the bronchial tree of the lung parenchyma in the same position. It is possible to compare pathologies in the vascular bed and bronchial branching separately.

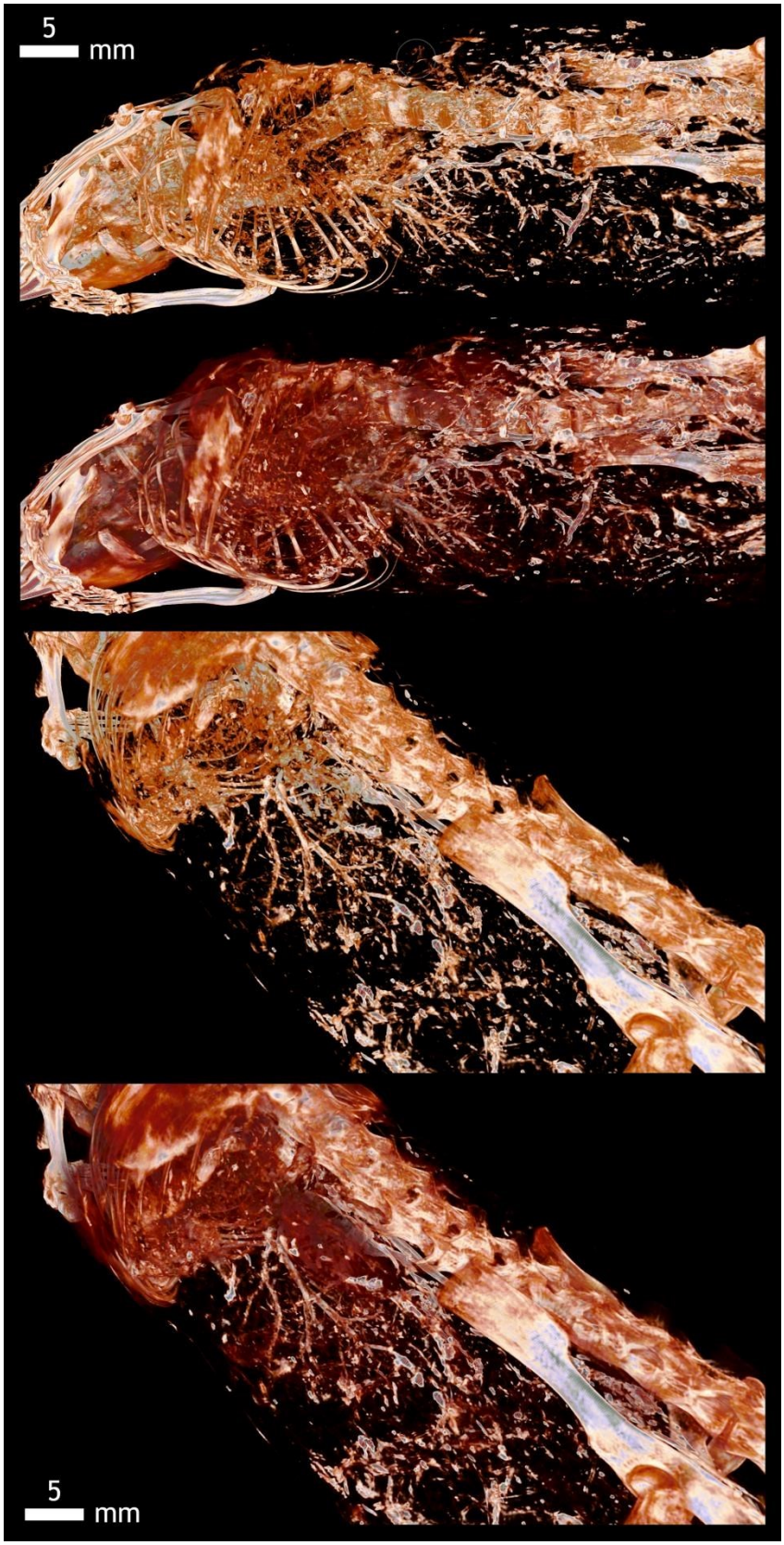

Figure A7. Transition of the thoracic and abdominal cavities and vascular supply of the lungs, heart, and the vessels of the liver and intestine. Simultaneous imaging of the bronchial ventilated tree helps to differentiate individual vascular systems. Detail of the hepatic vessels shows their segmentation into individual lobes. Another vascular system in the abdominal cavity corresponds to the largest perfusion in the bloodstream of the small and large intestine.

Appendix A.3. Omnipaque

In mouse organs prepared with Omnipaque contrast agent, transfer characteristics/functions highlighting the soft tissues of these organs were designed.

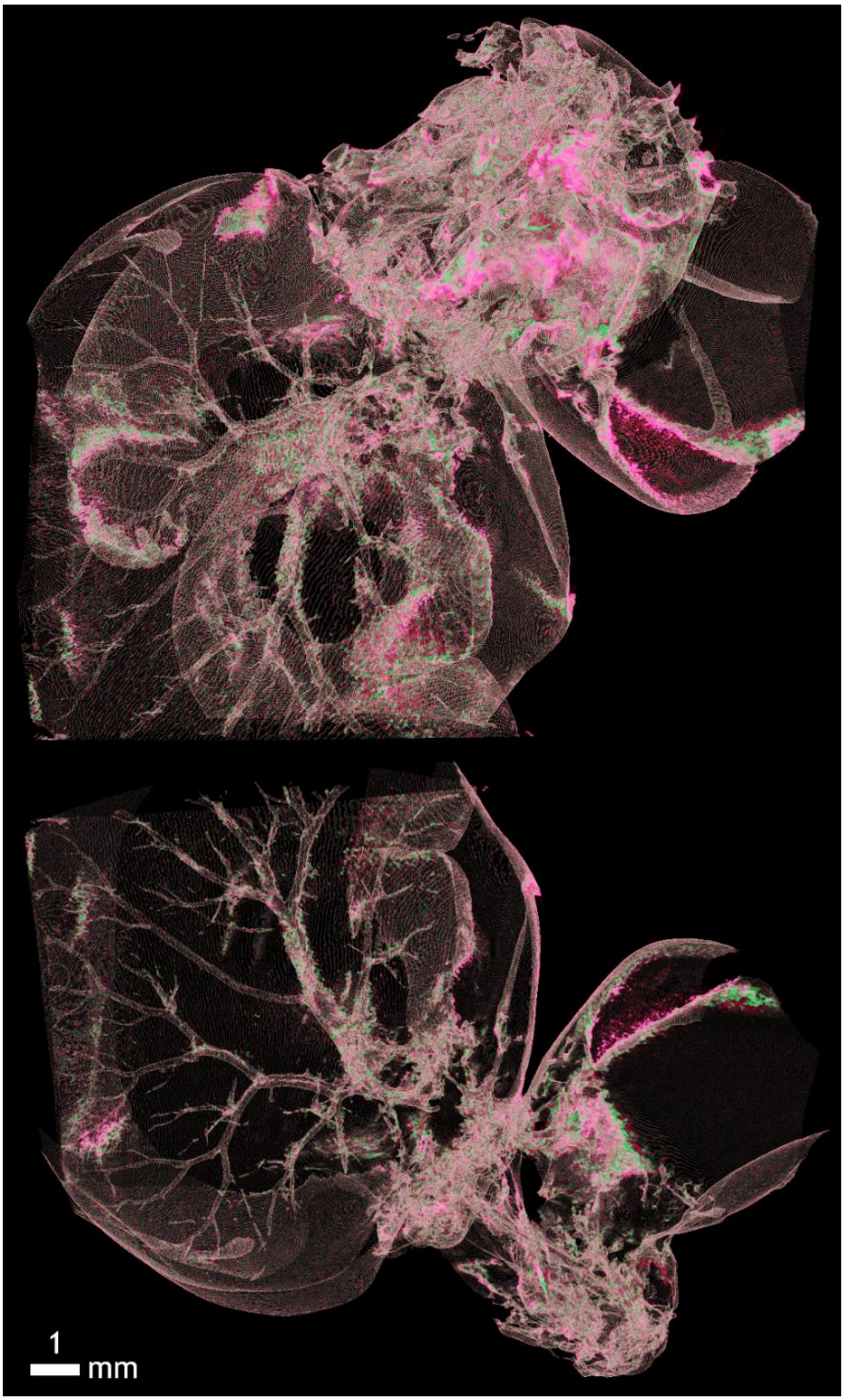

Figure A8. Detailed view of the lobe of the liver and segmental vessels using Omnipaque contrast. Here, is a physiological finding. According to the drawing of the vasculature, we can also describe possible pathological conditions, reconstruction of the liver parenchyma, and its irregular vascular bed or proliferation of blood vessels in tumors.

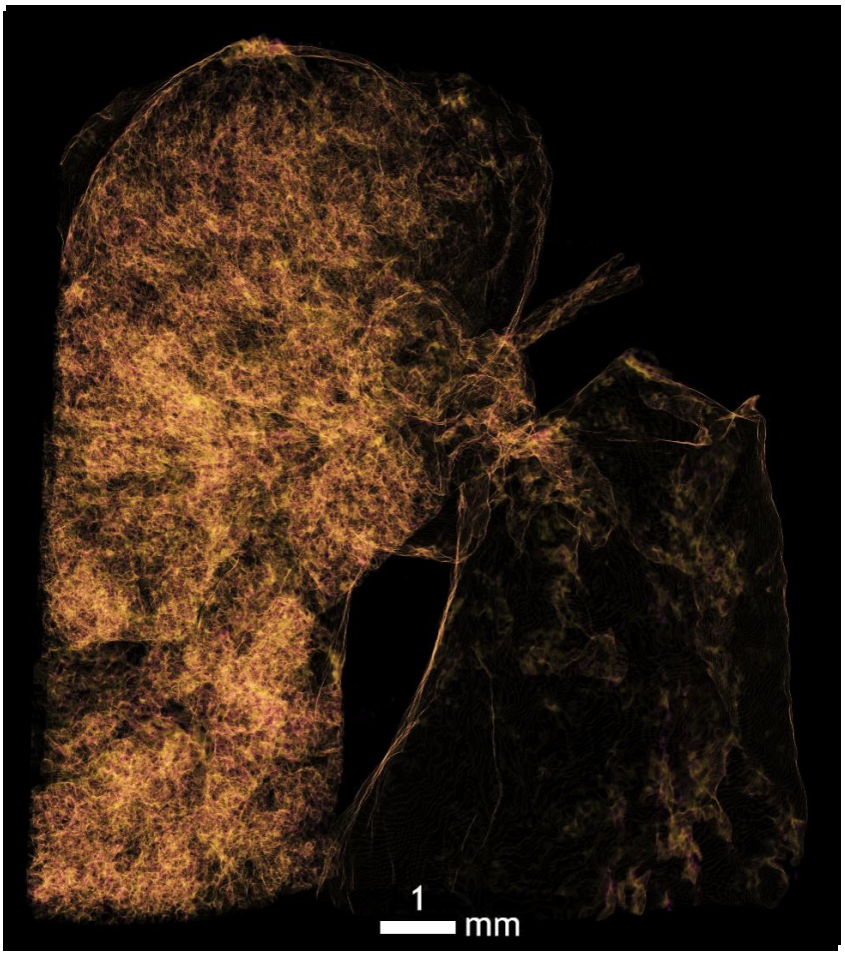

Figure A9. Ideal right lung position for imaging of bronchial branching down to alveolar levels using Omnipaque contrast. The right lung is rotated in a different position and it is possible that post-mortem it collapsed, mechanically vented, or was fixed in the fluid.

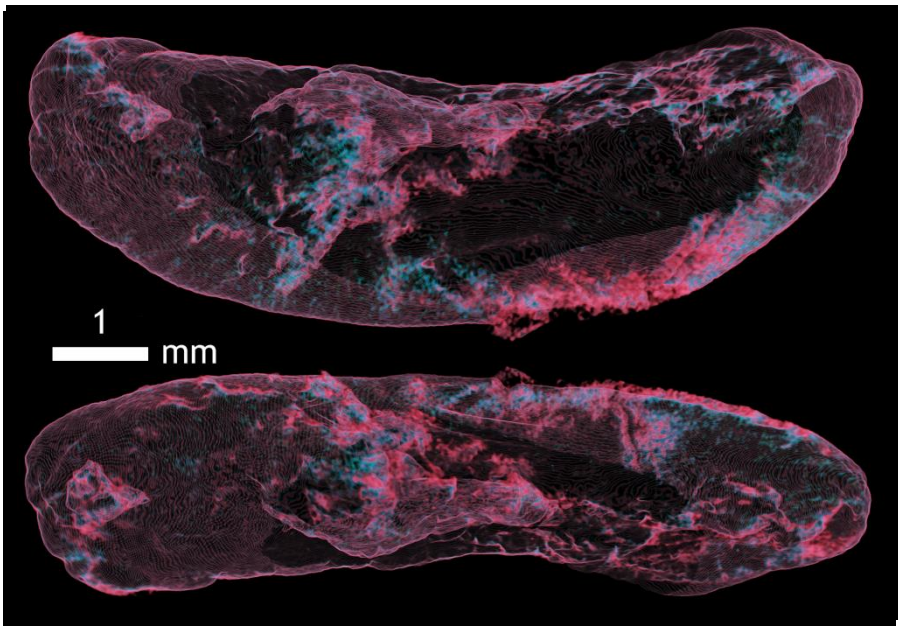

Figure A10. Imaging of the capsule of the spleen and superficial vessels in fascial tissue in two positions using Omnipaque contrast.

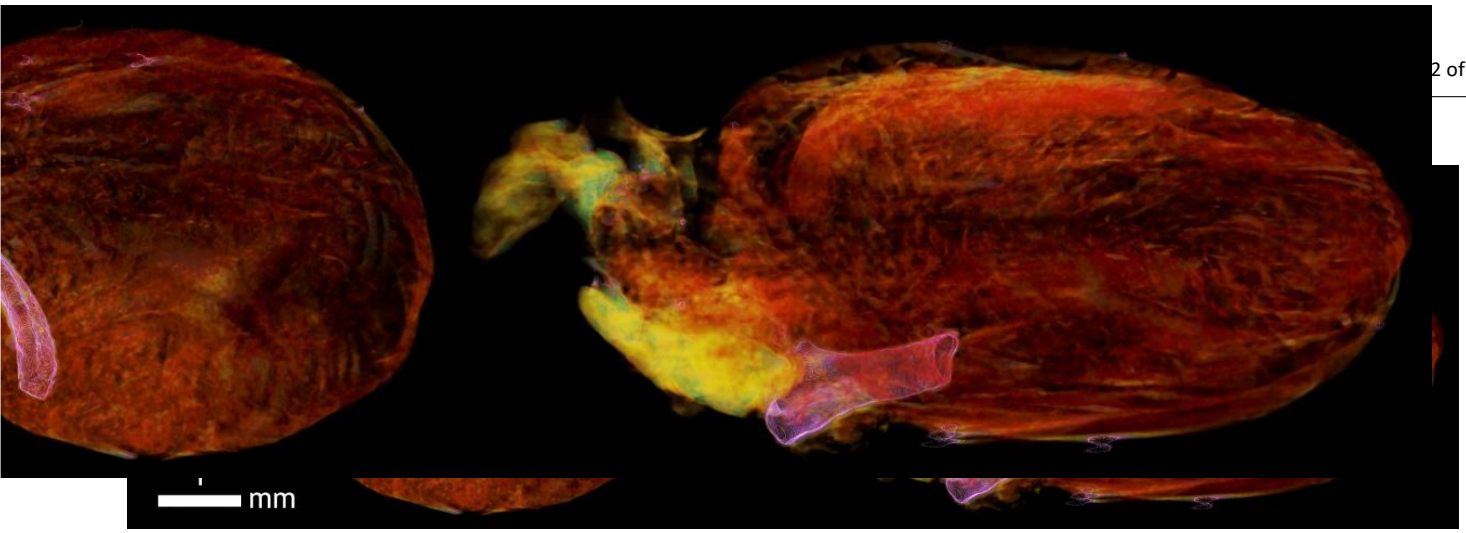

Figure A11. Imaging of superficial vessels of the epicardium and sub fascial layer of the heart.

Appendix A.4. Potassium iodide (KI) in 20% Ethanol Solution

To emphasize soft tissue organs loaded in a solution of dissolved potassium iodide in 20% ethanol solution, additional LUTs were designed and optimized.

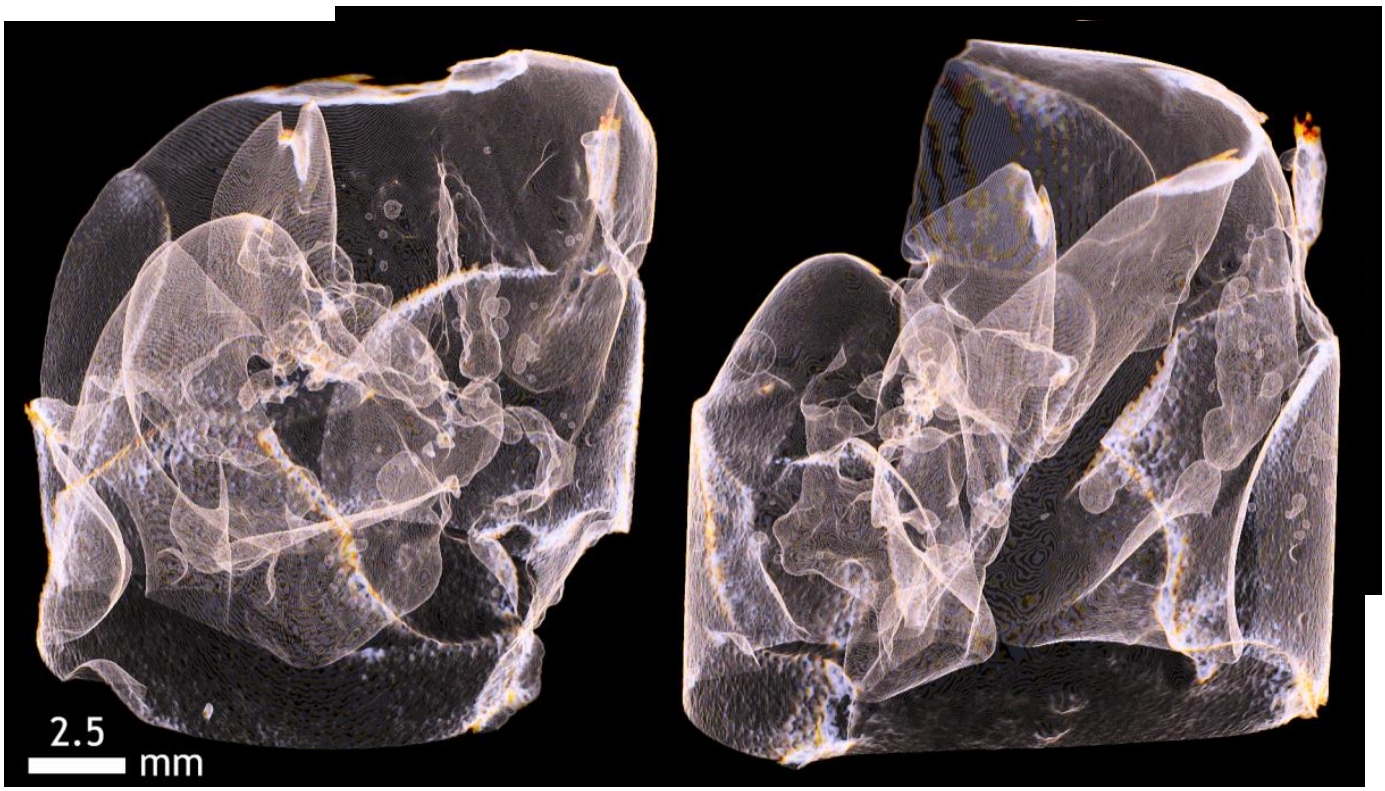

Figure A12. Imaging of the superficial capsule of the liver and division of the hepatic lobes.

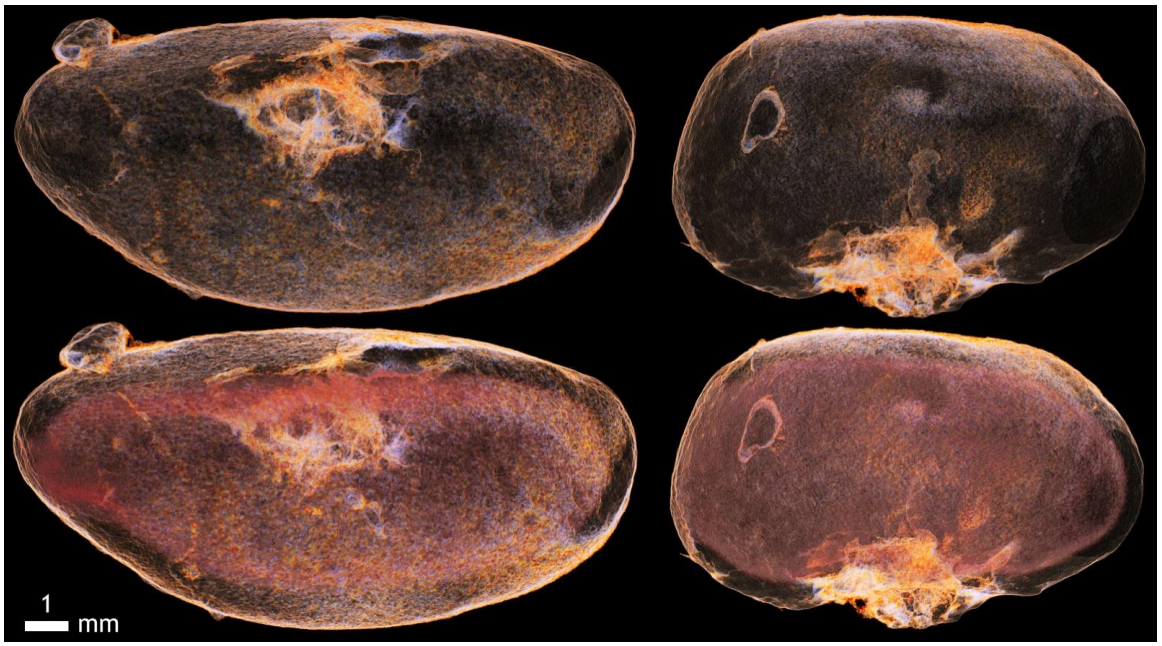

Figure A13. Iodine contrast and imaging of the kidney capsule, including the pathology of the cystic formation on the surface of the kidney.

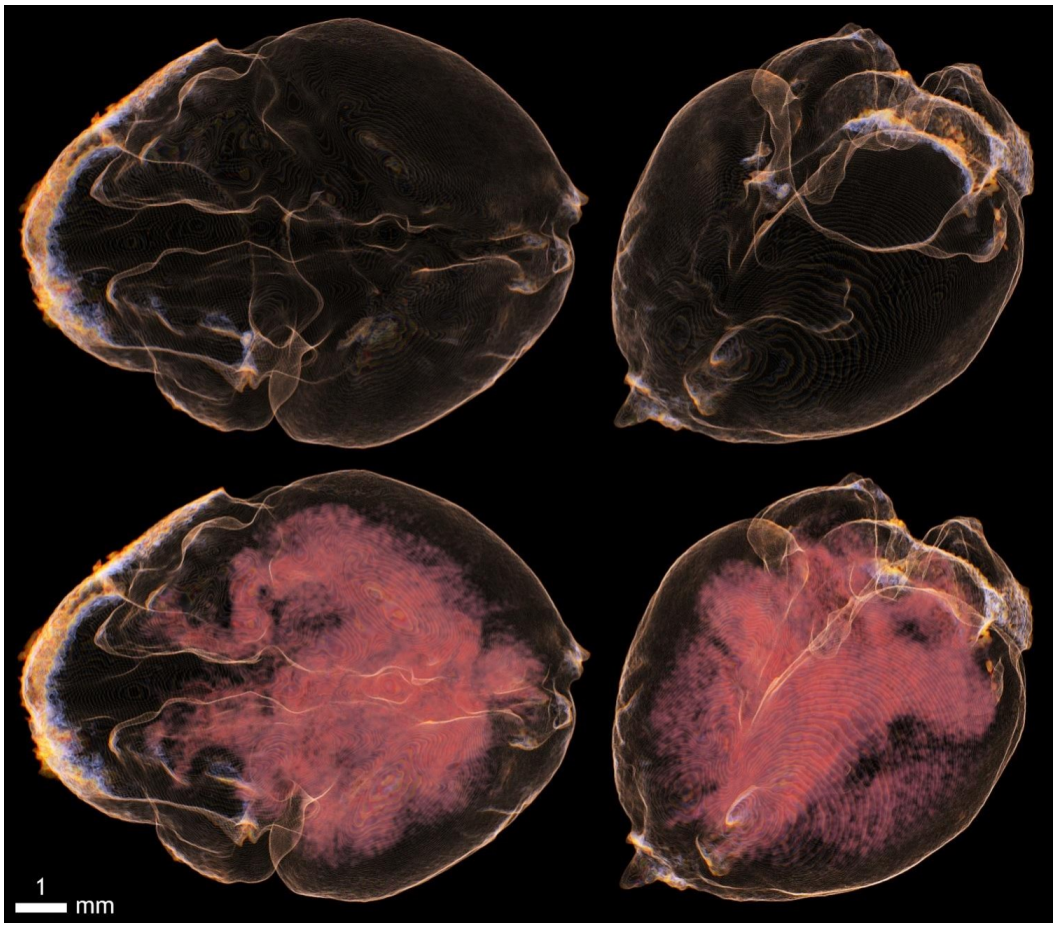

Figure A14. Imaging of the cerebral lobes and internal ventricular system with KI and 20% ethanol.

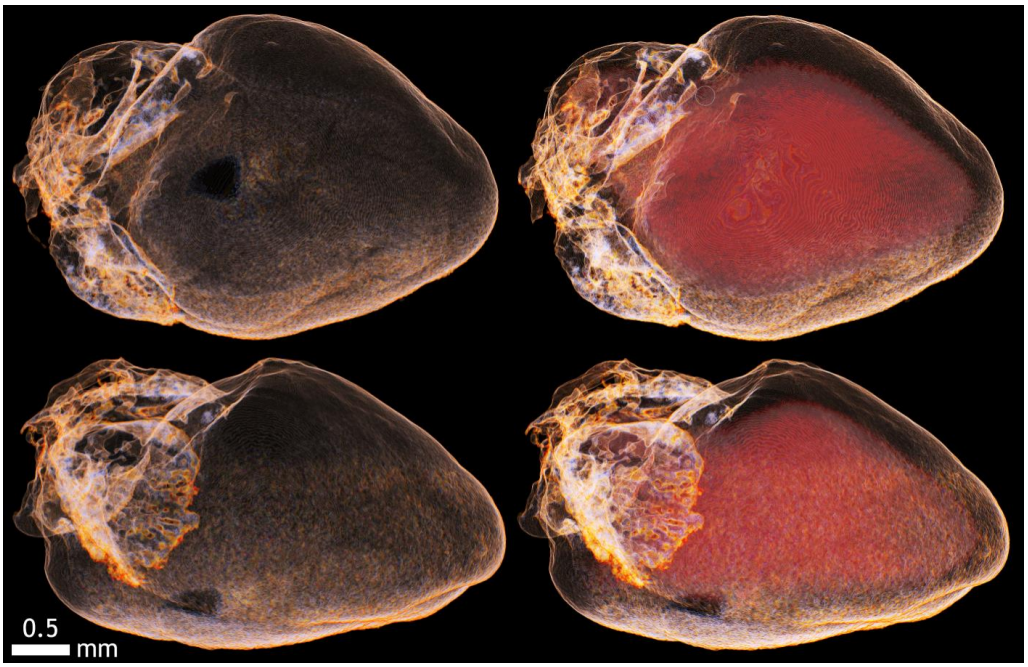

Figure A15. Imaging of the epicardium and endocardium of the heart and its cavities with KI and 20% ethanol.

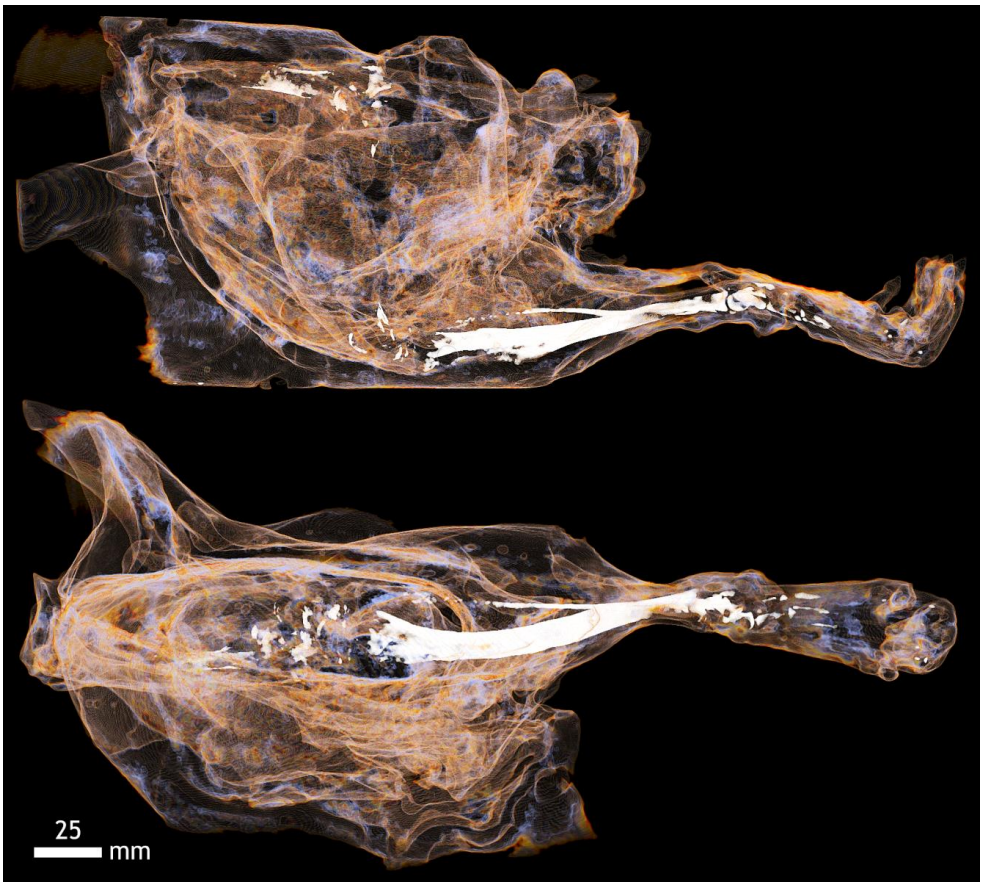

Figure A16. Contrast of fascia muscle groups on the hind limb of mice with KI and 20% ethanol. The bones of the limb can be seen in detail, including the small tarsal bones of the foot.

Appendix A.5. Mercox (Resin)

For corrosive slides, transfer characteristics/functions emphasizing only the soft tissue structures (not the soft tissue itself) have been proposed using a contrast between resin and air. The images show the rabbit and rat airways, and in the case of the rat, the heart is visible along with the vasculature as well.

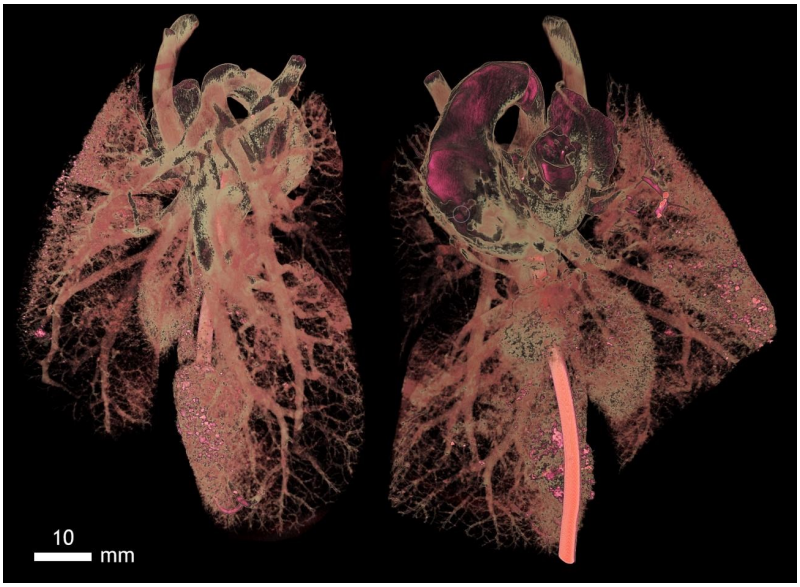

Figure A17. Rabbit lung vessels visualized by Mercox contrast, a corrosive preparation. Here, the passage of blood vessels in post mortem is ensured by intravenous application of resin by continuous pressure. It is possible to modify vascular ligatures in experiments and, thus, display a failure that is similar to embolism. It is also possible to subsequently measure the angle of the segmental vessels distances and their diameters.

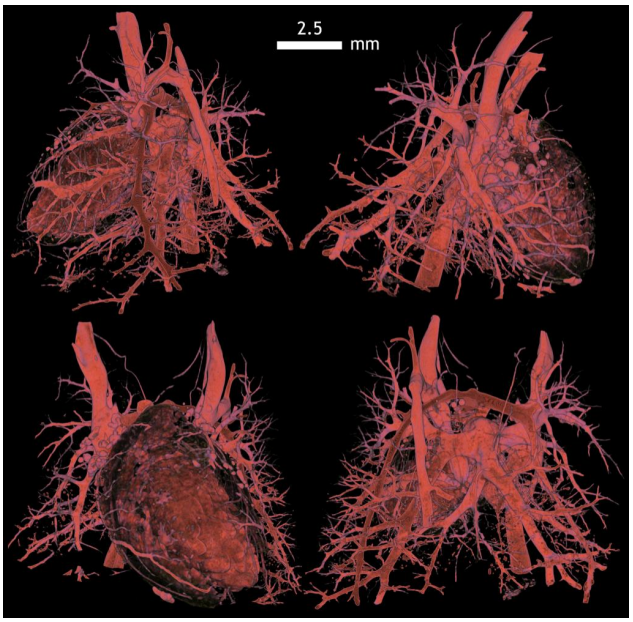

Figure A18. The corrosive specimen of the heart and blood vessels shows both the coronary arter-ies for the heart, the basic platform for incipient myocardial infarction, and the branching of the pulmonary artery and pulmonary artery diameters and their angles of spacing and segmentation. Here, is a physiological finding. The arrangement of the pulmonary arteries and their branching is disturbed in pulmonary embolism, vascular wall pathology and also in lung tumors.

134

Parameter	Value	
object-source distance	310	detector-source distance

	Physical Unit
	mm
	mm

Appendix B.

This appendix is an additional section that contains details and data supplemental to the main text from the point of view of the experimental setting of both setups, i.e., Phywe and Bruker systems.

Table A1. Values of set parameters on the PHYWE XR 4.0 assembly.

Parameter	Value	Physical Unit
object-source distance	310	mm
detector-source distance	360	mm
anode voltage	35	kV
emission current	1	mA
pixel projection dimension	96	m
exposure time	500	ms
degree of rotation (increm.)	1.8	
binning [1]	500 500	pixels

[1] Explanation of binning is available within the [2,13].

The scan settings for scanning biological samples of chickens outside the shell with the SkyScan 1275 are shown in the following tables. The table header consists of a number followed by a capital letter D, this is the age of the chicken, which is given in days. This may be preceded either by another number followed by the capital letter E, in which case it is the concentration of the ethanol solution in which the chicken was prepared, or by the letter F, which indicates that the chicken was prepared in a formaldehyde solution. In four cases, the concentration of the Ethanol solution is preceded by the capital letter A, this is the contrast agent Aurovist.

Table A2. Values of set parameters on SkyScan 1275.

Parameter	Value 50E5D	Value 100E5D	Value F5D	Value 50E6D	Value 80E6D	Value 100E6D	Physical Unit
object-source distance	40.97	40.97	40.97	40.97	40.97	40.97	mm
detector-source distance	286	286	286	286	286	286	mm
anode voltage	50	50	50	50	50	50	kV
emission current	200	200	200	200	200	200	A m
pixel projection dimension	11.6	11.6	11.6	11.6	11.6	11.6	ms
exposure time	50	50	50	50	50	50	
degree of rotation (increm.)	0.2	0.2	0.2	0.2	0.2	0.2	pixel
binning [1]	1 1	1 1	1 1	1 1	1 1	1 1	

[1] Explanation of binning is available within the [2,13].

Table A3. Values of set parameters on SkyScan 1275.

Parameter	Value F6D	Value 80E7D	Value 100E7D	Value 80E8D	Value 80E9D	Value A80E10D	Physical Unit
object-source distance	40.97	48.39	48.39	57.22	71.47	92.67	mm
detector-source distance	286	286	286	286	286	286	mm
anode voltage	50	50	50	65	70	100	kV
emission current	200	200	200	153	142	100	A m
pixel projection dimension	11.6	13.7	13.7	16.2	20.24	26.24	ms
exposure time	50	50	50	36	36	35	pixel
degree of rotation (increm.)	0.2	0.2	0.2	0.2	0.2	0.2	
binning [1]	1 1	1 1	1 1	1 1	1 1	1 1	

[1] Explanation of binning is available within the [2,13].

Table A4. Values of set parameters on SkyScan 1275.

Parameter	Value A80E10D	Value 80E10-11D	Value 80E10-11D	Value 50E11D	Value 80E12D	Physical Unit
object-source distance	71.47	60.75	67.9	92.67	80.4	mm
detector-source distance	286	286	286	286	286	mm
anode voltage	75	75	75	75	75	kV
emission current	133	133	133	133	133	A m
pixel projection dimension	20.24	17.2	19.23	26.24	22.77	ms
exposure time	36	36	36	36	500	pixel
degree of rotation (increm.)	0.2	0.2	0.2	0.2	0.2	
binning [1]	1 1	1 1	1 1	1 1	1 1	

[1] Explanation of binning is available within the [2,13].

Table A5. Values of set parameters on SkyScan 1275.

Parameter	Value A80E12D	Value A80E12D	Value 50E13D	Value 50E14D	Value 100E14D	Physical Unit
object-source distance	92.67	82.19	92.67	96.48	123.29	mm
detector-source distance	286	286	286	286	286	mm
anode voltage	75	75	75	75	80	kV
emission current	133	133	133	133	125	A m
pixel projection dimension	26.24	23.27	26.24	27.32	34.91	ms
exposure time	500	500	500	500	32	
degree of rotation (increm.)	0.2	0.2	0.2	0.2	0.2	pixel
binning [1]	1 1	1 1	1 1	1 1	1 1	

[1] Explanation of binning is available within the [2,13].

Table A6. Values of set parameters on SkyScan 1275.

Parameter	Value 50E15D	Value 50E15D	Value 50E16D	Value 100E18D	Value 100E18D	Physical Unit
object-source distance	146.51	142.94	178.67	169.74	176.89	mm
detector-source distance	286	286	286	286	286	mm
anode voltage	80	80	80	80	80	kV
emission current	125	125	125	125	125	A m
pixel projection dimension	41.48	40.47	50.59	48.06	50.08	ms
exposure time	32	32	32	33	33	pixel
degree of rotation (increm.)	0.2	0.2	0.2	0.2	0.2	
binning [1]	1 1	1 1	1 1	1 1	1 1	

[1] Explanation of binning is available within the [2,13].

Table A7. Values of set parameters on SkyScan 1275.

Parameter	Value 100E19D	Value 100E19D	Value 100E19D	Value 100E19D	Physical Unit
object-source distance	173.31	132.22	92.67	141.15	mm
detector-source distance	287	286	286	286	mm
anode voltage	40	80	100	100	kV
emission current	250	125	100	100	A m
pixel projection dimension	49.07	37.44	26.24	39.97	ms
exposure time	35	35	35	35	
degree of rotation (increm.)	0.2	0.2	0.2	0.2	pixel
binning [1]	1 1	1 1	1 1	1 1	

[1] Explanation of binning is available within the [2,13].

The scanning parameters for scanning biological samples of chickens in the shell with the SkyScan 1275 are shown in the following tables. The table header consists of a number followed by a capital letter D, this is the age of the chicken, which is given in days.

Table A8. Values of set parameters on SkyScan 1275.

Parameter	Value 8D	Value 9D	Value 10D	Value 11D	Value 12D	Physical Unit
object-source distance	155.45	146.51	151.87	137.58	153.66	mm
detector-source distance	286	286	286	286	286	mm
anode voltage	80	80	80	80	80	kV
emission current	125	125	125	125	125	A m
pixel projection dimension	44.01	41.48	43	38.95	43.51	ms
exposure time	36	36	36	36	36	
degree of rotation (increm.)	0.2	0.2	0.2	0.2	0.2	pixel
binning [1]	1 1	1 1	1 1	1 1	1 1	

[1] Explanation of binning is available within the [2,13].

Table A9. Values of set parameters on SkyScan 1275.

Parameter	Value 13D	Value 14D	Value 15D	Value 15D	Value 16D	Physical Unit
object-source distance	146.51	148.30	155.45	158.93	144.73	mm
detector-source distance	286	286	286	286	286	mm
anode voltage	80	80	80	80	80	kV
emission current	125	125	125	125	125	A m
pixel projection dimension	41.48	41.49	44.01	45	40.98	ms
exposure time	36	36	36	36	36	
degree of rotation (increm.)	0.2	0.2	0.2	0.2	0.2	pixel
binning [1]	1 1	1 1	1 1	1 1	1 1	

[1] Explanation of binning is available within the [2,13].

Table A10. Values of set parameters on SkyScan 1275.

Parameter	Value 17D	Value 18D	Value 18D	Value 19D	Physical Unit
object-source distance	159.02	157.23	167.95	150.09	mm
detector-source distance	286	286	286	286	mm
anode voltage	95	80	80	80	kV
emission current	105	125	125	125	A m
pixel projection dimension	45.03	44.52	47.55	42.50	ms
exposure time	36	36	36	36	
degree of rotation (increm.)	0.2	0.2	0.2	0.2	pixel
binning [1]	1 1	1 1	1 1	1 1	

[1] Explanation of binning is available within the [2,13].

Table A11. Values of set parameters on SkyScan 1275 for scanning of the 13 liver samples.

Parameter	Value 50E8D	Value 50E17D	Value 100E8D	Value 100E16D	Value 100E37D	Physical Unit
object-source distance	63.57	56.51	54.74	52.98	49.45	mm
detector-source distance	286	286	286	286	286	mm
anode voltage	30	40	30	35	40	kV
emission current	212	250	212	231	250	A m
pixel projection dimension	18.00	16.00	15.50	15.00	14.00	ms
exposure time	58	35	58	38	35	
degree of rotation (increm.)	0.2	0.2	0.2	0.2	0.2	pixel
binning [1]	1 1	1 1	1 1	1 1	1 1	

[1] Explanation of binning is available within the [2,13].

Table A12. Values of set parameters on SkyScan 1275 for scanning of the 11 kidneys samples.

Parameter	Value 50E7D	Value 50E16D	Value 100E7D	Value 100E16D	Value 100E37D	Physical Unit
object-source distance	28.26	28.26	30.02	28.26	28.26	mm
detector-source distance	286	286	286	286	286	mm
anode voltage	35	35	35	35	40	kV
emission current	231	231	231	231	250	A m
pixel projection dimension	8.00	8.00	8.50	8.00	8.00	ms
exposure time	35	38	35	38	35	
degree of rotation (increm.)	0.2	0.2	0.2	0.2	0.2	pixel
binning [1]	1 1	1 1	1 1	1 1	1 1	

[1] Explanation of binning is available within the [2,13].

Table A13. Values of set parameters on SkyScan 1275.

Parameter	Value 17D	Value 18D	Value 18D	Value 19D	Physical Unit
object-source distance	159.02	157.23	167.95	150.09	mm
detector-source distance	286	286	286	286	mm
anode voltage	95	80	80	80	kV
emission current	105	125	125	125	A m
pixel projection dimension	45.03	44.52	47.55	42.50	ms
exposure time	36	36	36	36	
degree of rotation (increm.)	0.2	0.2	0.2	0.2	pixel
binning [1]	1 1	1 1	1 1	1 1	

[1] Explanation of binning is available within the [2,13].

Table A14. Values of set parameters on SkyScan 1275.

Parameter	Value 17D	Value 18D	Value 18D	Value 19D	Physical Unit
object-source distance	159.02	157.23	167.95	150.09	mm
detector-source distance	286	286	286	286	mm
anode voltage	95	80	80	80	kV
emission current	105	125	125	125	A m
pixel projection dimension	45.03	44.52	47.55	42.50	ms
exposure time	36	36	36	36	pixel
degree of rotation (increm.)	0.2	0.2	0.2	0.2	
binning [1]	1 1	1 1	1 1	1 1	

[1] Explanation of binning is available within the [2,13].

Table A15. Values of set parameters on SkyScan 1275.

Parameter	Value 17D	Value 18D	Value 18D	Value 19D	Physical Unit
object-source distance	159.02	157.23	167.95	150.09	mm
detector-source distance	286	286	286	286	mm
anode voltage	95	80	80	80	kV
emission current	105	125	125	125	A m
pixel projection dimension	45.03	44.52	47.55	42.50	ms
exposure time	36	36	36	36	
degree of rotation (increm.)	0.2	0.2	0.2	0.2	pixel
binning [1]	1 1	1 1	1 1	1 1	

[1] Explanation of binning is available within the [2,13].

Table A16. Values of set parameters on SkyScan 1275.

Parameter	Value 17D	Value 18D	Value 18D	Value 19D	Physical Unit
object-source distance	159.02	157.23	167.95	150.09	mm
detector-source distance	286	286	286	286	mm
anode voltage	95	80	80	80	kV
emission current	105	125	125	125	A m
pixel projection dimension	45.03	44.52	47.55	42.50	ms
exposure time	36	36	36	36	pixel
degree of rotation (increm.)	0.2	0.2	0.2	0.2	
binning [1]	1 1	1 1	1 1	1 1	

[1] Explanation of binning is available within the [2,13].

The scan settings for scanning mouse biological samples with Aurovist contrast agent (letter A), rabbit and rat biological samples with Mercox resin contrast agent (letter M), and mouse organ biological samples with Omnipaque contrast agent (letter O) and potassium iodide (KI) contrast agent dissolved in 20% ethanol solution (letters KI) with the SkyScan 1275 kit are shown in the following tables.

Table A17. Values of set parameters on SkyScan 1275.

Parameter	Value A-Mouse	Value M-Rabbit	Value M-Rat	Physical Unit
object-source distance	92.67	148.30	62.54	mm
detector-source distance	286	286	286	mm
anode voltage	42	46	34	kV
emission current	238	217	227	A m
pixel projection dimension	26.24	41.99	17.71	ms
exposure time	99	35	41	pixel
degree of rotation (increm.)	0.2	0.2	0.2	
binning [1]	1 1	1 1	1 1	

[1] Explanation of binning is available within the [2,13].

Table A18. Values of set parameters on SkyScan 1275.

Parameter	Value O-Liver	Value O-Lungs	Value O-Spleen	Value O-Heart	Physical Unit
object-source distance	58.96	33.95	28.59	33.95	mm
detector-source distance	286	286	286	286	mm
anode voltage	40	54	54	40	kV
emission current	238	185	185	238	A m
pixel projection dimension	16.70	19.22	16.19	9.61	ms
exposure time	35	50	50	35	
degree of rotation (increm.)	0.2	0.4	0.4	0.2	pixels
binning [1]	1 1	2 2	2 2	1 1	

[1] Explanation of binning is available within the [2,13].

Table A19. Values of set parameters on SkyScan 1275.

Parameter	Value KI-Liver	Value KI-Kidney	Value KI-Brain	Value KI-Heart	Value KI-Leg	Physical Unit
object-source distance	107.21	32.16	117.93	39.31	178.67	mm
detector-source distance	286	286	286	286	286	mm
anode voltage	80	80	80	80	80	kV
emission current	125	125	125	125	125	A m
pixel projection dimension	30.36	9.11	33.39	11.13	50.59	ms
exposure time	35	35	35	35	35	
degree of rotation (increm.)	0.2	0.2	0.2	0.2	0.2	pixel
binning [1]	1 1	1 1	1 1	1 1	1 1	

[1] Explanation of binning is available within the [2,13].

References

1. Liguori, C.; Frauenfelder, G.; Massaroni, C.; Saccomandi, P.; Giurazza, F.; Pitocco, F.; Marano, R.; Schena, E. Emerging clinical applications of computed tomography. Med. Devices **2015**, 8, 265–278. [CrossRef]
2. Stock, S.R. Microcomputed Tomography: Methodology and Applications, 2nd ed.; CRC Press/Taylor and Francis: Boca Raton, FL, USA, 2020.
3. Vickerton, P.; Jarvis, J.; Jeffery, N. Concentration-dependent specimen shrinkage in iodine-enhanced microCT. J. Anat. **2013**, 223, 185–193. [CrossRef] [PubMed]
4. Silva, J.M.D.E.; Zanette, I.; Noel, P.B.; Cardoso, M.B.; Kimm, M.A.; Pfeiffer, F. Three-dimensional non-destructive soft-tissue visualization with X-ray staining micro-tomography. Sci. Rep. **2015**, 5, 14088. [CrossRef] [PubMed]
5. Metscher, B.D. MicroCT for comparative morphology: Simple staining methods allow high-contrast 3D imaging of diverse non-mineralized animal tissues. BMC Physiol. **2009**, 9, 11. [CrossRef] [PubMed]
6. Patzelt, M.; Mrzilkova, J.; Dudak, J.; Krejci, F.; Zemlicka, J.; Karch, J.; Musil, V.; Rosina, J.; Sykora, V.; Horehledova, B.; et al. Ethanol fixation method for heart and lung imaging in micro-CT. Jpn. J. Radiol. **2019**, 37, 500–510. [CrossRef] [PubMed]
7. Dudak, J.; Zemlicka, J.; Karch, J.; Patzelt, M.; Mrzilkova, J.; Zach, P.; Hermanova, Z.; Kvacek, J.; Krejci, F. High-contrast X-ray micro-radiography and micro-CT of ex-vivo soft tissue murine organs utilizing ethanol fixation and large area photon-counting detector. Sci. Rep. **2016**, 6, 30385. [CrossRef] [PubMed]
8. McNitt-Gray, M.F.; Taira, R.K.; Johnson, S.L.; Razavi, M. An automatic method for enhancing the display of different tissue densities in digital chest radiographs. J. Digit. Imaging **1993**, 6, 95–104. [CrossRef] [PubMed]
9. Seeram, E.; Seeram, D. Image Postprocessing in Digital Radiology—A Primer for Technologists. J. Med. Imaging Radiat. Sci. **2008**, 39, 23–41. [CrossRef] [PubMed]
10. Alshipli, M.; Kabir, N.A.; Hashim, R.; Marashdeh, M.W.; Tajuddin, A.A. Measurement of attenuation coefficients and CT numbers of epoxy resin and epoxy-based Rhizophora spp. particleboards in computed tomography energy range. Radiat. Phys. Chem. **2018**, 149, 41–48. [CrossRef]
11. Phywe XR 4.0 Expert Unit, X-ray Unit, 35 kV: Germany: PHYWE Systeme GmbH. Available online: https://repository.curriculab.net/files/bedanl.pdf/09057.99/0905799e.pdf (accessed on 18 July 2021).
12. XR 4.0 Software Measure CT Manual. PHYWE. Available online: https://repository.curriculab.net/files/bedanl.pdf/14421.61/1442161e.pdf (accessed on 18 July 2021).
13. CTvox Quick Start Guide. Bruker. Available online: https://www.bruker.com/fileadmin/user_upload/3-Service/Support/Preclinical_Imaging/X-Ray-uCT_Software/CTvox_QuickStartGuide.pdf (accessed on 18 July 2021).
14. Key Features of Dragonfly. Available online: https://www.theobjects.com/dragonfly/features.html (accessed on 18 July 2021).

15. NRecon User Manual. Available online: https://umanitoba.ca/faculties/health_sciences/medicine/units/cacs/sam/media/NReconUserManual.pdf (accessed on 18 July 2021).
16. MIPS (Medical/Microscopy Image Processing Software). Available online: http://webzam.fbmi.cvut.cz/hozman/ (accessed on 20 February 2022).
17. DICOM PS3.3 2021e—Information Object Definitions. C.11 LUT and Presentation States. Available online: https://dicom.nema.org/medical/dicom/current/output/chtml/part03/sect_C.11.2.htm (accessed on 28 November 2021).
18. Weiss, S.; Westermann, R. Differentiable Direct Volume Rendering. IEEE Trans. Vis. Comput. Graph. **2022**, 28, 562–572. [CrossRef] [PubMed]
19. Skyscan CT-Volume Manual. Available online: https://umanitoba.ca/faculties/health_sciences/medicine/units/cacs/sam/media/CTVol_UserManual.pdf (accessed on 18 July 2021).
20. Wolfram Research, Inc. Centroid of triangle–Wolfram Alpha. Wolfram Research, Inc., Champaign, IL. Available online: https://www.wolframalpha.com/input?i=centroid+of+triangle (accessed on 6 April 2022).
21. Stakat. Let's Master Statistics Together. Spearman's Rho. Available online: https://statkat.com/stat-tests/spearmans-rho.php#5 (accessed on 25 April 2022).
22. Real Statistics Using Excel. Spearman's Rank Correlation Hypothesis Testing. Available online: https://www.real-statistics.com/correlation/spearmans-rank-correlation/spearmans-rank-correlation-detailed/ (accessed on 25 April 2022).
23. Gaspar, B.; Mrzilkova, J.; Hozman, J.; Zach, P.; Lahutsina, A.; Morozova, A.; Guarnieri, G.; Riedlova, J. Data Availability Statement: There Are Available All LUTs as Images and *.tf Files and Relevant Images as Well. Available online: http://webzam.fbmi.cvut.cz/hozman/LUT.htm (accessed on 25 April 2022).